Measuring diffusion coefficients in low-porosity rocks by X-ray radiography

By

Guadalupe Maldonado Sánchez

A thesis submitted in partial fulfillment
of the requirements for the degree of

Master of Science

Department of Earth and Environmental Sciences

Faculty of Science

University of Ottawa

October 2020

"Two roads diverged in a yellow wood,
And sorry I could not travel both
And be one traveler, long I stood
And looked down one as far as I could
To where it bent in the undergrowth;

Then took the other, as just as fair,
And having perhaps the better claim,
Because it was grassy and wanted wear,
Though as for that the passing there
Had worn them really about the same,

And both that morning equally lay
In leaves no step had trodden black.
Oh, I kept the first for another day!
Yet knowing how way leads on to way
I doubted if I should ever come back.

I shall be telling this with a sigh
Somewhere ages and ages hence:
Two roads diverged in a wood, and I,
I took the one less traveled by,
And that has made all the difference"

Robert Frost, The road not taken.

To my family

Abstract

Deep geological repositories (DGR) are considered an effective long-term solution for radioactive waste disposal. Sedimentary (argillaceous formations) and crystalline rocks are currently under investigation worldwide as potential host formations for DGR. Their low porosity (< 1-2 %) and very low hydraulic conductivity result in diffusion-dominated solute transport. There is a need to investigate their diffusion properties in detail, the long-established diffusion methods do not allow an evaluation of the spatial relationship between tracers and the characteristics of the geological medium. The aim of this project was to measure diffusion coefficients in low-porosity rocks (< 2%) using X-ray radiography and iodide tracer. The method is a non-destructive technique based on the principle of X-ray attenuation; it provides temporal- and spatially-resolved information of a highly attenuating tracer diffusing in a sample. Samples from the Cobourg Formation, an Ordovician argillaceous limestone from the Michigan Basin, and from the Lac du Bonnet batholith, an Archean granitic pluton were used in this study. X-ray radiography data from the Cobourg Formation indicate tracer accumulation occurs on dark argillaceous layers in the rock characterized by clay minerals and organic matter. It is proposed that the I^- tracer solution underwent photo-chemical oxidation, leading to the formation of I_2, a highly reactive volatile iodine species and I_3^-, which readily reacted with humic substances contained in the clay- and organic rich zones in the limestone samples. In the case of the granitic samples, attempts at measuring diffusion coefficients encountered several challenges. The results indicate that tracer signal can be detected, however diffusion signal is masked by imaging errors and noise.

Acknowledgments

I would like to take the opportunity to express my gratitude to the amazing people who helped me accomplish my goal. It has been a privilege to have met, worked with and had a good laugh with all these great human beings, and to have being part of the Earth and Environmental Sciences Department at uOttawa.

First and foremost, a heartfelt thank-you to my supervisor Dr. Tom Al for his guidance, patience and endless support throughout this extraordinary journey. His wisdom and knowledge inspired me and motivated to become a better person and researcher, to see beyond the obvious and to ask the right questions. Method development is not for the faint of heart, but his encouragement made the challenge enjoyable and manageable when things got tough.

I would like to thank the Nuclear Waste Management Organization and the National Sciences and Engineering Research Council of Canada for funding this research. This project has also been possible thanks to the assistance of Glenn Poirier, David Diekrup, Renelle Dubosq, Alain Mauviel, Hervé Beaudoin and Jean-Guy Brunet from uOttawa, and Stephen Delahunty and Calvin Nash from the University of New Brunswick.

Thank you to my thesis examiners Dr. Danielle Fortin and Dr. Richard Amos for their valuable comments on this manuscript. Special gratitude goes to Carla Rose (if you had not helped me to organize my ideas and had not pushed me to write, my thesis would have not been finished yet!), Birendra Sapkota (your expertise and help with the EMSA files and DTSA were crucial to the completion of this thesis), and Magda Celejewski (your assistance in improving my writing skills was invaluable).

To my colleagues Jacob Nunn, Ryan Miller, Samuel Morfin, Jiujang Zhao and Shuo Liang thanks for insightful discussions and suggestions to the project. To Simon Hayles and Geneviève

Ménard thank you so much for your friendship and brightening up my life in Ottawa, you made me feel at home away from home. To Goli, Evelyn, Dania, Dom and all members of Tom's research group, thank you for cheering me up and making my time in the Department memorable.

To Wendy Abdi, Kerry Klassen, Patricia Wickham and Paul Middlestead many thanks to you for welcoming me warmly into the Ján Veizer Stable Isotope Lab, for your kind words of support, thoughtful suggestions and fantastic sense of humor. It has been a delight to work with you all.

Finally, my heart goes to my parents, Aurelio and Teresa, to my sisters Celia, Marisol and Maria del Socorro, and to my cheerleaders Ithiel, Mary Luz, Alain, Cris, Sofía, Fernanda, Efra and Juan. Thank you for walking beside me this long path and for being my lighthouse during troubled times. I have achieved this milestone because of all of you.

Contents

Abstract III

Acknowledgments IV

List of Figures IX

List of Tables XIII

Chapter 1

Introduction 1

1.1. Nuclear waste and the DGR Concept 1

1.1.1. The Bruce Nuclear Site 3

1.2. Diffusion in porous media 6

1.2.1. Fick's laws 6

1.2.2. Porosity and diffusion properties 7

1.3. X-ray radiography with geological materials 9

1.3.1. Theory 10

1.3.2. The X-ray radiography method 13

1.3.3. Challenges with low-porosity rocks 15

1.4. Objectives 16

1.5. Thesis organization 17

1.6. References 17

Chapter 2

Iodide behaviour in argillaceous limestone: insights from X-ray radiography 21

2.1. Introduction 21

2.1.1. The conundrum of iodide transport in clay-rich rocks 21

2.1.2. X-ray radiography to investigate diffusion in heterogeneous media 23

2.2. Materials and methods 25

2.2.1. Sample origin and description 25

2.2.2. Water-accessible porosity 27

2.2.3. Synthetic porewater and I^- tracer 27

2.2.4. X-ray radiography 28

2.2.5. SEM imaging 30
2.3. Results and discussion 31
2.3.1. Water-accessible porosity 31
2.3.2. X-ray and SEM analysis 31
2.3.3. Iodine species adsorption and chemical transformations 38
2.3.4. Humic substances in argillaceous rocks 40
2.3.5. HS and iodine species retention 41
2.4. Conclusions and future work 42
2.5. References 43

Chapter 3

Summary and Conclusions 51
3.1. Concluding remarks 51
3.1.1. Cobourg Formation argillaceous limestone experiments 51
3.1.2. Lac du Bonnet granite experiments 52
3.1.3. Limitations of the method 53
3.2. Future work 54
3.3. References 54

Appendix A

Diffusion experiments in granitic rocks 55
A.1. Introduction 55
A.2. Materials and methods 55
A.2.1. Lac du Bonnet Batholith samples 55
A.2.2. Experimental procedures 57
A.3. Results and Discussion 59
A.3.1. X-ray radiography diffusion profiles 60
A.4. Conclusions 65
A.5. References 65

Appendix B

X-ray Radiography, standards and registration 67
B.1. Introduction 67
B.2. Background 67

B.3. Methodology 68
B.4. Results and Discussion 71
B.5. Summary and Conclusions 77
B.6. References 78

Appendix C

Petrographic analysis of the Cobourg Formation 79
C.1. Introduction 79
C.2. Background 80
C.3. Qualitative petrographic analyses 80
C.3.1. DGR3-675.46 80
C.3.2. DGR4-671.24 81
C.4. Summary and Conclusions 83
C.5. References 83

Appendix D

Greyscale (gsv) and ▪▪ profiles of the Cobourg Formation 85
D.1. Introduction 85
D.2. Gsv and ▪▪ profiles 85

List of Figures

Figure 1.1. DGR concept for the Bruce nuclear site, Kincardine, ON, Canada. 3

Figure 1.2. Location of the Bruce nuclear site. DGR-1 to DGR-6 indicate drilled boreholes sites. 4

Figure 1.3. a) Geology of southern Ontario showing the location of the Bruce nuclear site (BNS); **b)** Cross-section showing the stratigraphy of the northeastern margin of the Michigan Basin, **c)** Stratigraphic column and hydrostratigraphy of the BNS. 5

Figure 1.4. **a)** Schematic illustration of the solute-specific accessibility in a saturated porous medium. **b)** Representation of tortuosity (τ); L_d: length of a solute's diffusive pathway compared to the straight-line, L_s: length across the medium. 9

Figure 1.5. X-ray attenuation through an object of thickness d ($d = d_1 + d_2 + \ldots d_n$) in **a)** a homogeneous material, and **b)** a heterogeneous medium with different attenuation coefficients (μ) along the X-ray path 11

Figure 1.6. Set up of the X-ray radiography method 14

Figure 1.7. One-dimensional $\Delta\mu$ profiles representing the diffusion of an X-ray attenuating tracer (iodide) over time during an experiment. 14

Figure 1.8. Relative I^- concentration profiles (C/C_0) and D_p obtained for **a)** Queenstone shale and **b)** Cobourg limestone. Sample porosities are indicated in brackets; PB: parallel to bedding; NB: normal to bedding. 16

Figure 2.1. Subsampling of the DGR core segments normal to bedding for X-ray radiography. 26

Figure 2.2. Diagram of a sample mounted in the diffusion cell used for X-ray radiography. 28

Figure 2.3. **A and B**: profiles of mean greyscale values prior to addition of tracer (black solid line, right axis), and $\Delta\mu$ (coloured lines, left axis) versus distance after the addition of tracer, for samples DGR3-675.46-c and DGR4-671.24-a. The numbers next to the $\Delta\mu$ profiles indicate the number of days after the diffusion experiment started. **C and D:** polished thin sections from samples DGR3-675.46-c and DGR4-671.24-a, cut along the core axis, perpendicular to the X-ray path, after diffusion experiments ended. SEM-BSE images and EDS analyses were conducted on regions of interest (ROI) marked 1 to 6 (yellow squares). 34

Figure 2.4. ROI 1 and ROI 2 from the lower section of DGR3-675.46-c. Large arrows show the direction of diffusion, white rectangular areas in the images at left are magnified in the images at right and at the bottom. **a)** Concentrically-zoned dolomite and calcite grains in fine-grained matrix. **b)** Detail of the supporting matrix. X-ray spectrum (spot 1) confirms clay mineralogy and organic matter. **c)** Pyrite crystals and framboids within organic matter and calcium carbonate minerals. 35

Figure 2.5. BSE image of DGR3-675.46-c, ROI 3. The magnified area on the right (**d**) shows carbonate minerals and laminated organic matter preserved in a clay-rich matrix confirmed by X-ray spectra (spots 1 and 2). 36

Figure 2.6. BSE images from ROI 4, ROI 5 and ROI 6. White arrows show the direction of diffusion, rectangular areas in the images at left, are magnified in the images at right. e) Pyrite, zoned dolomite and organic matter with the presence of clay minerals suggested by detectable Al, Si and K in the X-ray spectrum from spot 1. f) Finely laminated clay minerals (corroborated by X-ray spectrum from spot 2) mixed with organic matter. g) Organic matter with clay (yellow arrows) in a clay-rich matrix with zoned dolomite and anhedral quartz. 37

Figure A.1. Geology of the Lac du Bonnet batholith, and the location of the Whiteshell nuclear facility (WRF) and the Underground Research Laboratory (URL; modified from Brown et al., 1998). 56

Figure A.2. Photograph of the Lac du Bonnet drill core showing sections were subsamples were obtained..... 57

Figure A.3. Diagram of a granite sample mounted in the diffusion Delrin® cell used for X-ray radiography. 58

Figure A.4. Microphotographs of core 275-EXT-NI. A: centre occupied by quartz (Q) with undulose extinction and fluid inclusions close to the edge, biotite (Bi) with pleochroic halos and microcline (M) with cross-hatched twinning. Mirmekite rods. B: Microfractures in microcline and common intragranular microquartz. 59

Figure A.5. $\Delta\mu$ versus distance graphs of granite # 2 and #4 obtained using different standards to adjust for variations of X-ray intensities from image to image. A and B: aluminium on top of the sample; C: a ceramic block inserted in the shielding screen, and D: a region on the sample. 62

Figure A.6. A: effects of misalignment and inaccurate adjustments of X-rays intensities (Al cap standard) on the granite # 2 greyscale vs distance plot. B: granite #4 profile showing effects of image quality on registration. Greyscale values (gsv) on the plot inflections (red arrows) display uneven signal and noise, more significant close to the top of the sample (from 15-23 mm)..... 63

Figure A.7. Representation of the blank subtraction method on a region of interest (red rectangle) for an imaged sample. A: reference image and baseline greyscale values. B: greyscale values reflecting the presence of tracer (blue area) in the sample after the blank subtraction removes efficiently the rock matrix C: anomalous greyscale values due to physical and image misalignment..... 64

Figure B.1. Examples of $\Delta\mu$ profiles of DGR3-675.46-a and DGR3-675.46-c samples showing alignment artifacts. 68

Figure B.2. Shielding screen used in the experiments to protect the detector from oversaturation. Front view (left) shows the ceramic (grey pattern) and aluminum (grey solid) blocks inserted in the frame made of ceramic (Mykroy/Mycalex) bricks (yellow). Lateral view (right) shows the slanted angle of the blocks. 69

Figure B.3. X-ray radiography image of the aluminum bar showing the position of the lead ball (black circle) used for registration. Three different areas on the screen (yellow rectangles) and one on the aluminum bar (blue rectangle) were used for normalization of the greyscale values measured from the aluminum bar (large blue rectangle). 70

Figure B.4. X-ray radiography image of the limestone sample obtained with the modified screen. Left: location of the region of interests (ROI) on each of the materials tested. Black circles: lead balls inserted inside of the ceramic and aluminium blocks..... 70

Figure B.5. Greyscale values (gsv) versus distance plots of the aluminum bar imaged at on-, mid- and off-peak periods of electricity consumption. The normalization of the time-series X-ray intensities was done using a vertical (V) and horizontal (H) area on the shielding screen (**A** and **B** respectively), and a lead ball (**C**). **D**: Mean gsv (normalized measurements) of the aluminum bar over time showing one standard deviation (coloured bands). Sun: Sunday; Mon: Monday; Tue: Tuesday. 1: morning; 2: noon; 3: evening. 72

Figure B.6. A: mean gsv versus distance plots of the aluminum bar. The X-ray intensities were normalized using a region on the imaged bar. **B**: Mean gsv profile of an image acquired while the instrument voltage swung during image acquisition (in red).**C**: Normalized mean gsv using the aluminum bar. Shaded area indicates the standard deviation (1 σ)..... 73

Figure B.7. Variation of gsv with changes in X-ray tube voltage (keV) of the tested materials (limestone core, aluminum and ceramic blocks) considered as potential standards for diffusion experiments with X-ray radiography (dashed lines are the best-fitting line). 74

Figure B.8. Percentage variation of the mean gsv with different voltages of the standard materials tested. X-ray images triplicates were obtained at 4-hours intervals. 75

Figure B.9. Percentage difference between the limestone and the Al and Cer blocks as potential standard materials. **A**: mean gsv. **B:** plot showing two-fold increase in the percentage difference when the ln of the mean gsv is calculated. 76

Figure C.1. Thin sections obtained from the centre of the 76-mm DGR3-675.46 and DGR4-671.24 cores. Argillaceous fine laminations are observed on the two of them. 79

Figure C.2. A) Soft sediment mud clast. **B)** Pellets in carbonate mud and iron-stained clay-rich matrix. **C**) Large brachiopod fragment, crinoids and skeletal clasts in a micritic matrix. **D)** Recrystallized dolomite crystals in a micritic groundmass. 81

Figure C.3. A) Compacted grains along argillaceous seams. The allochems have crushed edges. **B)** Star-shaped crinoid showing crushing with another shell fragment. **C**) Broken edges and crushed grains in direct contact in clay-rich areas. **D)** fine-grained, euhedral recrystallized dolomite within a clay-rich matrix. Red arrows showing a stylolite. 82

Figure D.1. Mean gsv vesus distance profiles for DGR3-675.46-a (**A**) and -c (**B**), and DGR4-671.24-a (**C**) and -c (**D**) subcores showing X-ray attenuation variability along the sample length. The black line (0 hrs) displays the gsv prior to tracer diffusion and the red line indicates the X-ray attenuation caused by tracer diffusing in the pore space over time (*n* days). 86

Figure D.2. $\Delta\mu$ versus distance plots for samples DGR3-675.46-a **(A)** and DGR4-671.24-c (**B**). The numbers next to the profiles indicate the number of days after the diffusion experiment started. **C:** DGR3-675.46-c polished thin section cut along the core axis after the diffusion experiment ended. 87

List of Tables

Table 1.1. General characteristics of nuclear waste and disposal recommendations. Waste classes defined by the International Atomic Energy Agency (IAEA, 2009). 2

Table 2.1. Average mineralogical composition (wt. %) of the Cobourg Formation (DGR3 core) identified by XRD analysis. 26

Table 2.2. Synthetic porewater (SPW) and I^- tracer solution used for the diffusion experiments 27

Table A.1. Synthetic porewater (SPW) and iodide tracer solution used for the diffusion experiments. 57

Table B.1. Physical characteristics of the tested materials to be used as standards. 74

Chapter 1

INTRODUCTION

1.1. Nuclear waste and the DGR Concept

Nuclear power plants around the world have generated electricity for nearly 60 years and currently provide 10% of the world's consumption (IAEA, 2019). The unavoidable byproduct of this activity is radioactive waste which needs to be managed and safely disposed to protect humans and the environment from its damaging effects. However, the production of radioactive waste is not limited to nuclear power plants, waste is also generated in a broad range of facilities that use radionuclides such as medical, research and defense centres (McGinnes, 2007). The estimated global inventory of nuclear waste that required some type of storage in early 2000's was 8.13×10^6 m^3 (IAEA, 2008) of low-(LLW), intermediate-(ILW) and high-level waste (HLW; Table 1.1). In Canada, it is expected that about 5.2 million used CANDU (Canada Deuterium-Uranium) fuel bundles will be generated when the 20 nuclear power reactors hosted in three plants in Ontario and one in New Brunswick end operations (Garamszenghy, 2015). This estimate (which includes bundles from two reactors in one plant in Québec that has reached the end of its life and has started the decommissioning process) would require a storage facility the size of fifteen hockey rinks.

The international consensus is that deep geological repositories (DGR) can provide an effective solution to the long-term management of nuclear waste, supplying the prolonged containment (thousand to million years) required to isolate the residue and to allow radioisotope decay to innocuous radioactive levels. A DGR (Fig. 1.1) is an engineered facility excavated deep underground, planned to safely isolate nuclear waste encased in containers placed in a network of rooms within a geologic formation with a series of surrounding barriers (clay-based and concrete sealing systems; Guo, 2017). An important aspect in the DGR concept is the stability of the

geological medium which is the ultimate natural barrier. The geosphere should provide mechanical protection (physical stability) over long timescales, optimal geochemical conditions (e.g. 4 < pH <10, reducing conditions and low to medium salinity) and negligible groundwater movement to prevent contact with the biosphere (Bredehoeft et al., 1985; McKinley et al., 2007).

Over the past forty years, many countries (e.g. France, Switzerland, Belgium) have been developing national programs on the safety and feasibility of repositories hosted mainly in sedimentary and crystalline rocks (e.g. clay-rich formations and granitic rocks; Altman et al., 2004; Gimmi et al., 2014; Vilks et al., 2003). It has been found that the low porosity and very low hydraulic conductivity (on the order of 10^{-10} to 10^{-16} m/s; Beauheim et al., 2014; Wilson et al., 1983) of these rocks could make them an effective barrier to radionuclide migration.

Table 1.1. General characteristics of nuclear waste and disposal recommendations (modified from McGinnes, 2007). Waste classes defined by the International Atomic Energy Agency (IAEA, 2009).

Waste Class	Characteristics	Disposal options
Low-level and intermediate-level waste (short-lived)	Restricted long-lived radionuclide concentrations (<400 Bq/g or 4000 Bq/g maximum per package).	Near surface or geological repository
Low-level waste (LLW, long-lived)	Waste exceeding 0.4 Bq/g $\beta\gamma$ per item but <4000 Bq/g α[1] and <12,000 Bq/g $\beta^2\gamma^3$.	Geological disposal facility
Intermediate-level waste (ILW, long-lived)	Waste exceeding LLW levels and having low heat-generating capacity (< 2 kW/m^3).	Geological disposal facility
High-level waste (HLW)	Heat-generating (thermal power greater than 2 kW/m^3).	Geological disposal facility

[1]α radiation barely penetrates the skin, it can be stopped by a piece of paper; [2]β radiation requires little shielding; [3]γ radiation can pass through the human body, it is absorbed by concrete or lead.

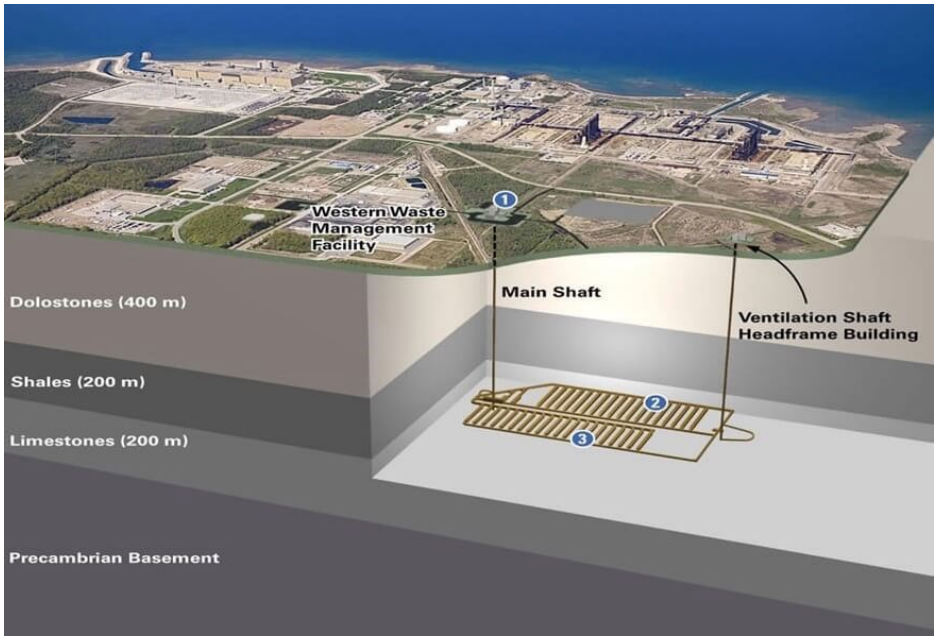

Figure 1.1. DGR concept for the Bruce nuclear site, Kincardine, ON, Canada (Patel, 2017).

In 2015, Finland became the first country to approve the construction of a DGR at a depth of 400 m in Paleoproterozoic crystalline rocks, and it is expected to become operational in 2020 (Engström et al., 2016). In Canada, the Atomic Energy of Canada Limited (AECL) started to develop a geoscience research program with the construction of the Underground Research Laboratory (URL) in the Lac du Bonnet Batholith in Manitoba (Brown et al., 1989). However, after AECL submitted its environmental impact assessment in 1994, the review panel recommended that even though it was technically safe, the public did not support the proposal of a DGR facility (Witherspoon and Bodvarsson, 2006).

1.1.1. The Bruce Nuclear Site

The Nuclear Waste Management Organization (NWMO) was established in 2002 and is responsible for finding a site to host a DGR for Canadian radioactive waste. The NWMO also managed site characterization activities for a proposed DGR for the long-term storage of LLW and

ILW on the Bruce Nuclear site (BNS)* located 225 km northwest of Toronto, Ontario (Fig. 1.2). Six deep boreholes (DGR-1 to DGR-6; Fig. 1.2) were drilled to characterize the geology under the BNS. The site is located on the east margin of the Michigan Basin, and the geology consists of an 840 m thick Paleozoic sedimentary sequence (Cambrian to Devonian) of near horizontally bedded (average regional strike of N14°W and dip of 0.6° SW) and weakly deformed shales, carbonates and evaporites (Fig. 1.3; Raven et al., 2010). The proposed DGR would have been excavated at a depth of 680 m within the Cobourg Formation, an Ordovician argillaceous limestone overlain by 200 m of shale. The 35 m thick Cobourg Formation was of interest due in part to its low hydraulic conductivity (4 x 10^{-15} to 3 x 10^{-14} m/s; Beauheim et al., 2014) and porosity (1-2 %). In the event of a loss of containment in clay-rich formations, diffusion would be the only mechanism for solute transport (Altmann et al., 2012; McKinley et al., 2007).

Figure 1.2. Location of the Bruce nuclear site. DGR-1 to DGR-6 indicate drilled boreholes sites.

*In January 2020, the Saugeen Ojibway First Nation voted against the project and the site is no longer being considered to host a DGR.

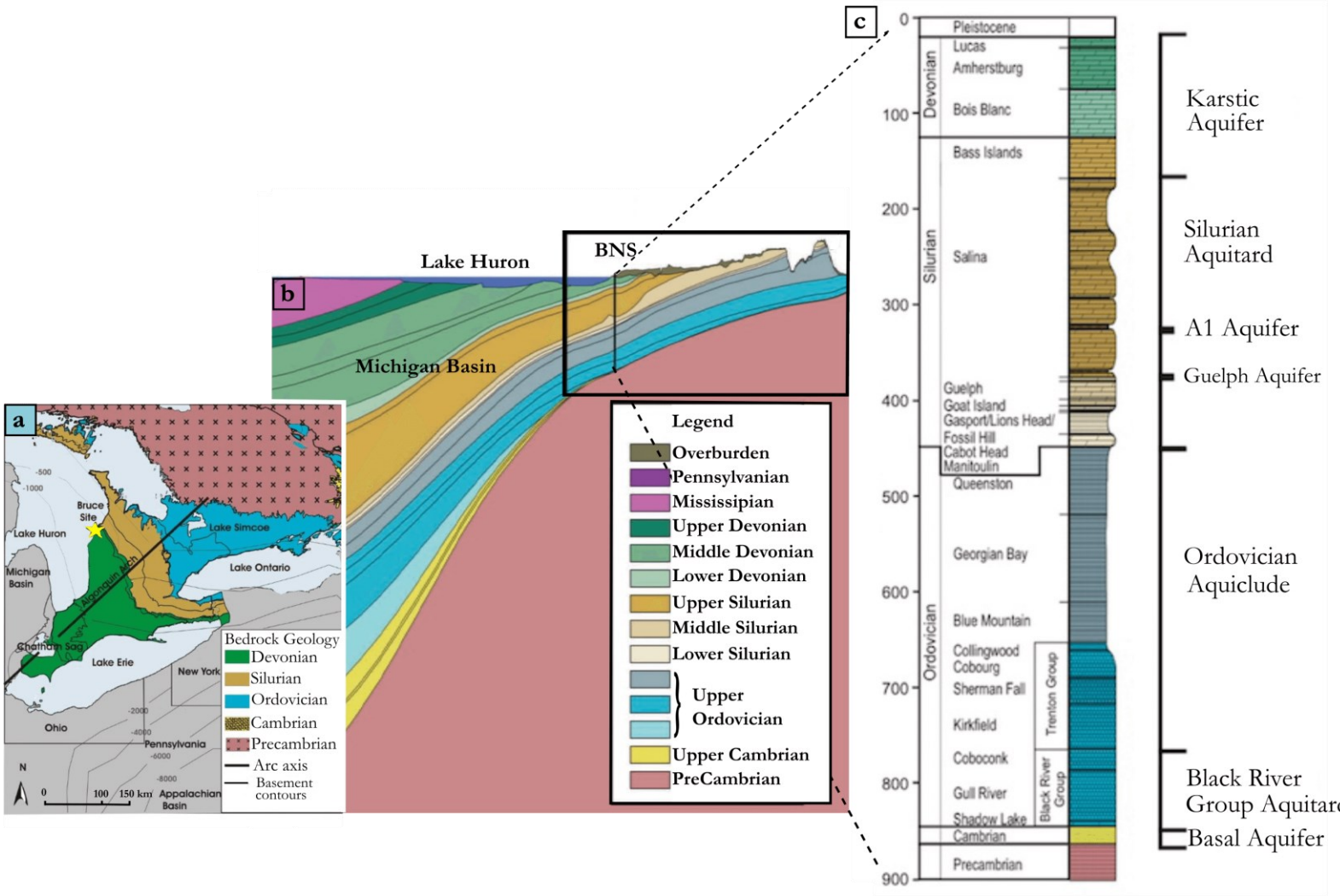

Figure 1.3. a) Geology of southern Ontario showing the location of the Bruce nuclear site (BNS; modified from Al et al., 2015); **b)** Cross-section showing the stratigraphy of the northeastern margin of the Michigan Basin (modified from Clark et al., 2013) **c)** Stratigraphic column and hydrostratigraphy of the BNS (from Al. et al., 2015).

1.2. Diffusion in porous media

1.2.1. Fick's laws

In very low permeability rocks, such as clay-rich sedimentary sequences and unfractured granite, it is expected that diffusion will be the main transport mechanism for contaminants (Polak et al., 2003; Shackelford, 1991). Diffusion is a fundamental physico-chemical phenomenon in all natural systems. In basic terms, it is defined as the thermal motion of molecules and ions from areas of high concentration to areas of low concentration that results in mass movement (Singhal and Gupta, 2010). Alfred Fick, a physiologist, described mathematically the laws of diffusion which he related to Fourier's law for heat conduction (Crank, 1975; Philibert, 2005). His first law posited that the mass flux (*J*) is directly proportional to the concentration gradient with a proportionality factor, thus it predicts how much flux can be expected. It is expressed as:

$$J = -D \frac{\partial C}{\partial x} \qquad [1.1]$$

where *D* is the diffusion coefficient (length^2/time), a constant that depends among other things on temperature, the size, mass and charge of the solute and the composition of the fluid; *C* is the solute concentration (mass/L^3), and ∂C/∂x is the solute concentration gradient (Grathwohl, 1998). The negative sign in the equation is used to follow mathematical sign convention that indicates the solute movement (*J*) takes place down a concentration gradient (Shackelford and Moore, 2013).

Fick's first law describes transport of species in a fluid at a constant temperature where *J* and ∂C/∂x do not depend on time, hence it is at steady state (Watson and Baxter, 2007). However, geochemical systems rarely attain steady-state conditions and Fick's second law accounts for variation in concentration with time; the equation for the non-steady state diffusion in one spatial dimension (*x*) is written as follows (Shackelford and Moore, 2013):

$$\frac{\partial C}{\partial t} = D \frac{\partial^2 C}{\partial x^2} \qquad [1.2]$$

where $\partial C/\partial t$ is the change in concentration over time.

The molecular diffusion coefficient for a solute in water, also known as the free-water diffusion coefficient (D_0), is large relative to that in porous media because there is no resistance to the random molecular motion of a solute (Singhal and Gupta, 2010). Diffusion coefficients in any natural porous system, such as sediments and rocks, are smaller because diffusion follows a more complicated path than in free water.

1.2.2. Porosity and diffusion properties

In geological porous media, pore space is an inherent, complex rock component occupied by fluids such as water, gas, oil, or a mixture of them; some pores may contain solids (secondary minerals) or even host living organisms (Anovitz and Cole, 2015; Milliken and Curtis, 2016). Pore sizes can vary across a wide range and can be modified by various processes (microbial growth, diagenesis, weathering, hydrothermal alteration, etc.) as the rock responds to chemical and physical changes (Anovitz and Cole, 2015; Yoon et al., 2015). The pore structure, and the extent of its connectivity, control fluid flow and transport. It has been widely recognized that in transport experiments, the measured porosity is frequently less than the total (physical) porosity (Pearson, 1999). For this reason, two distinctive porosity terms are commonly used in diffusion studies: water-accessible porosity (φ_w) and tracer-accessible porosity (φ_{tr}; Al et al. 2015). These parameters indicate the portion of the total volume of the rock that is accessible to porewater and specific solutes (e.g. Cl^-, I^-, etc.; Fig. 1.4a) for diffusion (García-Gutiérrez et al., 2004).

When diffusion occurs in the pore space, solutes are constrained within the pore system, thus their path is tortuous and follows a complex trajectory (Ghanbarian et al., 2013). In order to account for the characteristics of the porous medium, three types of diffusion coefficients have been defined

in the literature: the free-water diffusion coefficient (D_0), the pore diffusion coefficient (D_p), and the effective diffusion coefficient (D_e; Al et al. 2015).

The free-water diffusion coefficient (D_0) applies to diffusion of chemical species in aqueous fluids. D_p takes into account the tortuosity (τ) and constrictivity (δ) of the pore system and is related to D_0 as follows (García-Gutiérrez et al. 2004):

$$D_p = \frac{\delta}{\tau} D_0 \quad [1.3]$$

Different definitions of τ have been provided and are sometimes used interchangeably in the literature, leading to confusion. Since the discussion of the term is beyond the scope of this work, I will use the concept of diffusive tortuosity defined by Epstein (1989) and Ghanbarian et al. (2013) that accounts for the porosity of the medium and the molecular size of the solute. It is expressed as the square of the ratio of the average length of a solute's diffusive pathway (l_d) to the straight-line length (l_s) across the medium (Fig. 1.4b).

$$\tau = \left[\frac{l_d}{l_s}\right]^2 \quad [1.4]$$

Constrictivity ($\delta \leq 1$) is a dimensionless parameter that accounts for the variations in pore radii along the transport direction (van Brakel and Heertjes, 1974).

The effective diffusion coefficient (D_e) incorporates φ_{tr}, which is obtained experimentally and is different for each tracer (Al et al., 2015):

$$D_e = \varphi_{tr} D_p \quad [1.5]$$

The diffusion behaviour of a solute that interacts with the porous media (e.g. adsorption, ion exchange) can be described with the apparent diffusion coefficient (D_a). Since D_a takes into account the matrix porosity and the sorption response of the solute, the equation is defined as D_e divided by the rock capacity factor (α; Grathwohl, 1998).

$$D_a = \frac{D_e}{\alpha} \quad [1.6]$$

The rock capacity factor (α) includes the dry bulk density of the material (ρ_d) and the distribution coefficient (K_d). It is a dimensionless parameter written as follows (García-Gutiérrez et al., 2004; Shackelford and Moore, 2013):

$$\alpha = \varphi_{tr} + \rho_d K_d \quad [1.7]$$

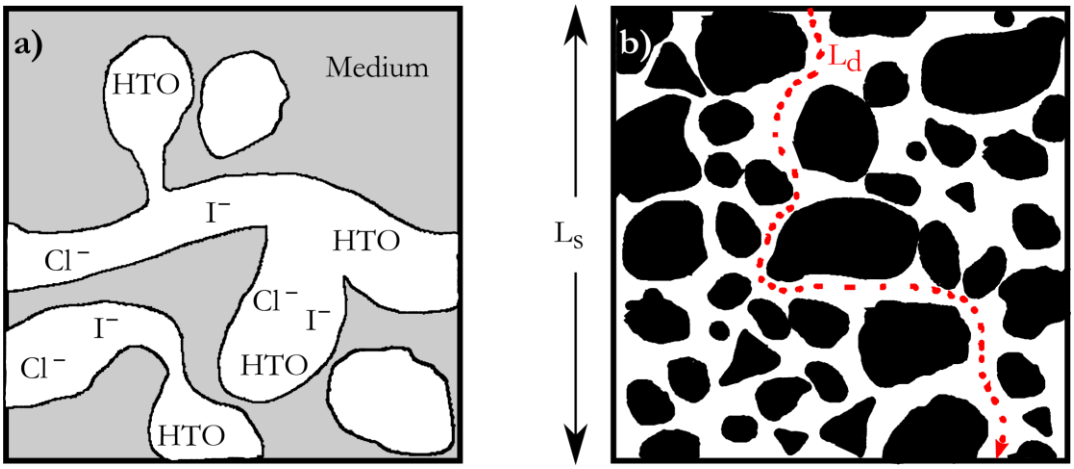

Figure 1.4. **a)** Schematic illustration of the solute-specific accessibility in a saturated porous medium (modified from Shackelford and Moore, 2013). **b)** Representation of tortuosity (τ); L_d: length of a solute's diffusive pathway compared to the straight-line, L_s: length across the medium (modified from Ghanbarian et al., 2013).

1.3. X-ray radiography with geological materials

Measurement of diffusion coefficients in sediments and rocks have traditionally been conducted using well-established laboratory methods such as through-diffusion, in-diffusion and out-diffusion. These techniques measure the solute flux through (into or out of) a sample that is placed between two reservoirs; one containing a tracer of interest (e.g. tritiated water -HTO-, I^-, Cl^-) and the other serving as a collection reservoir from which the tracer solution is continuously removed to maintain the concentration gradient (Shackelford, 1991). Some of the disadvantages of these conventional methods are that in most cases they should achieve and maintain steady-state

conditions, and in the case of using a non-conservative tracer and/or large samples, the time required to measure D_e can be extremely long (Shackelford, 1991; Grathwohl, 1989). Additionally, the obtained D_e values represent bulk measurements, which limits our understanding of spatial heterogeneities in properties such as porosity and connectivity that influence mass transport. Therefore, it is important to assess the temporal and spatial variation of solute transport in relation to the physical and chemical characteristics of the porous medium.

X-ray radiography imaging has been used for investigating diffusion in dolomite (Tidwell et al., 2000), in diverse fracture-filling material in crystalline rocks (Altman et al., 2004) and in low-permeability shale (Cavé et al., 2009). The method is based on the principle of X-ray attenuation by a diffusing tracer, and it usually involves collection of time-sequence radiographs for a sample, with the attenuation increasing over time as the X-ray tracer concentration increases. The changes are visualized and quantified (Altman et al., 2004; Cavé et al., 2009; Tidwell et al., 2000).

1.3.1. Theory

When an X-ray beam passes through matter, interactions between photons and electrons in the object are of greatest interest. The X-rays are attenuated by photoelectric absorption and compton scattering processes (Ketcham and Carlson, 2001). For a monochromatic X-ray beam, the Beer-Lambert Law [Eq. 1.8] predicts the exponential reduction in intensity with distance through a homogeneous material (Fig. 1.5a; Tidwell and Glass, 1994):

$$I = I_0{}^{-\mu d} \qquad [1.8]$$

where I_0 is the incident X-ray intensity on the object of thickness d; I is the intensity of the transmitted X-ray beam, and μ is the X-ray linear attenuation coefficient. When polychromatic X-ray radiation interacts with a heterogeneous medium, such as geological samples, equation [1.8] becomes:

$$I = \int_0^{E_{max}} I_0(E) \exp\left[-\int_0^i \mu'(E) d_i\right] dE \qquad [1.9]$$

where I_0 varies with the range of the X-ray energies (E_{max}), μ' is the linear attenuation coefficient that also depends on E, and i is the number of discrete materials in the heterogeneous solid (Jussiani and Appoloni, 2015). Equation [1.9] takes into account variations in the source energy spectrum and the attenuation coefficients for different solids along the linear extent of the X-ray path (Fig. 1.5b).

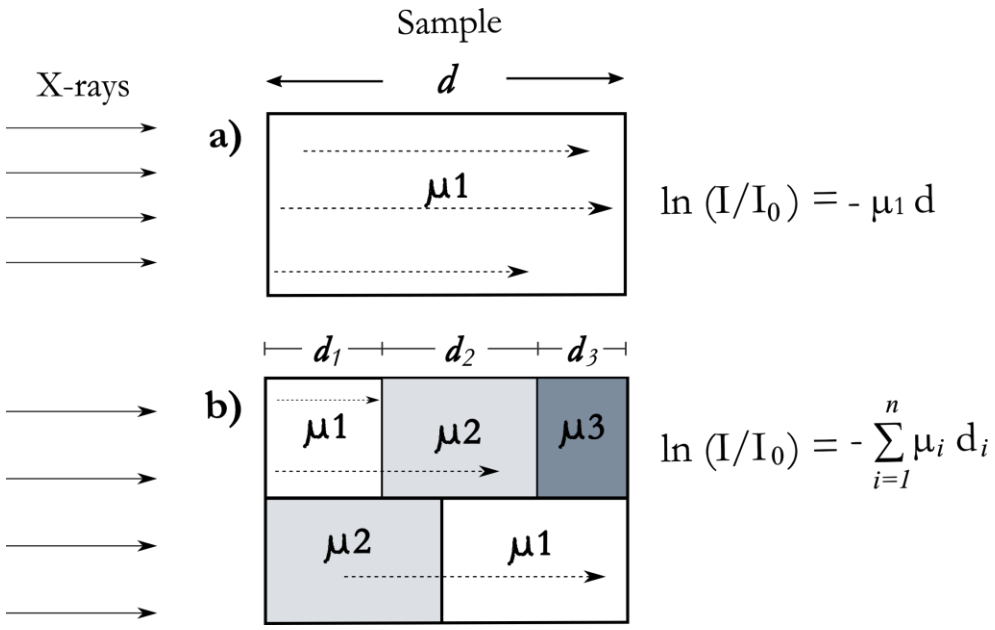

Figure 1.5. X-ray attenuation through an object of thickness d ($d = d_1 + d_2 + \ldots d_n$) in **a)** a homogeneous material, and **b)** a heterogeneous medium with different attenuation coefficients (μ) along the X-ray path (modified from Van Geet et al., 2000).

μ represents the probability of a potential fraction of the beam being absorbed or scattered as it passes through the sample (Sprawls, 2019). The degree of attenuation is determined by the atomic density (N) and the atomic cross section (σ; Eq. 1.10; Hussein, 2007; Jussiani and Appoloni, 2015).

$$\mu = N\sigma \qquad [1.10]$$

N accounts for the number of atoms per unit volume in the medium [Eq. 1.11], and σ takes into consideration the X-ray photon energy, target composition and the type of interactions, i.e., photoelectric, compton or pair production (Eq. 1.12; Hussein, 2007):

$$N = N_a \frac{\rho}{A} \quad [1.11]$$

where N_a is the Avogadro's number, ρ is the density of the material and A is the molecular weight.

In equation [1.12] σ_{pe} is the probability of photoelectric interaction and σ_c represents the probability of compton interaction (Jussiani and Appoloni, 2015). The effective atomic number (Z_{eff}) is a parameter that represents the X-ray attenuation in a medium composed of different elements in varying proportions (Manohara et al., 2008), such as geological materials. The collective interaction of chemical elements making up the material is weighed proportionally to their content (Murty, 1965).

$$\sigma = \sigma_{pe} + Z_{eff}\sigma_c \quad [1.12]$$

Photoelectric absorption and compton scattering are the only relevant processes in X-ray radiography for geological materials. Photoelectric interaction occurs when a photon from the X-ray beam collides with an inner shell electron, transmitting all of its energy and ejecting the electron (Selman, 2000). For this process to occur, the incident photon must have slightly higher energy than the *s, p* energies of the inner-shell electrons (Hussein, 2007). For most geologic materials, this means that photoelectric interactions occur at energies below 100 keV. The compton effect takes place when a photon from the X-ray beam collides with a loosely bound outer electron from an atom. The photon undergoes an inelastic collision with the electron, causing it to be ejected from the atom; the photon loses some of its initial energy and changes direction (Selman, 2000). This scattered radiation impairs image contrast and degrades image quality (Aichinger et al., 2012).

1.3.2. The X-ray radiography method

The X-ray technique developed by Cavé et al. (2009), based on the work of Tidwell et al. (2000) and Altman et al. (2004) to measure diffusion coefficients, uses an X-ray source, a stage and a detector. The sample of interest is saturated with synthetic pore water (SPW) and placed in a cell with a lower reservoir filled with SPW (Fig. 1.6). The experiment begins when an X-ray-attenuating tracer is added to the lower reservoir. Radiographic images are collected from the moment the tracer solution is introduced in the lower reservoir (reference image) and at selected time intervals (time-series images) afterward, until the tracer is homogeneously distributed in the sample. Using ImageJ (Rueden et al., 2017), a Java image processing program, identical regions of interest (ROI) are selected from the reference and time-series radiographs, and the pixel grey scale values (gsv) are averaged in the direction transverse to the diffusion direction and then ln-transformed to create μ profiles versus diffusion distance ($\mu = \ln(gsv)$). Changes in X-ray attenuation ($\Delta\mu$) caused by tracer mass diffusion over time are obtained by subtracting the reference μ profile from the time-series μ profile. This procedure, known as difference imaging, is analogous to blank subtraction in analytical chemistry (Tidwell et al. 2000; Altman et al., 2004; Cavé et al., 2009) and it removes the constant sample background from the radiographs. An example of a $\Delta\mu$ profile obtained by this approach is provided in Fig. 1.7 which illustrates the diffusion of I^- after 25, 72 and 264 hours; $\Delta\mu$ is proportional to I^- concentration.

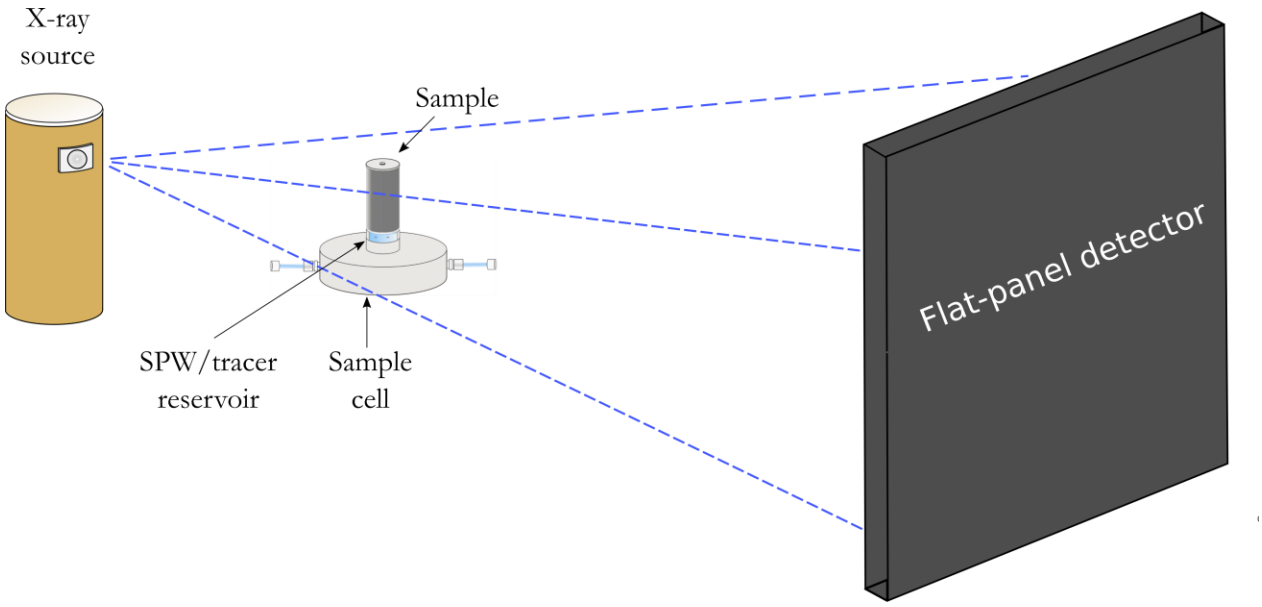

Figure 1.6. Set up of the X-ray radiography method.

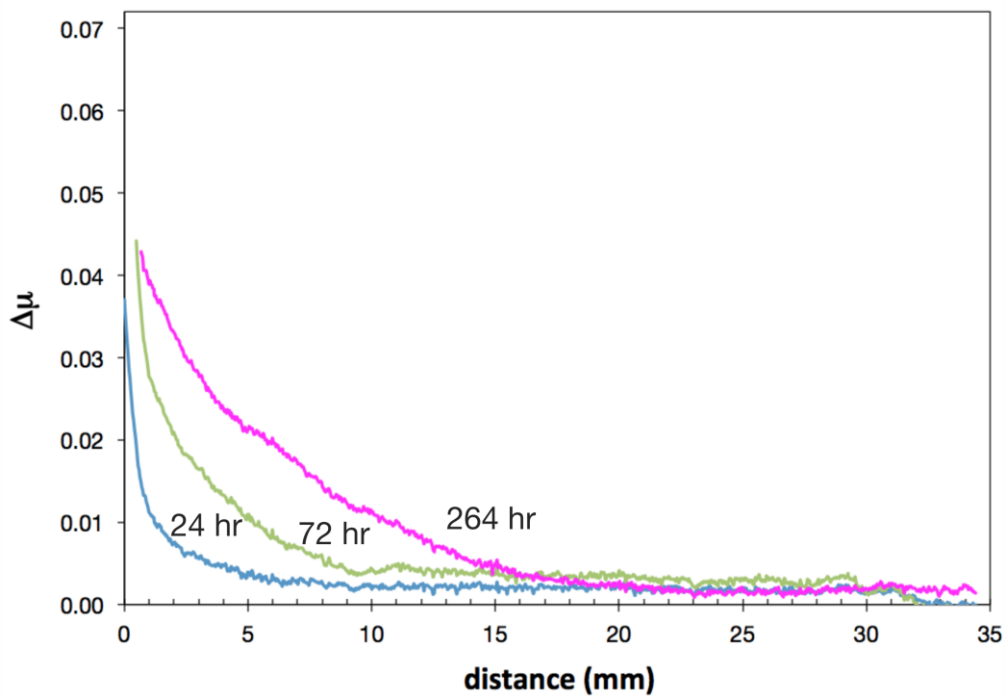

Figure 1.7. One-dimensional Δμ profiles representing the diffusion of an X-ray attenuating tracer (iodide) over time during an experiment.

To determine the relative tracer concentration (C/C_0) in the sample and to obtain C/C_0 profiles, time-series values for $\Delta\mu$ ($\Delta\mu_t$) are normalized to its final values ($\Delta\mu_s$) acquired when the tracer concentration in the sample is fully homogeneous and equal to the constant concentration at the influx boundary (Eq. 1.13, Cavé et al., 2009). D_p is then estimated by visually fitting the experimental C/C_0 data to an analytical solution for Fick's second law (Fig. 1.8a):

$$\left(\frac{C}{C_0}\right) = \frac{(\Delta\mu_t)_x}{(\Delta\mu_s)_x} \quad [1.13]$$

where, C represents the tracer concentration at a distance x from the influx boundary; C_0 is the constant tracer concentration at the influx boundary.

An iodide (I^-) tracer is commonly used with the X-ray radiography method because of its high atomic number (Z=53) and conservative geochemical behaviour (Tidwell et al., 2000). The technique has been successfully applied for Ordovician shales of the Michigan Basin to obtain diffusion coefficients under saturated and partially-saturated conditions (Queenston Formation; Cavé et al., 2009; Nunn et al., 2018), to study diffusion anisotropy (Queenston, Georgian Bay and Blue Mountain Formations; Xiang et al., 2013), and to determine diffusion-reaction parameters in shale using cesium (Cs^+), a reactive tracer also appropriate for X-ray radiography due to its high atomic number (Loomer et al., 2013).

1.3.3. Challenges with low-porosity rocks

Altman et al. (2004) and Cavé et al. (2009) encountered difficulties discriminating the signal of the tracer from the background noise when attempting to estimate diffusion coefficients using X-ray radiography in low-porosity rocks (< 2 %). The signal-to-noise ratio (SNR) is a parameter that reflects image quality as it compares the amount of background noise to that of the desired signal (Welvaert and Rosseel, 2013): above some threshold level of SNR, the attenuation (signal) caused by

a diffusing tracer can be clearly differentiated from the background. In low-porosity rocks, the SNR is low because the mass of tracer in the sample is limited by the small pore volume. Fig. 1.8 shows C/C_0 profiles for shale (~ 8% porosity) and limestone (~ 2% porosity), illustrating the effect of low SNR for the limestone relative to the shale. The SNR can be improved by minimizing image-registration errors during the difference-imaging process, and increasing the source beam current to improve the photon-counting statistics.

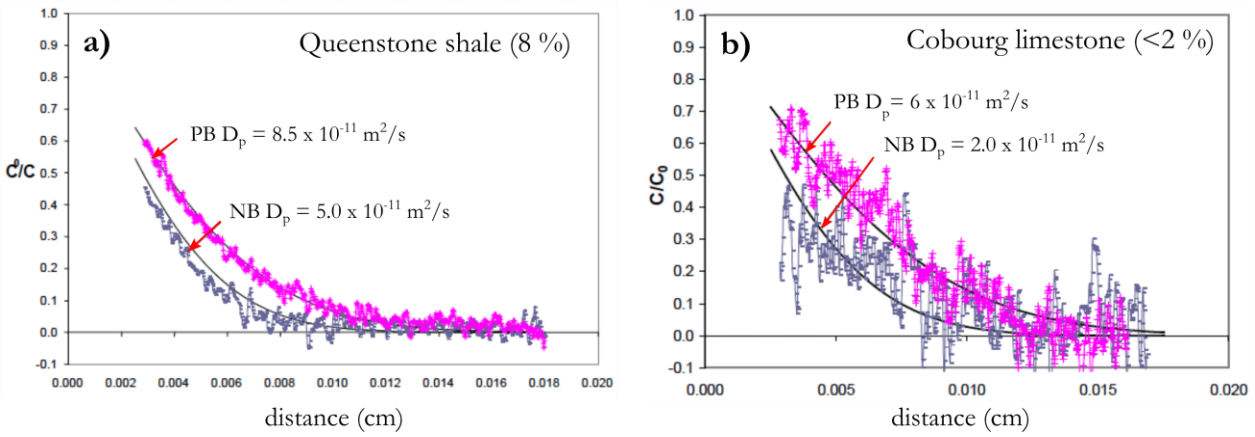

Figure 1.8. Relative I^- concentration profiles (C/C_0) and D_p obtained for **a)** Queenstone shale and **b)** Cobourg limestone. Sample porosities are indicated in brackets; PB: parallel to bedding; NB: normal to bedding (from Al et al., 2010).

1.4. Objectives

The main objective of this research was to refine the X-ray radiography method developed by Cavé et al. (2009) to detect I^- concentrations and quantify diffusion in rocks with porosities below 2%. The focus was to improve the SNR and to test the method on larger samples. The experiments were carried out on samples from the Cobourg Formation, an argillaceous limestone from the Michigan Basin, and on granitic rocks from the Lac du Bonnet Batholith in Manitoba.

1.5. Thesis organization

This thesis is organized to reflect the main outcome of the research and consists of three chapters and four appendices.

Chapter 1 covers the background, including relevant concepts and justification for this investigation. Chapter 2 was prepared to be submitted for publication in a peer-reviewed academic journal and presents the findings of the experiments using I^- tracer in argillaceous limestone. Chapter 3 summarizes the conclusions from this research.

The work on method development to improve the SNR in granitic rocks (Lac du Bonnet Batholith samples) did not achieve a satisfactory outcome, thus those results are not presented in the main body of the thesis; they are shown in Appendix A. Appendix B describes the experimental work done on standards used for calibration, Appendix C shows the petrographic analysis carried out on the Cobourg Formation samples and appendix D presents the remaining of the Cobourg Formation diffusion profiles.

1.6. References

Aichinger, H., Dierker, J., Joite-Barbfuß, S., Säbel, M., 2012. Radiation exposure and image quality in X-ray diagnostic radiology - physical principles and clinical applications, 2nd ed. Springer-Verlag Berlin Heidelberg.

Al, T.A., Clark, I.D., Kennell, L., Jensen, M., Raven, K.G., 2015. Geochemical evolution and residence time of porewater in low-permeability rocks of the Michigan Basin, Southwest Ontario. Chem. Geol. 404, 1–17.

Al, T.A., Xiang, Y., Cavé, L., 2010. Measurement of diffusion properties by X-ray radiography and by through-diffusion techniques using iodide and tritium tracers: core samples from OS-1 and DGR-2 (Technical Report No. TR-07-17, Revision 3). Intera Engineering Ltd., University of New Brunswick.

Altman, S.J., Uchida, M., Tidwell, V.C., Boney, C.M., Chambers, B.P., 2004. Use of X-ray absorption imaging to examine heterogeneous diffusion in fractured crystalline rocks. J. Contam. Hydrol. 69, 1–26. https://doi.org/10.1016/S0169-7722(03)00153-0

Altmann, S., Tournassat, C., Goutelard, F., Parneix, J.-C., Gimmi, T., Maes, N., 2012. Diffusion-driven transport in clayrock formations. Appl. Geochem. 27, 463–478. https://doi.org/10.1016/j.apgeochem.2011.09.015

Anovitz, L.M., Cole, D.R., 2015. Characterization and Analysis of Porosity and Pore Structures. Mineral. Soc. Am., Reviews in Mineralogy and Geochemistry 80, 61–164.

Beauheim, R.L., Roberts, R.M., Avis, J.D., 2014. Hydraulic testing of low-permeability Silurian and Ordovician strata, Michigan Basin, southwestern Ontario. J. Hydrol. 509, 163–178. https://doi.org/10.1016/j.jhydrol.2013.11.033

Bredehoeft, J.D., England, A.W., Stewart, D.B., Trask, N.J., Winograd, I.J., 1985. Geologic Disposal of High-Level Radioactive Wastes- Earth-Science Perspectives (Circular 779). U.S. Geological Survey, Alexandria, VA.

Brown, A., Soonawala, N.M., Everitt, R.A., Kamineni, D.C., 1989. Geology and geophysics of the Underground Research Laboratory site, Lac du Bonnet Batholith, Manitoba. Can. J. Earth Sci. 26, 404–425. https://doi.org/10.1139/e89-037

Cavé, L., Al, T., Xiang, Y., Vilks, P., 2009. A technique for estimating one-dimensional diffusion coefficients in low-permeability sedimentary rock using X-ray radiography: Comparison with through-diffusion measurements. J. Contam. Hydrol. 103, 1–12. https://doi.org/10.1016/j.jconhyd.2008.08.001

Clark, I.D., Al, T., Jensen, M., Kennell, L., Mazurek, M., Mohapatra, R., Raven, K.G., 2013. Paleozoic-aged brine and authigenic helium preserved in an Ordovician shale aquiclude. Geology 41, 951–954. https://doi.org/10.1130/G34372.1

Crank, J., 1975. The Mathematics of Diffusion, Second Edition. ed. Oxford University Press, Oxford.

Engström, J., Front, K., Gehör, S., Kosunen, P., Kärki, A., Mattila, J., Paananen, M., Paulamäki, S., 2016. Geology of Olkiluoto. Posiva.

Epstein, N., 1989. On tortuosity and the tortuosity factor in flow and diffusion through porous media. Chem. Eng. Sci. 44, 777–779. https://doi.org/10.1016/0009-2509(89)85053-5

Garamszenghy, M., 2015. Nuclear fuel waste projections in Canada – 2015 Update (No. NWMO TR-2015-19). Nuclear Waste Management Organization.

García-Gutiérrez, M., Cormenzana, J.L., Missana, T., Mingarro, M., 2004. Diffusion coefficients and accessible porosity for HTO and 36-Cl in compacted FEBEX bentonite. Appl. Clay Sci. 26, 65–73.

Ghanbarian, B., Hunt, A.G., Ewing, R.P., Sahimi, M., 2013. Tortuosity in porous media: a critical review. Soil Sci. Soc. Am. J. 77, 1461–1477. https://doi.org/10.2136/sssaj2012.0435

Gimmi, T., Leupin, O.X., Eikenberg, J., Glaus, M.A., Van Loon, L.R., Waber, H.N., Wersin, P., Wang, H.A.O., Grolimund, D., Borca, C.N., Dewonck, S., Wittebroodt, C., 2014. Anisotropic diffusion at the field scale in a 4-year multi-tracer diffusion and retention experiment – I: Insights from the experimental data. Geochim. Cosmochim. Acta 125, 373–393. https://doi.org/10.1016/j.gca.2013.10.014

Grathwohl, P., 1998. Diffusion in Natural Porous Media: Contaminant Transport, Sorption/Desorption and Dissolution Kinetics, Topics in Environmental Fluid Mechanics. Springer US. https://doi.org/10.1007/978-1-4615-5683-1

Guo, R., 2017. Thermal response of a Canadian conceptual deep geological repository in crystalline rock and a method to correct the influence of the near-field adiabatic boundary condition. Eng. Geol. 218, 50–62. https://doi.org/10.1016/j.enggeo.2016.12.014

Hussein, E.M.A., 2007. Radiation Mechanics, Principles and Practice, 1st ed. Elsevier, UK. https://doi.org/10.1016/B978-0-08-045053-7.X5000-9

IAEA, 2019. Energy, electricity and nuclear power estimates for the period up to 2050, Reference Data Series. International Atomic Energy Agency, Vienna.

IAEA, 2009. Classification of Radioactive Waste (No. GSG-1), IAEA Safety Standards Series No. GSG-1. International Atomic Energy Agency, Vienna.

IAEA, 2008. Estimation of global inventories of radioactive waste and other radioactive materials. International Atomic Energy Agency, Vienna.

Jussiani, E.I., Appoloni, C.R., 2015. Effective atomic number and density determination of rocks by X-ray microtomography. Micron v. 70, 1–6. https://doi.org/10.1016/j.micron.2014.11.005
Ketcham, R.A., Carlson, W.D., 2001. Acquisition, optimization and interpretation of X-ray computed tomographic imagery: applications to the geosciences. Comput. Geosci. 27, 381–400. https://doi.org/10.1016/S0098-3004(00)00116-3
Loomer, D.B., Scott, L., Al, T.A., Mayer, K.U., Bea, S., 2013. Diffusion–reaction studies in low permeability shale using X-ray radiography with cesium. Appl. Geochem. 39, 49–58. https://doi.org/10.1016/j.apgeochem.2013.09.019
Manohara, S.R., Hanagodimath, S.M., Thind, K.S., Gerward, L., 2008. On the effective atomic number and electron density: A comprehensive set of formulas for all types of materials and energies above 1keV. Nucl. Instrum. Methods Phys. Res. Sect. B Beam Interact. Mater. At. 266, 3906–3912. https://doi.org/10.1016/j.nimb.2008.06.034
McGinnes, D.F., 2007. Waste sources and classification, in: Radioactivity in the Environment. Elsevier, pp. 8–40. https://doi.org/10.1016/S1569-4860(06)09002-4
McKinley, I.G., Russell Alexander, W., Blaser, P.C., 2007. Development of geological disposal concepts, in: Radioactivity in the Environment. Elsevier, pp. 41–76. https://doi.org/10.1016/S1569-4860(06)09003-6
Milliken, K.L., Curtis, M.E., 2016. Imaging pores in sedimentary rocks: foundation of porosity prediction. Mar. Pet. Geol. 73, 590–608.
Murty, R.C., 1965. Effective atomic numbers of heterogeneous materials. Nature 398–399. https://doi.org/10.1038/207398a0
Nunn, J.A., Xiang, X., Al, T.A., 2018. Investigation of partial water saturation effects on diffusion in shale. Appl. Geochem. 93–101. https://doi.org/10.1016/j.apgeochem.2018.08.004
Patel, S., 2017. OPG: Kincardine Nuclear Waste Deep Geologic Repository is best alternative [WWW Document]. POWER Mag. URL https://www.powermag.com/opg-kincardine-nuclear-waste-deep-geologic-repository-is-best-alternative/ (accessed 4.28.20).
Pearson, F.J., 1999. What is the porosity of a mudrock?, in: Aplin, A.C., Fleet, A.J., Macquaker, J.H.S. (Eds.), Muds and Mudstones: Physical and Fluid Flow Properties, Special Publication 158. The Geological Society of London, pp. 9–20.
Philibert, J., 2005. One and a Half Century of Diffusion: Fick, Einstein, before and beyond. Open-Access J. Basic Princ. Diffus. Theory Exp. Appl., Diffusion Fundamentals 2, 1–20.
Polak, A., Grader, A.S., Wallach, R., Nativ, R., 2003. Chemical diffusion between a fracture and the surrounding matrix: Measurement by computed tomography and modeling. Water Resour. Res. 39, 1–14.
Raven, K., McCreath, D., Jackson, R., Clark, I.D., Heagle, D., Sterling, S., Avis, J.D., 2010. Descriptive Geosphere Site Model, Deep Geologic Repository Bruce Nuclear Site (No. PR-08-01 Revision 1C), DGR Site Characterization Document. Intera Engineering Ltd.
Rueden, C.T., Schindelin, J., Hiner, M.C., DeZonia, B.E., Walter, A.E., Arena, E.T., Eliceiri, K.W., 2017. ImageJ2: ImageJ for the next generation of scientific image data. BMC Bioinformatics 18, 529. https://doi.org/10.1186/s12859-017-1934-z
Selman, J., 2000. Fundamentals of Imaging Physics and Radiobiology. Charles C. Thomas Publisher, Limited.
Shackelford, C.D., 1991. Laboratory diffusion testing for waste disposal — A review. J. Contam. Hydrol. 7, 177–217. https://doi.org/10.1016/0169-7722(91)90028-Y
Shackelford, C.D., Moore, S.M., 2013. Fickian diffusion of radionuclides for engineered containment barriers: Diffusion coefficients, porosities, and complicating issues. Eng. Geol. 152, 133–147.
Singhal, B.B.S., Gupta, R.P., 2010. Applied hydrogeology of fractured rocks, 2nd ed. Springer Science+Business Media B.V.

Sprawls, P., 2019. Interaction of radiation with matter [WWW Document]. Phys. Princ. Med. Imaging. URL http://www.sprawls.org/ppmi2/INTERACT/#INTRODUCTION (accessed 1.13.20).

Tidwell, V.C., Glass, R.J., 1994. X ray and visible light transmission for laboratory measurement of two-dimensional saturation fields in thin-slab systems. Water Resour. Res. 30, 2873–2882. https://doi.org/10.1029/94WR00953

Tidwell, V.C., Meigs, L.C., Christian-Frear, R., Boney, C.M., 2000. Effects of spatially heterogeneous porosity on matrix diffusion as investigated by X-ray absorption imaging. J. Contam. Hydrol. 42, 285–302. https://doi.org/10.1016/S0169-7722(99)00087-X

van Brakel, J., Heertjes, P.M., 1974. Analysis of diffusion in macroporous media in terms of a porosity, a tortuosity and a constrictivity factor. Int. J. Heat Mass Transf. 17, 1093–1103. https://doi.org/10.1016/0017-9310(74)90190-2

Van Geet, M., Swennen, R., Wevers, M., 2000. Quantitative analysis of reservoir rocks by microfocus X-ray computerised tomography. Sediment. Geol. 132, 25–36. https://doi.org/10.1016/S0037-0738(99)00127-X

Vilks, P., Cramer, J.J., Jensen, M., Miller, N.H., Stanchell, F.W., Miller, H, 2003. In situ diffusion experiment in granite: Phase I. J. Contam. Hydrol. 61, 191–202. https://doi.org/10.1016/S0169-7722(02)00135-3

Watson, E.B., Baxter, E.F., 2007. Diffusion in solid-Earth systems. Earth Planet. Sci. Lett. 253, 307–327. https://doi.org/10.1016/j.epsl.2006.11.015

Welvaert, M., Rosseel, Y., 2013. On the definition of signal-to-noise ratio and contrast-to-noise ratio for fMRI data. PLoS ONE 8, e77089. https://doi.org/10.1371/journal.pone.0077089

Wilson, C.R., Witherspoon, P.A., Long, J.C.S., Galbraith, R.M., DuBois, A.O., McPherson, M.J., 1983. Large-scale Hydraulic Conductivity Measurements in Fractured Granite. Int. J. Rock Mech. Min. Sci. Geomech. Abstr. 26, 279–286.

Witherspoon, P.A., Bodvarsson, G.S. (Eds.), 2006. Geological Challenges in Radioactive Waste Isolation, Fourth Worldwide Review. University of California, Earth Sciences Division.

Xiang, Y., Al, T., Scott, L., Loomer, D., 2013. Diffusive anisotropy in low-permeability Ordovician sedimentary rocks from the Michigan Basin in southwest Ontario. J. Contam. Hydrol. 155, 31–45.

Yoon, H., Kang, Q., Valocchi, A.J., 2015. Lattice Boltzmann-Based Approaches for Pore-Scale Reactive Transport. Mineral. Soc. Am., Reviews in Mineralogy and Geochemistry 80, 393–431.

Chapter 2

IODIDE BEHAVIOUR IN ARGILLACEOUS LIMESTONE: INSIGHTS FROM X-RAY RADIOGRAPHY

2.1. Introduction

2.1.1. The conundrum of iodide transport in clay-rich rocks

Safe disposal of nuclear waste is a pressing matter in countries with nuclear energy programs. To ensure that waste is isolated from the biosphere for time scales exceeding 100 000 years, deep burial in geologically stable sites where the host rock formation can prevent the outward migration of radionuclides is seen as the most effective long-term solution (OECD/NEA, 2008). The challenge is, however, to demonstrate with confidence that the host rocks of a deep geological repository (DGR) will serve as an effective natural barrier. Rocks with very low hydraulic conductivity are considered suitable for this role, and of particular interest are argillaceous rocks because, among other advantages, their low permeability ($k \sim 10^{-19}$ to 10^{-21} m^2) results in diffusion-dominated solute transport (Boving and Grathwohl, 2001; Neretnieks, 1980; Selvadurai and Najari, 2016), their high adsorption capacity can slow down radionuclide migration (Altmann, 2008; Sawhney, 1972; Weber et al., 1991), and their plasticity may lead to an effective self-sealing of fractures (Dohrmann et al., 2013; Mazurek et al., 2009; Roxburgh, 1987; Tournassat et al., 2015).

Over the past two decades a large body of work has been focused on measurement of solute mass transport by diffusion (e.g. Boving and Grathwohl, 2001; Cavé et al., 2009; Chen et al., 2014; Descostes et al., 2008; Loomer et al., 2013; Van Loon and Mibus, 2015). Solute-specific diffusion coefficient measurements in clay-rich formations are key for site characterization and performance assessment. Most of the measurements have been obtained using bulk techniques including in-, out- and through-diffusion experiments with a variety of tracers that are considered to behave

conservatively, such as water isotopes (e.g. HDO, HTO) and anions (e.g. Cl^-, Br^-, I^-; Appelo et al., 2010; Appelo and Wersin, 2007; García-Gutiérrez et al., 2004; Vilks et al., 2003) where the tracer flux is estimated with Fick's laws presuming a homogeneous medium and constant mass flow. The diffusivity of anionic species is known to be slower than of water isotopes because of the anion exclusion effect (Bolt and de Haan, 1979; Descostes et al., 2008; Van Loon et al., 2007); however various studies have shown that iodide (I^-) flux is notably retarded relative to chloride (Cl^-), suggesting a non-conservative behaviour of I^- (Appelo et al., 2010; Van Loon et al., 2003a, 2003b). A significant collective work has been carried out to understand I^- transport mechanisms in clay-rich formations but there is no scientific consensus on its behaviour to date. Previous research exploring its diffusion and adsorption properties commonly show contradictory results. On the one hand, for a given set of samples, a large range of distribution coefficients (e.g. K_d = 0.004 to 0.15 mL/g, Bazer-Bachi et al., 2006) has been reported, as well as different rock capacity factor values depending on whether the tracer diffuses in or out of the sample (e.g. Glaus et al., 2008; Savoye et al., 2006; Van Loon et al., 2003a, 2003b), and conversely, some studies show K_d values indicating no adsorption at all (e.g. Savoye et al., 2012). It has been suggested that I^- uptake by minerals and rocks is sensitive to the initial iodide tracer concentration, noticing no measurable I^- uptake when experiments are conducted with high tracer concentrations (i.e. 10^{-3} M) but adsorption is detected when experiments are conducted using lower tracer concentrations (below 10^{-6} M; Aimoz et al., 2011; Bazer-Bachi et al., 2006; Descostes et al 2008; Frasca et al., 2012; Van Loon et al., 2003b; Wittebroodt et al., 2012, 2008), yet some works show no effect of initial tracer concentration (high or low) on I^- adsorption Glaus et al., 2008; Savoye et al., 2012). The inconsistencies have been linked to experimental artifacts (Glaus et al., 2008), isotopic exchange between the tracer and the sample (Tournassat et al., 2007), co-precipitation of I^- with calcium carbonate (Claret et al., 2010), or adsorption by the various mineral phases composing the argillaceous sample (pyrite, Fe-oxides, carbonates and organic matter; Altman et al. 2008; Claret et al. 2010; Frasca et al., 2012). Nevertheless, experiments carried out

under strictly controlled conditions to avoid oxidation (e.g. N_2/CO_2 atmosphere and controlled P_{CO2}) and controlling the purity of tracer solutions, still indicate small but significant I^- retention, making it difficult to propose an adsorption mechanism (e.g., Frasca et al., 2012; Glaus et al., 2008; Montavon et al., 2014; Wittebroodt et al., 2012).

These unresolved issues highlight the unique characteristics of I^- and its particular interaction with the solid medium within which it diffuses, in addition to the limitations of the long-established diffusion and adsorption methods used. Iodine species are sequestered by geological materials due in part to variations in redox state, which control its fate and transport (Whitehead, 1984). Furthermore, laboratory studies conducted on crushed samples potentially increment the risk of experimental artifacts. By crushing the sample, the surface area is increased and I^- can gain access to previously unavailable reactive surfaces sites, not to mention the disturbance to the pore sizes and distribution, a major control in the diffusion and adsorption of anionic species. In the case of in- or out-diffusion experiments using intact samples, the data reflect the behavior of the tracer in the bulk sample and do not allow an evaluation of the spatial relationships between tracers and the variable mineralogical and porosity characteristics.

2.1.2. X-ray radiography to investigate diffusion in heterogeneous media

Published studies have demonstrated that argillaceous rocks are anisotropic due to their sedimentary origin, with preferential diffusion along bedding planes (Gimmi et al., 2014; Van Loon et al., 2004; Wenk et al., 2008; Xiang et al., 2013). Certainly, geological media are heterogeneous with physical characteristics and chemical properties influenced by their origin and subsequent diagenetic processes. In order to advance our understanding of diffusive transport, it is valuable to obtain spatially resolved information from within the rock and to assess how the porous medium controls the process.

X-ray Radiography (XRR) is a non-destructive technique adapted to investigate matrix diffusion (Tidwell et al., 2000). It is based on the principle of X-ray attenuation by a highly attenuating tracer in a sample that is imaged repeatedly through time during a diffusion experiment. Iodide tracer solutions are commonly used because i) I^- is considered a non-sorbing species, ii) its high atomic number provides effective X-ray attenuation, and iii) it can represent the migration behavior of ^{129}I, an important dose contributor in nuclear waste (Cavé et al., 2009; Davis et al., 1980; Tidwell et al., 2000).

Cavé et al. (2009) estimated diffusion coefficients in laboratory-scale shale samples using XRR and found them to be similar to values obtained by the through-diffusion method, with the additional advantage of acquiring visual evidence of heterogeneity along the diffusion path. Similarly, Nunn et al. (2018) successfully conducted experiments on shales, demonstrating the correlation between porosity and variations in partial gas saturation in partially-saturated samples. While XRR has worked well on relatively high-porosity rocks (> 5%), limitations have been reported on low-porosity materials by Altman et al. (2004) and Cavé et al. (2009) where attempts to measure diffusion in unaltered granodiorite and limestone respectively, did not give reliable results. In rocks with low porosity (e.g. plutonic and metamorphic crystalline rocks and carbonates), the mass of I^- tracer is very small and it is challenging to obtain sufficient contrast (tracer signal) above the ambient noise level (signal-to-noise ratio, SNR). In addition, the relatively high density (2.8 g/cm^3) and high effective atomic number (15.6; Kumar et al., 1996) of calcium-rich carbonate rocks contributes to a low SNR, limiting further the use of the method on geological materials with these characteristics.

In our research, we focused on improving the SNR and monitoring the diffusion of I^- tracer in the Cobourg Formation, an argillaceous limestone formerly considered a plausible host rock for the long-term storage of low- and intermediate-level radioactive waste in Canada. The Cobourg Formation contains 7-17 % wt % of clay minerals (Koroleva et al., 2009) nevertheless, its geological context and attributes (e.g. low hydraulic conductivity - 4 x 10^{-15} to 3 x 10^{-14} m/s; Beauheim et al.,

2014) resemble those European clay-rich formations that are under investigation for nuclear waste disposal. By extension, this work aims at providing a better understanding of the transport of I^- in argillaceous rocks. ^{129}I is mainly concentrated in intermediate- and high-level nuclear waste (Reiller et al., 2006), and as a dissolved species it will be present in its reduced form as $^{129}I^-$ under the reducing conditions prevailing in the geologic system surrounding a DGR, with no affinity for adsorption to the negatively-charged mineral surfaces (Appelo and Wersin, 2007; Descostes et al., 2008; Shackelford and Moore, 2013; Tournassat and Steefel, 2015). This radionuclide has the potential to travel unretarded through the porous medium and to reach the biosphere because of its long half-life (1.57×10^7 y) and high mobility (ANDRA, 2005). It is of environmental concern because of its tendency to accumulate in living organisms (Reiller et al., 2006), thus understanding its transport behavior is critical for assessing the long-term performance and safety of a nuclear waste repository.

2.2. Materials and methods

2.2.1. Sample origin and description

Samples of the Cobourg Formation used in this study were collected from boreholes drilled at the Bruce nuclear generating station, located 220 km northwest of Toronto, ON, Canada. Data from six boreholes indicate the top is at 645-663 m below ground surface and it is overlain by 200 m of shale (Al et al., 2015; Sterling and Melaney, 2010). The Cobourg Formation was deposited in the Michigan Basin during one of the greatest marine transgressions in the geological record (Brookfield and Brett, 1988 Coniglio et al., 1990). It is divided into two members: the upper Collingwood Member, composed of dark grey to black calcareous shale with thin interbeds of fossiliferous limestone, and the Lower Member, made up of grey, fine-grained limestone and argillaceous limestone with fossiliferous and shaly beds, and nodular texture (NWMO, 2011). Samples of the Lower Member were chosen from two 75 mm-diameter archived core segments from depths of 675

m (DGR3-675.46) and 671 m (DGR4-671.24). The core segments were cut parallel to bedding into 40 mm thick slices with a diamond saw, using water to cool and lubricate the blade. Each slice was then sub-cored using diamond coring bits, producing small cylinders, 40 mm long and 20 mm diameter (Fig. 2.1).

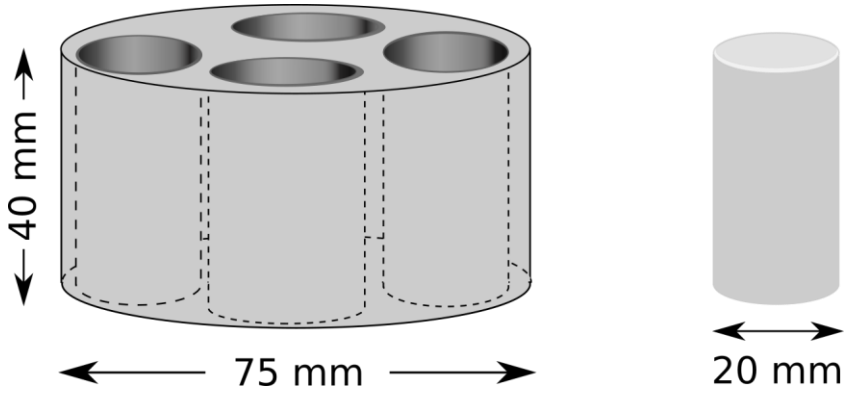

Figure 2.1. Subsampling of the DGR core segments normal to bedding for X-ray radiography.

DGR3-675.46 core is a bioturbated wackestone showing burrow structures and DGR4-671.24 has characteristics of a wackstone interbedded with a packstone. They are composed mainly of calcite, dolomite, clay minerals, pyrite and fossil fragments (primarily bryozoans, crinoids and brachiopods) with the percentages differing between them. The organic matter is mainly of marine origin deposited in a dysoxic environment (Obermajer et al., 1999); the organic carbon content ranges from 0.1 to 2 % wt (Koroleva et al., 2009). A quantitative XRD analysis of the Cobourg Formation from DGR3 core is shown on Table 2.1.

DGR 3			
Minerals	**Wt. %**	**Minerals**	**Wt. %**
Calcite	80.58	Dolomite	3.7
Illite/clays	5.06	Ankerite	2.4
Orthoclase	4.2	Organic carbon	0.921
Quartz	3.2		

Table 2.1. Average mineralogical composition (wt. %) of the Cobourg Formation (DGR3 core) identified by XRD analysis (Wigston and Jackson, 2010).

2.2.2. Water-accessible porosity

Water-accessible porosity (φ_w) was measured on subsamples cut from the 75 mm core segments. The technique consisted of weighing the samples in both water-saturated and dry conditions as described by Xiang et al. (2013). This procedure accounts for the high salinity of the porewater which causes salt precipitation in the pore space of the dried sample. A 28 % salinity correction was used for the calculations based on salinity estimations provided by Xiang et al. (2013).

2.2.3. Synthetic porewater and I^- tracer

The porewater composition of the Cobourg Formation is characterized by very high salinity (3.8 M Cl^-, Xiang et al., 2013) that results from downward migration of hypersaline post-evaporite Silurian brine (Al et al., 2015; Clark et al., 2013). The synthetic porewater (SPW) used in these experiments was prepared to resemble the original porewater composition and ionic strength (Xiang et al., 2013). A 1 M I^- tracer solution was prepared for the diffusion experiments by replacing 1 mol of NaCl by one mol of NaI in the SPW (Table 2.2). Thiosulfate ($Na_2S_2O_3$) was added to keep the solution stable.

Table 2.2. Synthetic porewater (SPW) and I^- tracer solution used for the diffusion experiments.

Ions	SPW (mol/kgw)	Tracer (mol/kgw)
Na^+	2.000	2.000
K^+	0.450	0.450
Ca^{2+}	0.485	0.485
Mg^{2+}	0.200	0.200
Cl^-	3.81	2.81
SO_4^{2-}	0.005	0.005
I^-	-	1.000
Ionic strength	4.51	4.51

2.2.4. X-ray radiography

Experimental set-up

Samples were saturated with the SPW following the method described by Xiang et al. (2014). After saturation was achieved, samples were mounted in Delrin® diffusion cells (Fig. 2.2) similar to the procedure detailed by Loomer et al. (2013), and SPW was added to the tracer reservoir and at the top surface of the sample through a hole in the Delrin® disc to maintain saturation on both ends. The felt disc at the top was kept dampened by adding SPW daily and sealing the hole with a nylon screw. A 3 mm lead ball was attached to the top of the sample to aid in the image registration process. The diffusion experiments were initiated by replacing the SPW from the lower reservoir with I^- tracer solution.

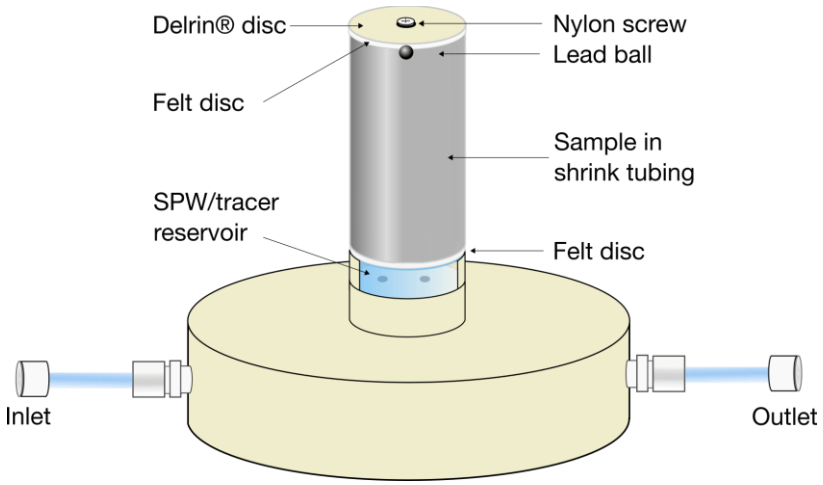

Figure 2.2. Diagram of a sample mounted in the diffusion cell used for X-ray radiography.

Data acquisition and image processing

Immediately after injecting the tracer solution, reference X-ray images were collected for each sample, and subsequent images were obtained every 24 hours for four days, and then in time intervals of 40-48 hours. The tracer solution in the lower reservoir was replaced every 24 hours, and after 90 days the I^- tracer was also added to the top surface of the sample by removing the nylon

screw and submerging the top of the sample in tracer solution, allowing the tracer to diffuse in two directions. When collecting the time-series images, great caution was taken to align them at the same position as for the reference image – also known as image registration. Measurements were conducted using an X-ray imaging system (Pinnacle X-ray Systems, Suwanee, Ga., U.S.A) equipped with an amorphous-silicon flat-panel imaging detector (Varian PaxScan®1313DX), and an stationary anode X-ray source (Varian® NDI-160/22) coupled to a Gulmay® CPL series (CP2-1402) 3 kW generator located in the Department of Earth and Environmental Sciences at the University of Ottawa. The X-ray source voltage and current settings were optimized at 50 kV and 60 mA, acquisition time was 1 frame per second with 32 frames averaged to produce an image. A 3.3 mm aluminum filter was used to condition the beam and minimize beam hardening artefacts, and internal standards made of aluminum and ceramic (Mykroy/Mycalex; McMaster-Carr) were used to correct for variations in the X-ray source. X-ray images were acquired as 1024 x 1024 pixels, 16-bit greyscale radiographs (65 536 greyscale values -gsv-) where each pixel value is a function of the X-ray intensity transmitted through the sample. A simplified modification of the Beer-Lambert Law [Eq. 2.1] best describes the X-ray attenuation caused by the sample. It gives an estimation of the exponential reduction in X-ray intensity (I) with sample thickness (d) through the heterogeneous medium (Cavé et al., 2009).

$$I = I_0^{[-\sum_{i=1}^{n}(\mu_i d_i)]} \qquad [2.1]$$

where I_0 is the initial X-ray intensity and μ_i is the X-ray attenuation coefficient for each mineral constituent (i) of the rock over its linear thickness (d_i).

Radiographs were processed using ImageJ, an open source image analysis program developed at the National Institute of Health in Maryland, U.S.A. (Rueden et al., 2017), following the step-by-step approach described by Cavé et al. (2009), in which the two-dimensional images are converted to one-dimensional profiles of X-ray attenuation (μ) versus distance from the tracer influx boundary.

For a selected region of interest on both the reference, and corresponding time-series radiographs, the process consists of integrating the pixel gsvs across the width of the sample (mean gsv for each pixel row) creating a profile of gsv along the sample length. The constant X-ray attenuation from the mineral solids is effectively removed by using an image-subtraction approach (Altman et al., 2004; Cavé et al., 2009; Tidwell et al., 2000), in which the reference image gsvs ($I_{t=0}$) are subtracted from the time-series gsvs ($I_{t>0}$). The difference is the attenuation caused by the I^- tracer present in the pore space, calculated as:

$$\Delta\mu = [\ln(I_{t=0}) - \ln(I_{t>0})] \quad [2.2]$$

Therefore, the term $\Delta\mu$ in Eq. [2.2] is a function of the mass of I^- tracer in the sample porewater over time.

2.2.5. SEM imaging

After the diffusion experiments ended, the samples were removed from the diffusion cell, cut in half along the core axis and polished thin sections were prepared. The structure and mineralogy of the samples were investigated with optical microscopy and a scanning-electron microscope (SEM; JEOL 6610LV) equipped with an Oxford Inca Energy Dispersive X-ray spectrometry (EDS) system located in the Department of Earth and Environmental Sciences at the University of Ottawa. The SEM/EDS analyses were performed at accelerating voltages of 10 and 20 kV, in high vacuum mode.

2.3. Results and discussion

2.3.1. Water-accessible porosity

The results of the φ_w measurements range from 1.2 % (DGR3-675.46) to 1.3 % (DGR4-671.24). These measurements are in agreement with porosities reported for the same unit by Al et al., 2010a, 2010b) and Xiang et al. (2013).

2.3.2. X-ray and SEM analysis

The profiles of mean gsv vs distance prior to tracer addition for samples DGR3-675.46-c and DGR4-671.24-a display significant variability along the sample length (Figs. 2.3 A and B), with high gsv indicating regions in the rock that are less attenuating to the X-ray beam and low gsv denoting zones where the X-rays are considerably attenuated. As X-ray attenuation is a function of density and atomic number, the gsv fluctuations indicate spatial variations in rock density, mineralogy and porosity. Comparison of the gsv profiles with the polished thin sections (Figs. 2.3 C and D) demonstrates that the high gsvs correlate to clay- and organic-rich domains that appear as dark wavy laminations. In contrast, the low gsvs correspond with bioturbated carbonate- and bioclast-dominated lenses. Clay- and organic-rich sedimentary rocks have relatively low X-ray attenuation coefficients due to the low atomic number of their constituents (silicon, Z=14; aluminum, Z=13; and carbon, Z=6), and low density (as low as 1.3 g/cm^3; Schön, 2011). Conversely, calcium-rich minerals and rocks have higher X-ray attenuation coefficients because of the higher atomic number of calcium (Z=20) and the higher density of carbonate minerals (2.7 – 2.9 g/cm^3; Schön, 2011). Since rocks are composed of different chemical elements in varying proportions, the absorption of X-rays in such complex materials is better represented in terms of their density, more specifically their electron density, and effective atomic number (Z_{eff}). Z_{eff} is a parameter that is used to represent the interaction of X-rays with a composite medium where Z_{eff} is weighted proportionally to the elemental

fractions and atomic numbers (Manohara et al., 2008). Various approaches are used to calculate Z_{eff}, Eq. [2.3] is based on Boespflug et al. (1994).

$$Z_{eff} = \sqrt[3.8]{f_1(Z_1)^{3.8} + f_n}(Z_n)^{3.8} \quad [2.3]$$

where: *f* is the elemental fraction and *n* is the number of elements in the material.

Z_{eff} of a given material varies with the photon energy (Akça and Erzeneoğlu, 2014). The experimental values obtained for calcite, illite and smectite in an energy range similar to that used in this study (below 80 kV) are 15.80, 12.79 and 10.85 respectively (Kumar et al., 1996). Higher Z_{eff} values indicate higher attenuation.

The Δμ versus distance profiles for DGR3-675.46-c and DGR4-671.24-a samples (Figs. 2.3 A and B) indicate changes in X-ray attenuation caused by the tracer diffusion - Δμ increases with time. The Δμ time-series profiles obtained at 1, 3, and 11 days for sample DGR3-675.46-c indicate tracer transport consistent with diffusion in a near homogeneous porous medium; however, data acquired after 48 days reveal more irregular Δμ profiles. After 48 days, discrete humps appear in the profiles at distances of approximately 6 and 11 mm. These features become more pronounced with time, and after 105 and 152 days the Δμ profiles display anomalously high values near the top boundary (approximately 30 to 35 mm). These elevated values for Δμ indicate accumulation of tracer in those regions; a visual comparison with the polished thin section (Fig. 2.3 C) indicates correlation between tracer accumulation and the dark, clay- and organic-rich zones.

Similar to the Δμ profile for sample DGR3-675.46-c, the profile for sample DGR4-671.24-a is relatively smooth at early time as would be expected for diffusion in a homogeneous medium, but with increasing time the Δμ profile becomes uneven, indicating heterogeneous tracer distributions (Fig. 2.3 B). Distinct perturbations appear between 2 and 4 mm, from 9 to 15 mm, from 26 to 28 mm and from 32 to 35 mm distance. Comparison with the physical characteristics of the

corresponding thin section again indicates that the tracer accumulation coincides with clay- and organic-rich zones in the rock (Fig. 2.3 D).

Given the observation of anomalous accumulations of the tracer in some regions of the samples, SEM imaging and EDS analyses were performed with special emphasis on those areas, in an effort to investigate the mineralogy and its role in tracer adsorption. Backscattered electron images (BSE) of selected regions (ROI 1-6, Figs. 2.3 C and D) confirm that the dark areas and laminae are characterized by a fine-grained matrix with concentrations of Si, Al and K, consistent with clay mineralogy. For example, in DGR3-675.46-c the moderate tracer accumulation close to the inlet boundary (approximately 6 and 11 mm; Fig. 2.3 C, ROI 1 and 2) occurs in a region distinguished by concentrically-zoned dolomite crystals, and pyrite crystals and framboids supported in a fine-grained matrix that contains organic matter (Fig. 2.4 a-c, spot 1). Near the top boundary where elevated tracer accumulation is observed (Fig. 2.3 C, ROI 3), the fine- grained matrix and organic matter are more abundant. In DGR4-671.24-a, the SEM images of ROI 4, 5 and 6 (Fig. 2.3 D) also corroborate that tracer accumulation takes places in argillaceous-rich areas (Fig. 2.6 e-f). EDS analyses confirm clay components and reveal carbon and sulphur peaks are common in the organic matter but iodine peaks are unusual (Fig. 2.5, spots 1 and 2). A limitation of EDS analysis is the difficulty of differentiating the I $L\alpha$ emission (3.9 keV) from the Ca $K\alpha$ emission (3.69 keV); however, data collected from organic matter in sample DGR4-671.24-a exhibit a clear I peak that is distinct from Ca (Fig. 2.6e, spot 1). Marine organic matter contains iodine that may be preserved after its decomposition (Ullman and Aller, 1985), thus the iodine concentration detected may not be related to diffusion of the tracer.

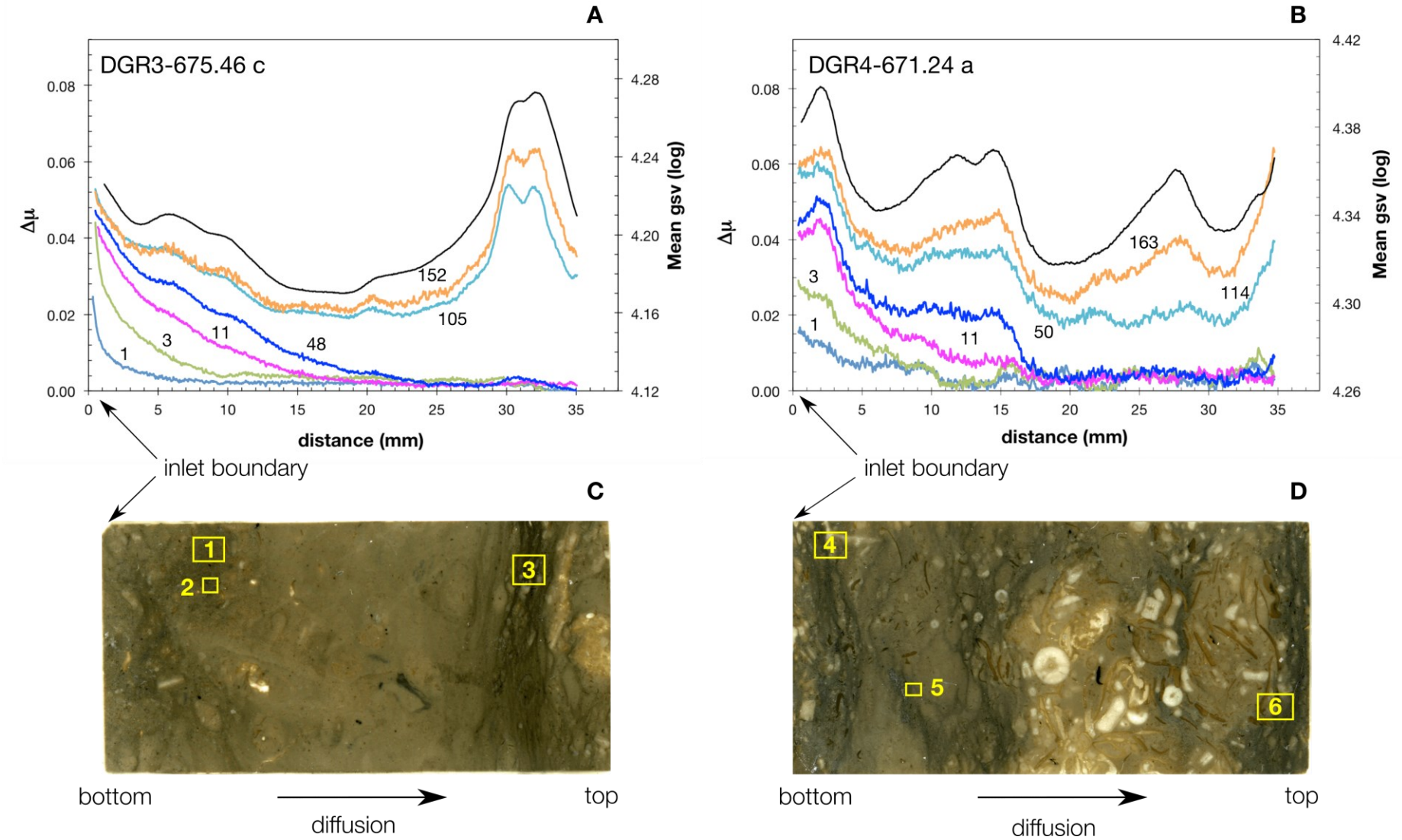

Figure 2.3. **A and B**: profiles of mean greyscale values prior to addition of tracer (black solid line, right axis), and Δμ (coloured lines, left axis) versus distance after the addition of tracer, for samples DGR3-675.46-c and DGR4-671.24-a. The numbers next to the Δμ profiles indicate the number of days after the diffusion experiment started. **C and D:** polished thin sections from samples DGR3-675.46-c and DGR4-671.24-a, cut along the core axis, perpendicular to the X-ray path, after diffusion experiments ended. SEM-BSE images and EDS analyses were conducted on regions of interest (ROI) marked 1 to 6 (yellow squares).

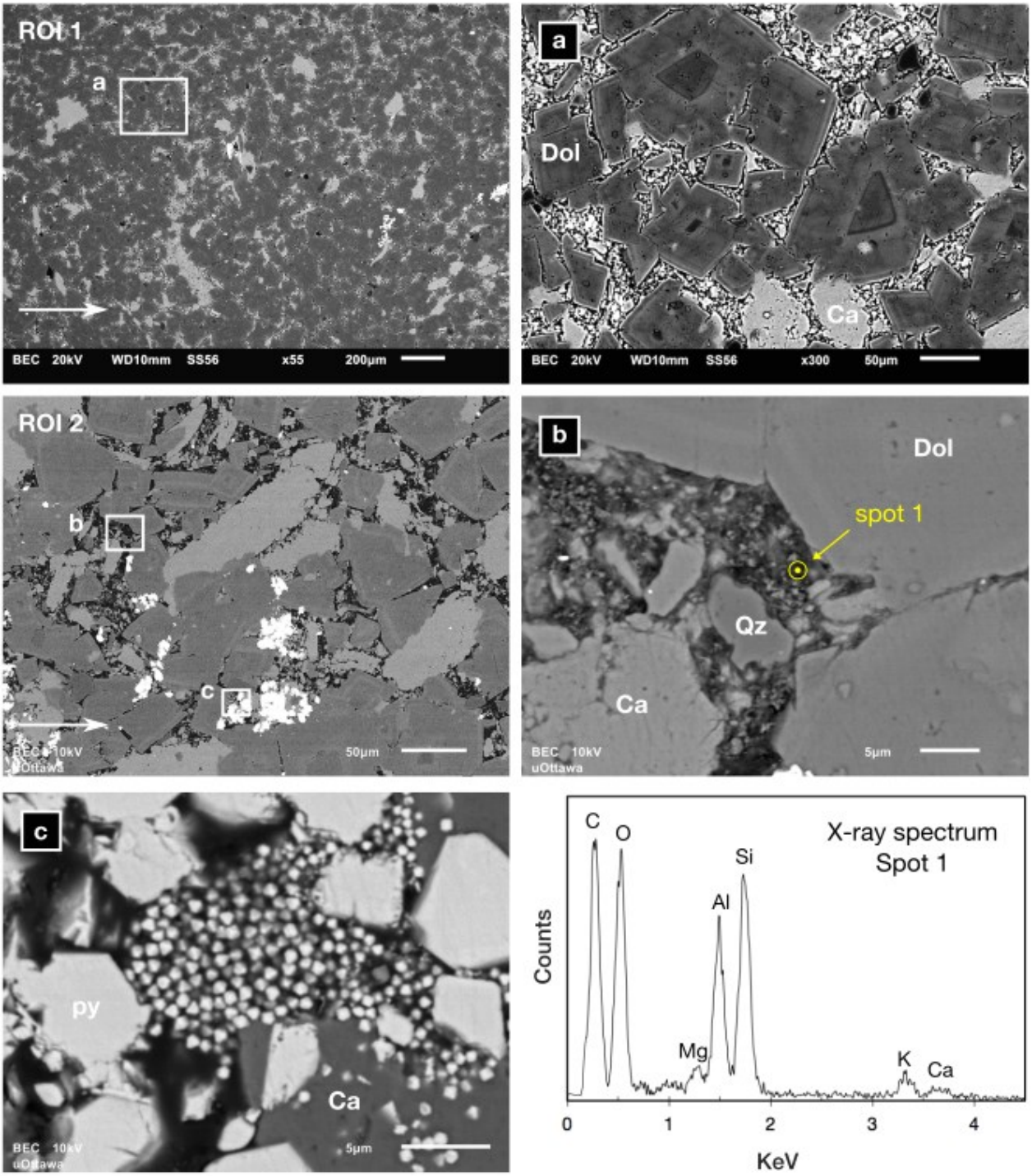

Figure 2.4. ROI 1 and ROI 2 from the lower section of DGR3-675.46-c. Large arrows show the direction of diffusion, white rectangular areas in the images at left are magnified in the images at right and at the bottom. **a)** Concentrically-zoned dolomite (Dol) and calcite (Ca) grains in fine-grained matrix. **b)** Detail of the supporting matrix. X-ray spectrum (spot 1) confirms clay mineralogy and organic matter. **c)** Pyrite (py) crystals and framboids within organic matter (black) and calcium carbonate minerals (Ca).

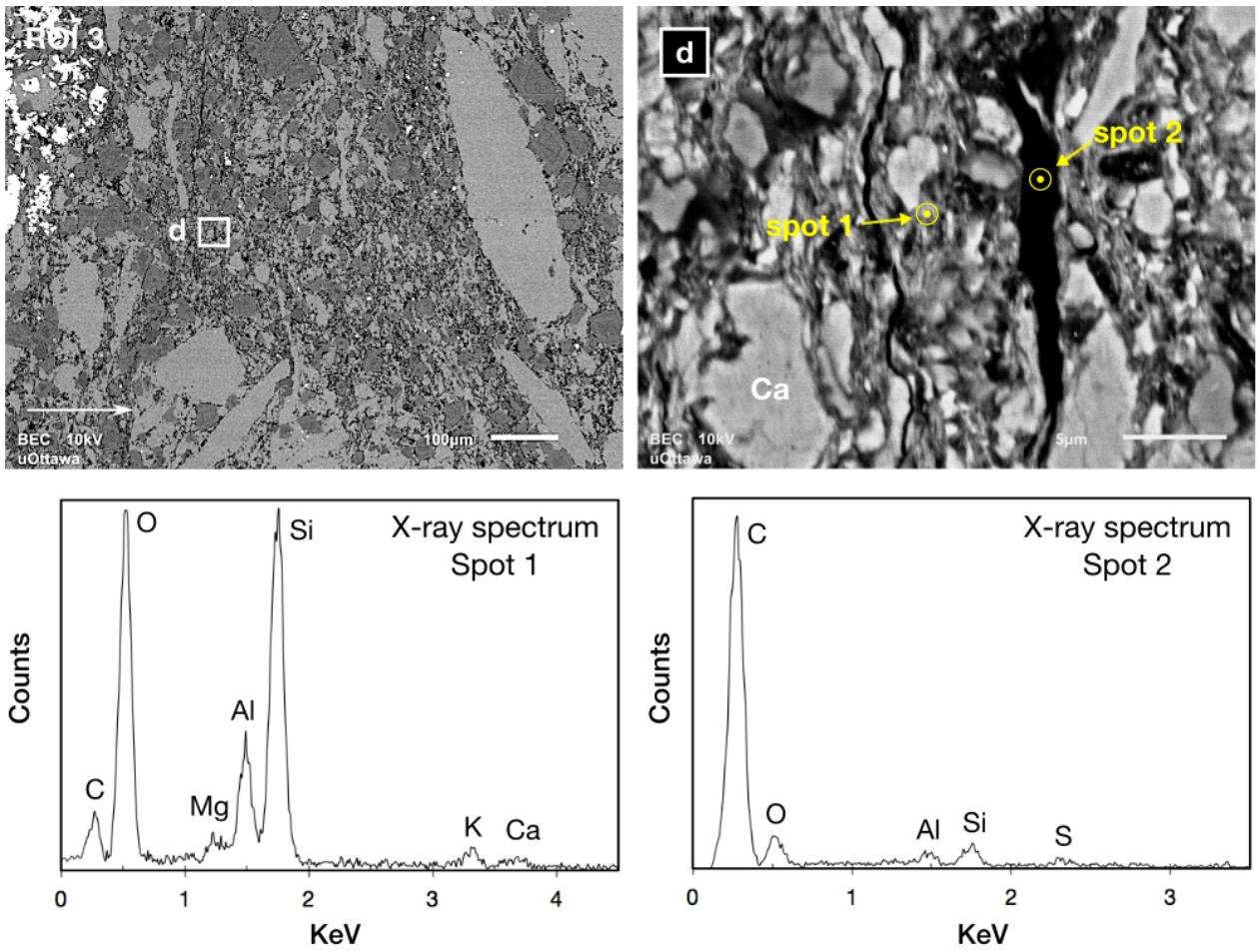

Figure 2.5. BSE image of DGR3-675.46-c, ROI 3. The magnified area on the right (**d**) shows carbonate minerals (Ca) and laminated organic matter preserved in a clay-rich matrix confirmed by X-ray spectra (spots 1 and 2).

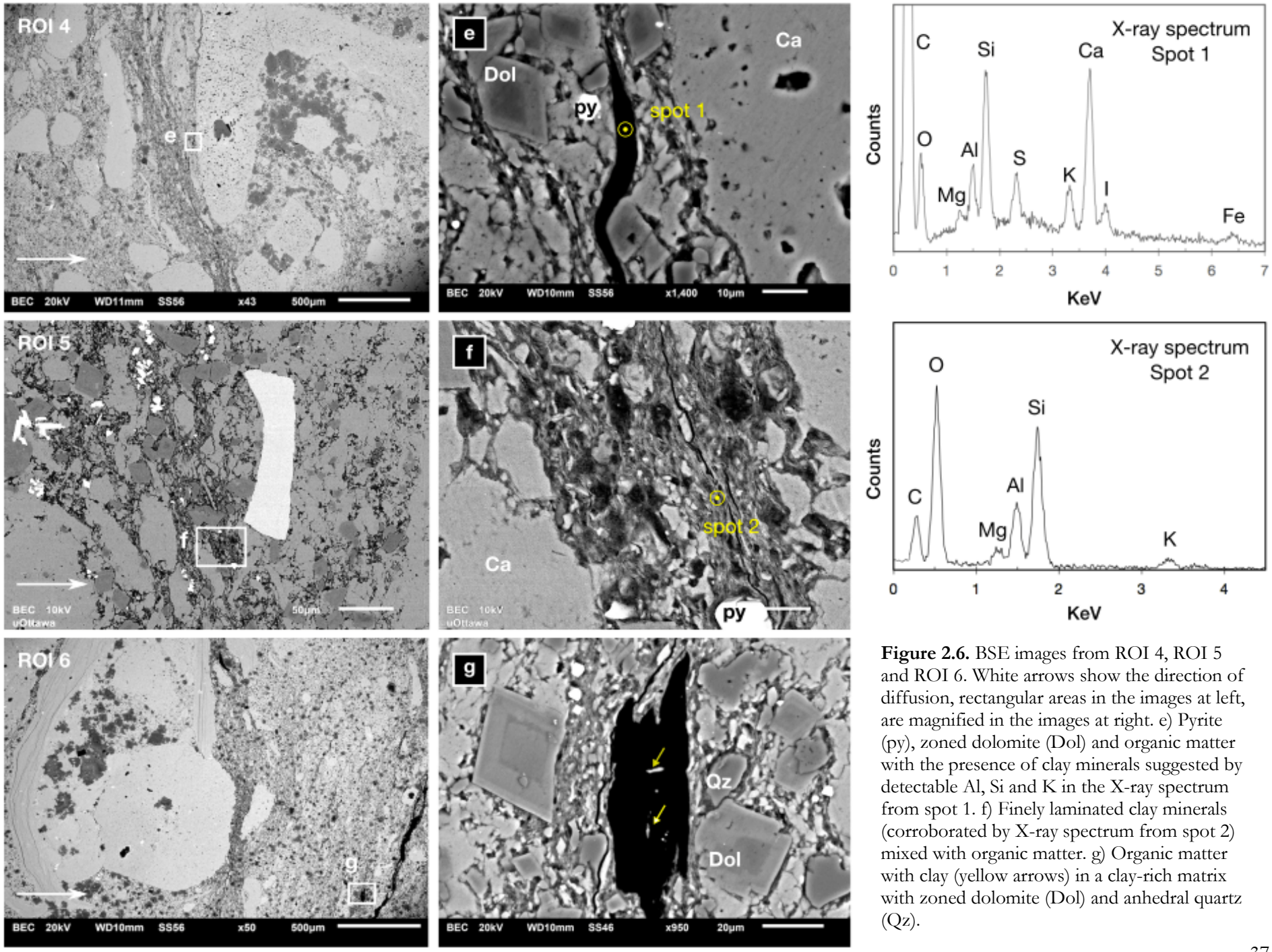

Figure 2.6. BSE images from ROI 4, ROI 5 and ROI 6. White arrows show the direction of diffusion, rectangular areas in the images at left, are magnified in the images at right. e) Pyrite (py), zoned dolomite (Dol) and organic matter with the presence of clay minerals suggested by detectable Al, Si and K in the X-ray spectrum from spot 1. f) Finely laminated clay minerals (corroborated by X-ray spectrum from spot 2) mixed with organic matter. g) Organic matter with clay (yellow arrows) in a clay-rich matrix with zoned dolomite (Dol) and anhedral quartz (Qz).

2.3.3. Iodine species adsorption and chemical transformations

The X-ray radiography data demonstrate that tracer adsorption occurs in the clay- and organic-rich regions of the samples. The adsorption, although significant in terms of the effect on the $\Delta\mu$ profiles, is below the detection limit of the EDS. The question whether or not I^- adsorbs to minerals, soils and sediments has been widely investigated using different methods and varying experimental conditions (e.g. pH, ionic strength and I^- concentration). It has been demonstrated that no adsorption occurs on calcite, quartz, smectite (Na-montmorillonite) and unoxidized pyrite crystals (Aimoz et al., 2011; Kaplan et al., 2000; Rançon, 1988; Ticknor and Cho, 1990). However, I^- adsorption has been detected from low-concentration I^- solutions on Fe(III) oxides formed at oxidized pyrite surfaces (Aimoz et al. 2011), while for illite, the predominant clay mineral in the Cobourg Formation, pH-dependent adsorption is reported from low-concentration I^- solutions (10^{-12} M), with higher adsorption at pH 3.6-5 (K_d= 46 to 59 mL/g) than at pH 7.9 (K_d= 24 mL/g; Kaplan et al., 2000).

When discussing the reactivity of I^- with porous media, it is helpful to consider the behavior of inorganic iodine species in general (I^-, IO_3^- -iodate-, and I_2 -molecular iodine-) and their speciation in response to redox conditions, as well as their pH-dependent adsorption and interaction with organic matter. For example, I^- and IO_3^- have different adsorption properties, with IO_3^- having higher affinity to solid media than I^- at neutral pH (Kodama et al., 2006). I^- adsorbs to the surface of ferric and aluminum oxyhydroxides at pH < 5 (Whitehead 1974); while IO_3^- adsorbs to these oxyhydroxides at pH 6-8 (Couture and Seitz, 1983). Hu et al. (2005) report stronger IO_3^- adsorption compared to I^- on coastal plain sediments at a pH ~ 5 and point to clay-mediated reduction of IO_3^- to I^-, drawing attention to the redox capacity of the medium and transformation of iodine species. In soils and wastewater rich in organic matter, I^- adsorption and oxidation to other iodine species have been documented as well (Rädlinger and Heumann, 2000; Yamaguchi et al., 2010). I^- and IO_3^- sorb

more readily in organic carbon-rich soils than in those with low C content (Kaplan, 2003; Oscarson, 1994; Sheppard and Thibault, 1992). The mechanism for I^- and IO_3^- retention involves their conversion to organo-iodine via I_2, with I^- oxidation only happening in the presence of bacteria (Christiansen and Carlsen, 1991; Seki et al., 2013; Shimamoto et al., 2011; Tsunogai and Sase, 1969). Spectroscopy and spectrophotometry coupled with other analytical techniques confirm I^- is unreactive with organic matter, but in oxidized form as I_2, binding with humic substances (HS) occurs by covalent bonding (Mercier et al., 2000; Reiller et al., 2006; Schlegel et al., 2006). In soils, the oxidation of I^- to I_2 is fast (1 day) but the reaction between I_2 and HS to create organo-iodine compounds is slower (60 days; Yamaguchi et al., 2010). In the samples used in this investigation, it is unlikely that biologically-induced I^- oxidation took place, the high salinity of the synthetic pore water would have suppressed any microbial activity. The hostile environment for microorganisms in the porewater is confirmed by Stroes-Gascoyne and Hamon (2008), who demonstrated that no indigenous bacteria are present in the argillaceous limestone. Furthermore, X-ray radiography data show tracer adsorption occurred after a short contact time with sample DGR4-671.24-a (3 days), attesting to a relatively fast reaction between the tracer solution and the clay- and organic-rich areas.

I^- redox transformations can also occur by photo-chemical reactions. I^- solutions are unstable and oxidize when exposed to UV radiation (Jortner et al., 1961; Miyake and Tsunogai, 1963), a process that occurs even in deaerated solutions (Rigg and Weiss, 1961). The photo-chemical deterioration is accelerated in the presence of oxygen and with increasing I^- concentration (Rigg and Weiss, 1952; Truesdale, 2007). It leads to the formation of I_2, a highly reactive volatile iodine species and tri-iodide (I_3^-); the latter appearing only in high I^- concentration solutions (Kalmár et al., 2014), increasing the solubility of molecular iodine (Bent, 1968). I_2 formation and volatilization can be inhibited by adding thiosulphate ($S_2O_3^{2-}$), a reductant that rapidly reduces I_2 to $2I^-$ (Rançon, 1988).

2.3.4. Humic substances in argillaceous rocks

Humic substances (HS) are the most abundant form of organic carbon on Earth (Hedges et al., 2000). They are ubiquitous in terrestrial and aquatic environments and occur in soil, water and sediments (Schnitzer, 1978). In marine sediments, they are primarily found in continental margins mainly close to the equator and in temperate latitudes, but they do occur in remote basins, away from continental land masses where they concentrate in fine-grained deposits (Premuzic et al., 1982; Waksman, 1933). In marine sediments, $\delta^{13}C$ isotope analysis (-19 to -23 ‰) indicates that the HS are formed *in situ* by the decomposition of marine plankton, without apparent influence from terrigenous HS, even in samples collected close to shore (Nissenbaum and Kaplan, 1972). HS are dark-coloured, complex mixtures of macromolecules of high molecular weight and a randomly coiled structure of non-repeating units (Sposito, 2008). Their structure reveals their complicated genesis. They originate from organic compounds of well-characterized compositions and chemical structures that decompose quickly when incorporated into soils and sediments. A small fraction associates with clays and clay-sized minerals and survives microbial attack, perhaps because of their complex structure or toxicity to microorganisms (Hedges et al., 2000; Theng, 2012). These altered forms of organic matter mix with other products of biological degradation and together are identified as HS (Theng, 2012). Although their structure makes them resistant to further decay, it is their interaction with clay minerals that gives them stability and makes them highly refractory (Baldock and Skjemstad, 2000; Oades, 1988). They decompose at around 400-625°C or 500-650°C, depending on the type of HS (Schnitzer and Hoffman, 1965), thus they can endure diagenetic processes which occur below 200-250°C (Boggs, 2009).

Complexes of clay and HS are among the most important reactions in nature and the most poorly understood (Theng, 2012). The lack of understanding is related to the fact that their interaction is influenced by the structure and chemical properties of both the HS and clay minerals,

as well as the chemistry of the medium (e.g. pH, ionic strength; Satterberg et al., 2003). In most of the adsorption interactions, it is known that clay minerals act as the substrate to which HS are adsorbed (Yariv, 2002). In the depositional environment of the shaly zones of the Cobourg Formation, HS would behave as polyanions that are unable to adsorb on the negatively-charged clay minerals. However, in seawater, multivalent cations (Ca^{2+}, Mg^{2+}, Al^{3+}, Fe^{2+}) act as a bridge and bind them together to form organo-mineral complexes. Investigations in cation-bridging complexation indicate that cementing cations like Ca^{2+} in particular, enhance the adsorption of HS to clays (Baldock and Skjemstad, 2000; Feng et al., 2005; Majzik and Tombácz, 2007). Van der Waals forces are also identified as an important mechanism of adsorption of HS to clay minerals in marine environments (Arnarson and Keil, 2000; Preston and Riley, 1982; Rashid et al., 1972).

The presence of HS in consolidated rocks has been corroborated by Claret et al. (2005). They characterized the nature of the HS in Jurassic clay formations and determined that humic and fulvic acids of marine origin were preserved since deposition.

2.3.5. HS and iodine species retention

Humic and fulvic acids are among the components of HS determining the fate of iodine species in sediments (Hansen et al., 2011). Humic acids adsorb I_2 at pH 5-5.5 (Hansen et al., 2011), whereas fulvic acids have a faster reaction with $I_{2(aq)}$ (Warner et al., 2000) at pH >6. It has been demonstrated that I_2/I_3^- are covalently bonded to carbon of more than one type of HS (Mercier et al., 2000; Reiller et al., 2006; Schlegel et al., 2006), and that the amount of iodine partitioning to HS depends on the number of phenolic groups available (Schlegel et al. 2006).

Considering the X-ray radiography results and the high concentration of the I^- tracer used in our experiments, it is possible that photo-oxidation occurred and the I^- redox state was not preserved despite adding $Na_2S_2O_3$. In that case, the tracer solution would have contained I_2/I_3^-, which reacted

readily with humic and fulvic acids associated with the clay fraction in the samples. The variations in tracer accumulation detected by X-ray attenuation within and between samples could reflect variability in the HS content of the rock

The I_2-HS covalent bonding could be responsible for the irreversibility of the tracer uptake observed in some diffusion experiments carried out in clay-rich formations (e.g. Descostes et al., 2008; Frasca et al., 2012; Savoye et al., 2006; Wittebroodt et al., 2008). On the other hand, halogen bonding is a mechanism that could account for the increased amount of tracer adsorption with contact time reported by some authors (e.g. Bazer-Bachi et al., 2006) and observed in this study. Covalent-bonded iodine atoms can interact with both electron acceptors and electron donors (Politzer et al., 2010) thanks to the anisotropic distribution of its electron cloud (Terraneo et al., 2015). The formation of a region of positive electrostatic potential named the σ-hole (Clark et al., 2007) serves to attract electron donors, such as I_3^-, which forms a halogen bond with I_2. Because this is an electrostatic interaction, it may explain the variable and/or partial iodine desorption observed in some transport experiments (e.g. Descostes, 2008).

2.4. Conclusions and future work

This study demonstrates the X-ray radiography is a promising method to monitor/measure diffusion in intact samples. It provides a good understanding of the structural changes in the porous media along the diffusion path that cannot be accounted for in using conventional methods. The technique drew attention to the fact that I^- tracer solutions can undergo photo-chemical oxidation, which may corrupt diffusion experiments if not taken into account. The photoreaction forms molecular iodine (I_2), a highly reactive iodine species with strong affinity for HS, and triiodide (I_3).

The X-ray data revealed tracer adsorption occurred mainly on dark argillaceous layers in the rocks characterized by clay minerals and organic matter. It is suggested that the tracer solution used

in the experiments contained I_2/I_3^- and reacted with HS preserved in the clay- and organic-rich areas of the Cobourg Formation samples. The precise amount of tracer adsorbed cannot be determined, but from the data it can be inferred that DGR4-671.21-a retained more tracer than DGR3-675.46-c. The discrepancy may be explained by different content of HS in the argillaceous zones, with DGR4-671.24-a showing larger variations along the sample length than DGR3-675.46-c. The type and distribution of HS in the argillaceous areas may have also controlled the amount of tracer adsorption. The covalent nature of the I_2 and HS bond could explain the irreversibility observed in diffusion experiments by other authors.

Under the anoxic conditions prevailing in a DGR, $^{129}I^-$ could be transported away unretarded from the facility presuming its reduced redox state is preserved. Further studies conducted with X-ray radiography, simulating in situ DGR conditions and using unoxidized I^- tracer solutions could provide a comprehensive picture of iodide behaviour in deep argillaceous rocks.

2.5. References

Aimoz, L., Curti, M., Mäder, U., 2011. Iodide interaction with natural pyrite. J. Radioanal. Nucl. Chem. 288, 517–524. https://doi.org/10.1007/s10967-010-0959-9

Akça, B., Erzeneoğlu, S.Z., 2014. The mass attenuation coefficients, electronic, atomic, and molecular cross sections, effective atomic numbers, and electron densities for compounds of some biomedically important elements at 59.5 keV. Sci. Technol. Nucl. Install. 2014, 1–8. https://doi.org/10.1155/2014/901465

Al, T.A., Clark, I.D., Kennell, L., Jensen, M., Raven, K.G., 2015. Geochemical evolution and residence time of porewater in low-permeability rocks of the Michigan Basin, Southwest Ontario. Chem. Geol. 404, 1–17.

Al, T.A., Xiang, Y., Cavé, L., 2010a. Measurement of diffusion properties by X-ray radiography and by through-diffusion techniques using iodide and tritium tracers: core samples from OS-1 and DGR-2 (Technical Report No. TR-07-17, Revision 3). Intera Engineering Ltd., University of New Brunswick.

Al, T.A., Xiang, Y., Loomer, D.B., Cavé, L., 2010b. Measurement of Diffusion Properties by X-Ray Radiography and by Through- Diffusion Techniques Using Iodide and Tritium Tracers: Core Samples from DGR-3 and DGR-4 (Technical Report No. TR-08-27, Revision 0B). Intera Engineering Ltd., University of New Brunswick.

Altman, S.J., Uchida, M., Tidwell, V.C., Boney, C.M., Chambers, B.P., 2004. Use of X-ray absorption imaging to examine heterogeneous diffusion in fractured crystalline rocks. J. Contam. Hydrol. 69, 1–26. https://doi.org/10.1016/S0169-7722(03)00153-0

Altmann, S., 2008. 'Geo'chemical research: A key building block for nuclear waste disposal safety cases. J. Contam. Hydrol. 102, 174–179. https://doi.org/10.1016/j.jconhyd.2008.09.012
ANDRA, 2005. Dossier 2005 Argile: Safety evaluation of a geological repository (Safety Report).
Appelo, C.A.J., Van Loon, L.R., Wersin, P., 2010. Multicomponent diffusion of a suite of tracers (HTO, Cl, Br, I, Na, Sr, Cs) in a single sample of Opalinus Clay. Geochim. Cosmochim. Acta 74, 1201–1219. https://doi.org/10.1016/j.gca.2009.11.013
Appelo, C.A.J., Wersin, P., 2007. Multicomponent Diffusion Modeling in Clay Systems with Application to the Diffusion of Tritium, Iodide, and Sodium in Opalinus Clay. Environ. Sci. Technol. 41, 5002–5007. https://doi.org/10.1021/es0629256
Arnarson, T.S., Keil, R.G., 2000. Mechanisms of pore water organic matter adsorption to montmorillonite. Mar. Chem. 71, 309–320. https://doi.org/10.1016/S0304-4203(00)00059-1
Baldock, J.A., Skjemstad, J.O., 2000. Role of the soil matrix and minerals in protecting natural organic materials against biological attack. Org. Geochem. 31, 697–710. https://doi.org/10.1016/S0146-6380(00)00049-8
Bazer-Bachi, F., Tevissen, E., Descostes, M., Grenut, B., Meier, P., Simonnot, M.-O., Sardin, M., 2006. Characterization of iodide retention on Callovo-Oxfordian argillites and its influence on iodide migration. Phys. Chem. Earth Parts ABC 31, 517–522. https://doi.org/10.1016/j.pce.2006.04.015
Beauheim, R.L., Roberts, R.M., Avis, J.D., 2014. Hydraulic testing of low-permeability Silurian and Ordovician strata, Michigan Basin, southwestern Ontario. J. Hydrol. 509, 163–178. https://doi.org/10.1016/j.jhydrol.2013.11.033
Bent, H.A., 1968. Structural chemistry of donor-acceptor interactions. Chem. Rev. 68, 587–648. https://doi.org/10.1021/cr60255a003
Boespflug, X., Ross, N., Long, B., Dumais, J.F., 1994. Tomodensitométrie axiale: relation entre l'intensité tomographique et la densité de la matière. Can. J. Earth Sci. 31, 426–434. https://doi.org/10.1139/e94-039
Bolt, G.H., de Haan, F.A.M., 1979. Chapter 7: Anion Exclusion in Soil, in: Developments in Soil Science. Elsevier, pp. 233–257. https://doi.org/10.1016/S0166-2481(08)70662-7
Boving, T.B., Grathwohl, P., 2001. Tracer diffusion coefficients in sedimentary rocks: correlation to porosity and hydraulic conductivity. J. Contam. Hydrol. 53, 85–100. https://doi.org/10.1016/S0169-7722(01)00138-3
Brookfield, M.E., Brett, C.E., 1988. Paleoenvironments of the mid-Ordovician (Upper Caradocian) Trenton limestones of southern Ontario, Canada: Storm sedimentation on a shoal-basin shelf model. Sediment. Geol. 57, 75–105. https://doi.org/10.1016/0037-0738(88)90019-X
Cavé, L., Al, T., Xiang, Y., Vilks, P., 2009. A technique for estimating one-dimensional diffusion coefficients in low-permeability sedimentary rock using X-ray radiography: Comparison with through-diffusion measurements. J. Contam. Hydrol. 103, 1–12. https://doi.org/10.1016/j.jconhyd.2008.08.001
Chen, Z., Montavon, G., Ribet, S., Guo, Z., Robinet, J.C., David, K., Tournassat, C., Grambow, B., Landesman, C., 2014. Key factors to understand in-situ behavior of Cs in Callovo–Oxfordian clay-rock (France). Chem. Geol. 387, 47–58. https://doi.org/10.1016/j.chemgeo.2014.08.008
Christiansen, J.V., Carlsen, L., 1991. Enzymatically controlled iodination reactions in the terrestrial Environment. Radiochim. Acta 52–53, 327–333. https://doi.org/10.1524/ract.1991.5253.2.327
Claret, F., Schäfer, T., Rabung, T., Wolf, M., Bauer, A., Buckau, G., 2005. Differences in properties and Cm(III) complexation behavior of isolated humic and fulvic acid derived from Opalinus clay and Callovo-Oxfordian argillite. Appl. Geochem. 20, 1158–1168. https://doi.org/10.1016/j.apgeochem.2005.01.008

Claret, F., Lerouge, C., Laurioux, T., Bizi, M., Conte, T., Ghestem, Jp., Wille, G., Sato, T., Gaucher, E.C., Giffaut, E., Tournassat, C., 2010. Natural iodine in a clay formation: Implications for iodine fate in geological disposals. Geochim. Cosmochim. Acta 74, 16–29. https://doi.org/10.1016/j.gca.2009.09.030

Clark, I.D., Al, T., Jensen, M., Kennell, L., Mazurek, M., Mohapatra, R., Raven, K.G., 2013. Paleozoic-aged brine and authigenic helium preserved in an Ordovician shale aquiclude. Geology 41, 951–954. https://doi.org/10.1130/G34372.1

Clark, T., Hennemann, M., Murray, J.S., Politzer, P., 2007. Halogen bonding: the σ-hole. Proceedings of "Modeling interactions in biomolecules II", Prague, September 5th–9th, 2005. J. Mol. Model. 13, 291–296. https://doi.org/10.1007/s00894-006-0130-2

Couture, R.A., Seitz, M.G., 1983. Sorption of anions of iodine by iron oxides and kaolinite. Nucl. Chem. Waste Manag. 4, 301–306. https://doi.org/10.1016/0191-815X(83)90055-4

Davis, S.N., Thompson, G.M., Bentley, H.W., Stiles, G., 1980. Ground-Water tracers - A short Review. Groundwater 18, 14–23.

Descostes, M., Blin, V., Bazer-Bachi, F., Meier, P., Grenut, B., Radwan, J., Schlegel, M.L., Buschaert, S., Coelho, D., Tevissen, E., 2008. Diffusion of anionic species in Callovo-Oxfordian argillites and Oxfordian limestones (Meuse/Haute–Marne, France). Appl. Geochem. 23, 655–677. https://doi.org/10.1016/j.apgeochem.2007.11.003

Dohrmann, R., Kaufhold, S., Lundqvist, B., 2013. The Role of Clays for Safe Storage of Nuclear Waste, in: Developments in Clay Science. Elsevier, pp. 677–710. https://doi.org/10.1016/B978-0-08-098259-5.00024-X

Feng, X., Simpson, A.J., Simpson, M.J., 2005. Chemical and mineralogical controls on humic acid sorption to clay mineral surfaces. Org. Geochem. 36, 1553–1566. https://doi.org/10.1016/j.orggeochem.2005.06.008

Frasca, B., Savoye, S., Wittebroodt, C., Leupin, O.X., Descostes, M., Grenut, B., Etep-Batanken, J., Michelot, J.-L., 2012. Influence of redox conditions on iodide migration through a deep clay formation (Toarcian argillaceous rock, Tournemire, France). Appl. Geochem. 27, 2453–2462. https://doi.org/10.1016/j.apgeochem.2012.09.003

García-Gutiérrez, M., Cormenzana, J.L., Missana, T., Mingarro, M., 2004. Diffusion coefficients and accessible porosity for HTO and 36-Cl in compacted FEBEX bentonite. Appl. Clay Sci. 26, 65–73.

Gimmi, T., Leupin, O.X., Eikenberg, J., Glaus, M.A., Van Loon, L.R., Waber, H.N., Wersin, P., Wang, H.A.O., Grolimund, D., Borca, C.N., Dewonck, S., Wittebroodt, C., 2014. Anisotropic diffusion at the field scale in a 4-year multi-tracer diffusion and retention experiment – I: Insights from the experimental data. Geochim. Cosmochim. Acta 125, 373–393. https://doi.org/10.1016/j.gca.2013.10.014

Glaus, M.A., Müller, W., Van Loon, L.R., 2008. Diffusion of iodide and iodate through Opalinus Clay: Monitoring of the redox state using an anion chromatographic technique. Appl. Geochem. 23, 3612–3619. https://doi.org/10.1016/j.apgeochem.2008.08.013

Hansen, V., Roos, P., Aldahan, A., Hou, X., Possnert, G., 2011. Partition of iodine (129I and 127I) isotopes in soils and marine sediments. J. Environ. Radioact. 102, 1096–1104. https://doi.org/10.1016/j.jenvrad.2011.07.005

Hedges, J.I., Eglinton, G., Hatcher, P.G., Kirchman, D.L., Arnosti, C., Derenne, S., Evershed, R.P., Kögel-Knabner, I., de Leeuw, J.W., Littke, R., Michaelis, W., Rullkötter, J., 2000. The molecularly-uncharacterized component of nonliving organic matter in natural environments. Org. Geochem. 31, 945–958. https://doi.org/10.1016/S0146-6380(00)00096-6

Hu, Q., Zhao, P., Moran, J.E., Seaman, J.C., 2005. Sorption and transport of iodine species in sediments from the Savannah River and Hanford Sites. J. Contam. Hydrol. 78, 185–205. https://doi.org/10.1016/j.jconhyd.2005.05.007

Jortner, J., Levine, R., Ottolenghi, M., Stein, G., 1961. The photochemistry of the iodide ion in aqueous solution. J. Phys. Chem. 65, 1232–1238. https://doi.org/10.1021/j100825a033
Kalmár, J., Dóka, É., Lente, G., Fábián, I., 2014. Aqueous photochemical reactions of chloride, bromide, and iodide ions in a diode-array spectrophotometer. Autoinhibition in the photolysis of iodide ions. Dalton Trans. 43, 4862–4870. https://doi.org/10.1039/c3dt53255k
Kaplan, D.I., Serne, R.J., Parker, K.E., Kutnyakov, I.V., 2000. Iodide Sorption to Subsurface Sediments and Illitic Minerals. Environ. Sci. Technol. 34, 399–405. https://doi.org/10.1021/es990220g
Kodama, S., Takahashi, Y., Okumura, K., Uruga, T., 2006. Speciation of iodine in solid environmental samples by iodine K-edge XANES: application to soils and ferromanganese oxides. Sci. Total Environ. 363, 275–284. https://doi.org/10.1016/j.scitotenv.2006.01.004
Koroleva, M., de Haller, A., Mäder, U., Waber, H.N., Mazurek, M., 2009. Borehole DGR-2: pore-water investigations (No. TR 08-02), DGR Site Characterization Document. Intera Engineering Ltd., Institute of Geological Sciences University of Bern, Switzerland.
Kumar, T.K., Venkataratnam, S., Reddy, K.V., 1996. Effective atomic number studies in clay minerals for total photon interaction in the energy region 10keV-10MeV. Radiat. Phys. Chem. 48, 707–710.
Loomer, D.B., Scott, L., Al, T.A., Mayer, K.U., Bea, S., 2013. Diffusion–reaction studies in low permeability shale using X-ray radiography with cesium. Appl. Geochem. 39, 49–58. https://doi.org/10.1016/j.apgeochem.2013.09.019
Majzik, A., Tombácz, E., 2007. Interaction between humic acid and montmorillonite in the presence of calcium ions I. Interfacial and aqueous phase equilibria: Adsorption and complexation. Org. Geochem. 38, 1319–1329. https://doi.org/10.1016/j.orggeochem.2007.04.003
Manohara, S.R., Hanagodimath, S.M., Thind, K.S., Gerward, L., 2008. On the effective atomic number and electron density: A comprehensive set of formulas for all types of materials and energies above 1keV. Nucl. Instrum. Methods Phys. Res. Sect. B Beam Interact. Mater. At. 266, 3906–3912. https://doi.org/10.1016/j.nimb.2008.06.034
Mazurek, M., Alt-Epping, P., Bath, A., Gimmi, T., Waber, H.N., 2009. Natural tracer profiles across argillaceous formations: the CLAYTRAC project, Radioactive Waste Managment. OECD, Paris.
Mercier, F., Moulin, V., Guittet, M.J., Barré, N., Toulhoat, N., Gautier-Soyer, M., Toulhoat, P., 2000. Applications of NAA, PIXE and XPS for the quantification and characterization of the humic substances/iodine association. Radiochim. Acta 88. https://doi.org/10.1524/ract.2000.88.9-11.779
Miyake, Y., Tsunogai, S., 1963. Evaporation of iodine from the ocean. J. Geophys. Res. 68, 3989–3993.
Montavon, G., Sabatié-Gogova, A., Ribet, S., Bailly, C., Bessaguet, N., Durce, D., Giffaut, E., Landesman, C., Grambow, B., 2014. Retention of iodide by the Callovo-Oxfordian formation: An experimental study. Appl. Clay Sci. 87, 142–149. https://doi.org/10.1016/j.clay.2013.10.023
Neretnieks, I., 1980. Diffusion in the rock matrix: An important factor in radionuclide retardation? J. Geophys. Res. Solid Earth. https://doi.org/10.1029/JB085iB08p04379
Nissenbaum, A., Kaplan, I.R., 1972. Chemical and isotopic evidence for the in-situ origin of marine humic substances. Limnol. Oceanogr. 17, 570–582. https://doi.org/10.4319/lo.1972.17.4.0570
Nunn, J.A., Xiang, X., Al, T.A., 2018. Investigation of partial water saturation effects on diffusion in shale. Appl. Geochem. 93–101. https://doi.org/10.1016/j.apgeochem.2018.08.004

NWMO, 2011. Geosynthesis (No. NWMO DGR-TR-2011-11). Nuclear Waste Managment Organization.
Oades, J.M., 1988. The retention of organic matter in soils. Biogeochemistry 5, 35–70. https://doi.org/10.1007/BF02180317
Obermajer, M., Fowler, M.G., Snowdon, L.R., 1999. Depositional Environment and Oil Generation in Ordovician Source Rocks from Southwestern Ontario, Canada: Organic Geochemical and Petrological Approach. AAPG Bull. 83. https://doi.org/10.1306/E4FD41D9-1732-11D7-8645000102C1865D
OECD/NEA, 2008. Nuclear Energy Outlook 2008, OECD Publishing. ed. Paris.
Politzer, P., Murray, J.S., Clark, T., 2010. Halogen bonding: an electrostatically-driven highly directional noncovalent interaction. Phys. Chem. Chem. Phys. 12, 7748. https://doi.org/10.1039/c004189k
Premuzic, E., Benkovitz, C.M., Gaeffeny, S., Walsh, J.J., 1982. The nature and distribution of organic matter in the surface sediments of world oceans and seas. Org. Geochem. 4, 63–77. https://doi.org/10.1016/0146-6380(82)90009-2
Preston, M.R., Riley, J.P., 1982. The interactions of humic compounds with electrolytes and three clay minerals under simulated estuarine conditions. Estuar. Coast. Shelf Sci. 14, 567–576. https://doi.org/10.1016/S0302-3524(82)80078-9
Rädlinger, G., Heumann, K.G., 2000. Transformation of Iodide in Natural and Wastewater Systems by Fixation on Humic Substances. Environ. Sci. Technol. 34, 3932–3936. https://doi.org/10.1021/es000868p
Rançon, D., 1988. Comparative Study of Radioactive Iodine Behavior in Soils under Various Experimental and Natural Conditions. Radiochim. Acta 44–45. https://doi.org/10.1524/ract.1988.4445.1.187
Rashid, M.A., Buckley, D.E., Robertson, K.R., 1972. Interactions of a marine humic acid with clay minerals and a natural sediment. Geoderma 8, 11–27. https://doi.org/10.1016/0016-7061(72)90029-8
Reiller, P., Mercier-Bion, F., Gimenez, N., Barré, N., Miserque, F., 2006. Iodination of humic acid samples from different origins. Radiochim. Acta 94, 739–745. https://doi.org/10.1524/ract.2006.94.9.739
Rigg, T., Weiss, J., 1961. The photochemistry of Iodide ions in aqueous solution. J. Phys. Chem. 65, 1937–1940.
Roxburgh, I.S., 1987. Geology of High-level Nuclear Waste Disposal - An Introduction. Chapman and Hall, London UK.
Rueden, C.T., Schindelin, J., Hiner, M.C., DeZonia, B.E., Walter, A.E., Arena, E.T., Eliceiri, K.W., 2017. ImageJ2: ImageJ for the next generation of scientific image data. BMC Bioinformatics 18, 529. https://doi.org/10.1186/s12859-017-1934-z
Satterberg, J., Arnarson, T.S., Lessard, E.J., Keil, R.G., 2003. Sorption of organic matter from four phytoplankton species to montmorillonite, chlorite and kaolinite in seawater. Mar. Chem. 81, 11–18. https://doi.org/10.1016/S0304-4203(02)00136-6
Savoye, S., Frasca, B., Grenut, B., Fayette, A., 2012. How mobile is iodide in the Callovo–Oxfordian claystones under experimental conditions close to the in situ ones? J. Contam. Hydrol. 142–143, 82–92. https://doi.org/10.1016/j.jconhyd.2012.10.003
Savoye, S., Michelot, J.-L., Wittebroodt, C., 2006. Evaluation of the reversibility of iodide uptake by argillaceous rocks by the radial diffusion method. Radiochim. Acta 94.
Sawhney, B.L., 1972. Selective sorption and fixation of Cations by clay minerals: a review. Clays Clay Miner. 20, 93–100.

Schlegel, M.L., Reiller, P., Mercier-Bion, F., Barré, N., Moulin, V., 2006. Molecular environment of iodine in naturally iodinated humic substances: Insight from X-ray absorption spectroscopy. Geochim. Cosmochim. Acta 70, 5536–5551. https://doi.org/10.1016/j.gca.2006.08.026
Schnitzer, M., 1978. Chapter 1 Humic Substances: Chemistry and Reactions, in: Developments in Soil Science. Elsevier, pp. 1–64. https://doi.org/10.1016/S0166-2481(08)70016-3
Schnitzer, M., Hoffman, I., 1965. Thermogravimetry of soil humic compounds. Geochim. Cosmochim. Acta 29, 859–870. https://doi.org/10.1016/0016-7037(65)90083-9
Seki, M., Oikawa, J., Taguchi, T., Ohnuki, T., Muramatsu, Y., Sakamoto, K., Amachi, S., 2013. Laccase-Catalyzed Oxidation of Iodide and Formation of Organically Bound Iodine in Soils. Environ. Sci. Technol. 47, 390–397. https://doi.org/10.1021/es303228n
Selvadurai, A.P.S., Najari, M., 2016. Isothermal Permeability of the Argillaceous Cobourg Limestone. Oil Gas Sci. Technol. – Rev. D'IFP Energ. Nouv. 71, 53. https://doi.org/10.2516/ogst/2015039
Shackelford, C.D., Moore, S.M., 2013. Fickian diffusion of radionuclides for engineered containment barriers: Diffusion coefficients, porosities, and complicating issues. Eng. Geol. 152, 133–147.
Shimamoto, Y.S., Takahashi, Y., Terada, Y., 2011. Formation of Organic Iodine Supplied as Iodide in a Soil−Water System in Chiba, Japan. Environ. Sci. Technol. 45, 2086–2092. https://doi.org/10.1021/es1032162
Sposito, G., 2008. The chemistry of soils, 2nd ed. Oxford Univ. Press, Oxford.
Sterling, S., Melaney, M., 2010. Bedrock Formations in DGR-1 to DGR-6 (Technical Report No. TR-09-11), DGR Site Characterization Document. Intera Engineering Ltd.
Stroes-Gascoyne, S., Hamon, C.J., 2008. Preliminary Microbial Analysis of Limestone and Shale Rock Samples (Technical Report No. TR-2008-09). Atomic Energy of Canada Limited, Nuclear Waste Managment Organization.
Terraneo, G., Resnati, G., Metrangolo, P., 2015. Iodine and Halogen Bonding, in: Kaiho, T. (Ed.), Iodine Chemistry and Applications. John Wiley & Sons, Hoboken, New Jersey.
Theng, B.K.G., 2012. Humic Substances, in: Developments in Clay Science. Elsevier, pp. 391–456. https://doi.org/10.1016/B978-0-444-53354-8.00012-8
Ticknor, K.V., Cho, Y.-H., 1990. Interaction of iodide and iodate with granitic fracture-filling minerals. J. Radioanal. Nucl. Chem. Artic. 140, 75–90. https://doi.org/10.1007/BF02037365
Tidwell, V.C., Glass, R.J., 1994. X ray and visible light transmission for laboratory measurement of two-dimensional saturation fields in thin-slab systems. Water Resour. Res. 30, 2873–2882. https://doi.org/10.1029/94WR00953
Tidwell, V.C., Meigs, L.C., Christian-Frear, R., Boney, C.M., 2000. Effects of spatially heterogeneous porosity on matrix diffusion as investigated by X-ray absorption imaging. J. Contam. Hydrol. 42, 285–302. https://doi.org/10.1016/S0169-7722(99)00087-X
Tournassat, C., Gaucher, E.C., Fattahi, M., Grambow, B., 2007. On the mobility and potential retention of iodine in the Callovian–Oxfordian formation. Phys. Chem. Earth Parts ABC 32, 539–551. https://doi.org/10.1016/j.pce.2005.12.004
Tournassat, C., Steefel, C.I., 2015. Ionic Transport in Nano-Porous Clays with Consideration of Electrostatic Effects. Rev. Mineral. Geochem. 80, 287–329. https://doi.org/10.2138/rmg.2015.80.09
Tournassat, C., Vinsot, A., Gaucher, E.C., Altmann, S., 2015. Chemical Conditions in Clay-Rocks, in: Developments in Clay Science. Elsevier, pp. 71–100. https://doi.org/10.1016/B978-0-08-100027-4.00003-6
Truesdale, V.W., 2007. On the feasibility of some photochemical reactions of iodide in seawater. Mar. Chem. 104, 266–281. https://doi.org/10.1016/j.marchem.2006.12.003
Tsunogai, S., Sase, T., 1969. Formation of iodide-iodine in the ocean. Deep Sea Res. Oceanogr. Abstr. 16, 489–496. https://doi.org/10.1016/0011-7471(69)90037-0

Ullman, W.J., Aller, R.C., 1985. The geochemistry of iodine in near-shore carbonate sediments. Geochim. Cosmochim. Acta 49, 967–978. https://doi.org/10.1016/0016-7037(85)90311-4
Van Loon, L.R., Glaus, M.A., Müller, W., 2007. Anion exclusion effects in compacted bentonites: Towards a better understanding of anion diffusion. Appl. Geochem. 22, 2536–2552. https://doi.org/10.1016/j.apgeochem.2007.07.008
Van Loon, L.R., Mibus, J., 2015. A modified version of Archie's law to estimate effective diffusion coefficients of radionuclides in argillaceous rocks and its application in safety analysis studies. Appl. Geochem. 85–94.
Van Loon, L.R., Soler, J.M., Bradbury, M.H., 2003a. Diffusion of HTO, 36Cl- and 125I- in Opalinus Clay samples from Mont Terri - Effect of confining pressure. J. Contam. Hydrol. 73–83.
Van Loon, L.R., Soler, J.M., Jakob, A., Bradbury, M.H., 2003b. Effect of confining pressure on the diffusion of HTO, 36Cl− and 125I− in a layered argillaceous rock (Opalinus Clay): diffusion perpendicular to the fabric. Appl. Geochem. 18, 1653–1662. https://doi.org/10.1016/S0883-2927(03)00047-7
Van Loon, L.R., Soler, J.M., Müller, W., Bradbury, M.H., 2004. Anisotropic Diffusion in Layered Argillaceous Rocks: A Case Study with Opalinus Clay. Environ. Sci. Technol. 38, 5721–5728. https://doi.org/10.1021/es049937g
Vilks, P., Cramer, J.J., Jensen, M., Miller, N.H., Stanchell, F.W., Miller, H, 2003. In situ diffusion experiment in granite: Phase I. J. Contam. Hydrol. 61, 191–202. https://doi.org/10.1016/S0169-7722(02)00135-3
Waksman, S.A., 1933. On the distribution of organic matter in the sea bottom and the chemical nature and origin of marine humus. Soil Sci. 36, 125–147.
Warner, J.A., Casey, W.H., Dahlgren, R.A., 2000. Interaction kinetics of I_2(aq) with substituted phenols and humic substances. Environ. Sci. Technol. 34, 3180–3185. https://doi.org/10.1021/es991228t
Weber, W.J., McGinley, P.M., Katz, L.E., 1991. Sorption phenomena in subsurface systems: Concepts, models and effects on contaminant fate and transport. Water Res. 25, 499–528. https://doi.org/10.1016/0043-1354(91)90125-A
Wenk, H.R., Voltolini, M., Mazurek, M., Van Loon, L.R., Vinsot, A., 2008. Preferred Orientations and Anisotropy in Shales: Callovo-Oxfordian Shale (France) and Opalinus Clay (Switzerland). Clays Clay Miner. 56, 285–306. https://doi.org/10.1346/CCMN.2008.0560301
Whitehead, D.C., 1984. The distribution and transformations of iodine in the environment. Environ. Int. 10, 321–339. https://doi.org/10.1016/0160-4120(84)90139-9
Whitehead, D.C., 1974. The sorption of iodide by soil components. J. Sci. Food Agric. 25, 73–79. https://doi.org/10.1002/jsfa.2740250109
Wittebroodt, C., Savoye, S., Frasca, B., Gouze, P., Michelot, J.-L., 2012. Diffusion of HTO, 36Cl− and 125I− in Upper Toarcian argillite samples from Tournemire: Effects of initial iodide concentration and ionic strength. Appl. Geochem. 27, 1432–1441. https://doi.org/10.1016/j.apgeochem.2011.12.017
Wittebroodt, C., Savoye, S., Gouze, P., 2008. Influence of initial iodide concentration on the iodide uptake by the argillite of Tournemire. Phys. Chem. Earth Parts ABC 33, 943–948. https://doi.org/10.1016/j.pce.2008.05.020
Xiang, Y., Al, T., Scott, L., Loomer, D., 2013. Diffusive anisotropy in low-permeability Ordovician sedimentary rocks from the Michigan Basin in southwest Ontario. J. Contam. Hydrol. 155, 31–45.
Xiang, Y., Loomer, D., Al, T., 2014. Improvements in methodologies for radiographic measurement of diffusion properties in low-permeability rocks, and development of methods for pH measurement in brines (No. NWMO TR-2014). Nuclear Waste Managment Organization, University of New Brunswick.

Yamaguchi, N., Nakano, M., Takamatsu, R., Tanida, H., 2010. Inorganic iodine incorporation into soil organic matter: evidence from iodine K-edge X-ray absorption near-edge structure. J. Environ. Radioact. 101, 451–457. https://doi.org/10.1016/j.jenvrad.2008.06.003

Yariv, S., 2002. Introduction to organo-clay complexes and interactions, in: Yariv, S., Cross, H. (Eds.), Organo-Clay Complexes and Interactions, Organo-Clay Complexes and Interactions. CRC Press, Boca Raton.

Chapter 3

SUMMARY AND CONCLUSIONS

3.1. Concluding remarks

This project aimed at measuring diffusion coefficients in low-porosity rocks (< 2%) using X-ray radiography. The objective was to refine the method developed by Cavé et al. (2009) to detect iodide concentration and quantify diffusion in sedimentary (argillaceous formations) and crystalline (e.g. granite) rocks, which are currently under investigation worldwide as potential host formations for Deep Geological Repositories (DGRs). Using an X-ray-CT instrument, the image parameters were optimized following the work of Nunn (2018), and after careful testing of standards coupled with meticulous registration procedures, the Signal-to-Noise Ratio (SNR) was improved. Samples from the Cobourg Formation (argillaceous limestone) and the Lac du Bonnet Batholith (granite) were used in the diffusion experiments and the results have shed light on I^- behaviour in argillaceous formations and on the limitations of the X-ray method in crystalline rocks. An overview of the key findings of this research is presented below.

3.1.1. Cobourg Formation argillaceous limestone experiments

The X-ray radiography method has been successfully applied to monitor the diffusion of I^- tracer in low-porosity (1.3 ± 0.1 %) samples from the Cobourg Formation, an Ordovician argillaceous limestone formerly under investigation as potential DGR host for low- and intermediate-level nuclear waste in Canada. The data show that accumulation of the tracer occurs by adsorption at specific locations along the diffusion path. The adsorption correlates to clay- and organic-rich domains in the samples. Published data on I^- chemical behaviour indicate that it is unreactive with minerals at the neutral pH of the experiments and that no interaction occurs with organic matter in

the absence of bacteria. However, a consensus exists on I^- adsorption to humic substances (including humic and fulvic acids, collectively referred to here as HS) when I^- is oxidized to I_2, which is attached by covalent bonding. It is known that I^- tracer solutions undergo photo-chemical oxidation producing I_2/I_3^- and that HS can be preserved in deep, clay-rich formations. Based on the X-ray radiography data, it is believed that the I^- tracer solution used in this experiment underwent photo-chemical oxidation and that the I_2/I_3^- reacted with HS contained in the argillaceous regions of the samples.

The findings underlined in this study emphasize the importance of understanding fundamental aspects of iodine speciation that influence its interaction with the solid medium within which it diffuses. These results specifically demonstrate the importance of understanding HS in clay-rich rocks, their distribution and characterization, and how they affect iodine species transport.

The X-ray radiography method gives clear evidence of where tracer accumulation takes place during diffusion experiments, providing new insights into I^- fate and transport in argillaceous rocks; a somewhat controversial topic in research focused on demonstrating the long-term safety of the geological barrier system.

3.1.2. Lac du Bonnet granite experiments

Several challenges were encountered with diffusion experiments carried out with Archean granite samples (porosity 0.4 ± 0.1 %) from the Underground Research Laboratory located on the Lac du Bonnet Batholith. The X-ray radiography data did not provide profiles consistent with I^- diffusion over time. Time-series profiles were slightly displaced relative to the reference profile and the displacement was consistent, in part, with image misalignment. Precise alignment between the reference image and the time series is key for the successful removal of the sample background that allows the effect of the tracer to be visualized. While careful steps were taken to align the sample to

its initial position from image to image, and to register the images down to the pixel level, misalignment of the time-series profile was unavoidable. The results point to several sources of error during the experiments. One of them comes from the level of accuracy in the movement of the instrument stage, which controls the stage on the *x*, *y* and *z* axes; the stage control is not perfect and slight deviations in positioning lead to errors in image alignment. Additionally, the aluminum cap used as an internal standard may have moved a little during sample handling, and it was noted the aluminum is not homogeneous. In order to normalize the X-ray intensities consistently throughout the experiment duration, an identical, homogeneous region on the standard is required for correcting variations from the X-ray source from time to time (image to image).

In summary, imaging-related errors are significant in rocks with porosity below 1%, the alignment and registration must be precise and accurate because image contrast resulting from the presence of the tracer is very small.

3.1.3. Limitations of the method

While the application of the X-ray radiography method in argillaceous samples successfully demonstrate tracer adsorption occurs in clay- and organic rich areas in the samples, the absolute tracer accumulation cannot be quantified. This represents a research opportunity that would complement the application of the method in transport experiments.

The experiments with granitic rocks have demonstrated that tracer signal can be detected but limitations of the X-ray CT system in positioning the stage at micrometric precision needs to be addressed.

3.2. Future work

To continue our understanding of I^- transport in clay-rich formations, and consequently the fate of ^{129}I in the geological media surrounding a DGR, future experiments using X-ray radiography focused on replicating reducing conditions prevailing in a DGR could provide a comprehensive picture of the reactivity of I^- with the solid medium.

For crystalline rocks with porosities below 1 %, perfect alignment of the sample and standard from image to image is critical to the successful application of the technique. Future studies focusing on solving the registration challenges would yield optimal results in measuring diffusion in crystalline rocks.

In future experiments, special care has to be taken in handling the high concentration I^- solutions needed with low-porosity rocks. In order to avoid photo-oxidation, tracer solutions should be stored in a dark container, protected from light to preserve its integrity. Thiosulphate ($Na_2S_2O_3$) should be added at a fixed concentration to avoid the formation of I_2/I_3.

3.3. References

Cavé, L., Al, T., Xiang, Y., Vilks, P., 2009. A technique for estimating one-dimensional diffusion coefficients in low-permeability sedimentary rock using X-ray radiography: Comparison with through-diffusion measurements. J. Contam. Hydrol. 103, 1–12. https://doi.org/10.1016/j.jconhyd.2008.08.001

Nunn, J., 2018. Investigations of partial gas saturation on diffusion in low- permeability sedimentary rocks. University of Ottawa, Ottawa, ON.

Appendix A

DIFFUSION EXPERIMENTS IN GRANITIC ROCKS

A.1. Introduction

Environmental site assessments are currently under way in many countries to evaluate the suitability of crystalline formations as deep geological repositories (DGR). These rocks are widely distributed over the Earth's surface (cover 20%; Hartmann and Moosdorf, 2012) and are relatively stable (McKinley et al., 2007). The interest as a potential DGR's relies on their strength, which provides structural stability, a relatively high melting point and low hydraulic conductivity (10^{-8} to 10^{-6} m/s at 1 km depth; Roxburgh, 1987; Stober and Bucher, 2007). The latter is affected by fault systems and fracture networks commonly present in crystalline bodies, but at the relative local scale of a DGR, it is expected these systems will be avoided (McEwen, 2007), reducing the transport of dissolved radionuclides to molecular diffusion in the pore structure. In crystalline unaltered rocks the porosity is below 1%, and is mainly associated to microfractures and to intergranular pores formed by secondary minerals and fluid inclusions (Schild et al., 2001; Tullborg and Larson, 2006).

Due in part to their low porosity, crystalline rocks represent a challenge for measuring diffusion coefficients using X-ray radiography. In this section, the main difficulties encountered with the method are highlighted.

A.2. Materials and methods

A.2.1. Lac du Bonnet Batholith samples

The samples used in the diffusion experiments were selected from archived drill cores from the Underground Research Laboratory (URL) in southern Manitoba, Canada. The URL is located on

the Lac du Bonnet batholith (Fig. A.1). This locality has been under investigation to characterize the hydrogeological conditions and to understand the processes affecting fluid migration at depth in crystalline rocks to further unravel their influence on a deep geological repository.

The Archean (~ 2600 Ma) Lac du Bonnet batholith is of granite-granodiorite composition, generally pink in colour at shallow depth (< 200 m) and predominantly grey at depths greater than 200 m; it has an elongated shape with an east-northeast trend and a surface exposure of about 1000-1500 km^2 (Brown et al., 1989; Gascoyne, 2004). The intrusive complex is also dominated by sub-vertical fractures at 100-200 m depth, whereas shear faults (about 20° dip) occur sparsely throughout the geological unit and control the groundwater flow in the uppermost 200 m where they interconnect with the sub-vertical system (Stevenson et al., 1996). In these zones the permeability decreases with depth with values ranging from 3 x 10^{-19} m^2 (in the upper 400 m) to 3 x 10^{-22} at the unweathered and unfractured zones about 1000 m depth (Stevenson et al., 1996).

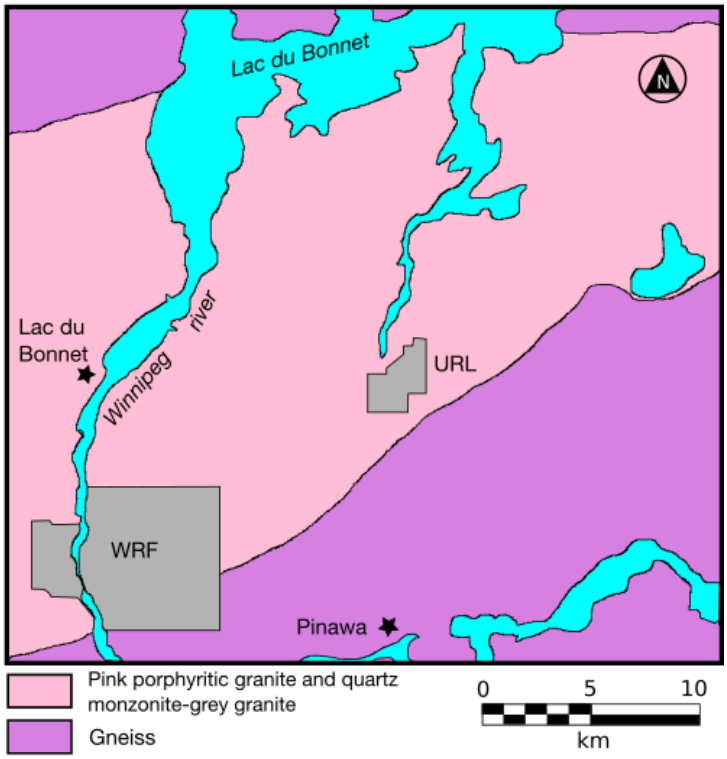

Figure A.1. Geology of the Lac du Bonnet batholith, and the location of the Whiteshell nuclear facility (WRF) and the Underground Research Laboratory (URL; modified from Brown et al., 1998).

The granitic samples used in this study were obtained from a 34 mm diameter core segment at 15 m depth (Fig. A.2; drill core number 275-EXT-IN). The segment displays a fracture surface on one end (top) with no visible evidence of weathering. Five samples ranging from 28.81 to 30.97 mm long were cut from below the fracture using a water-cooled diamond saw. Archived thin sections of the core were examined by optical microscopy.

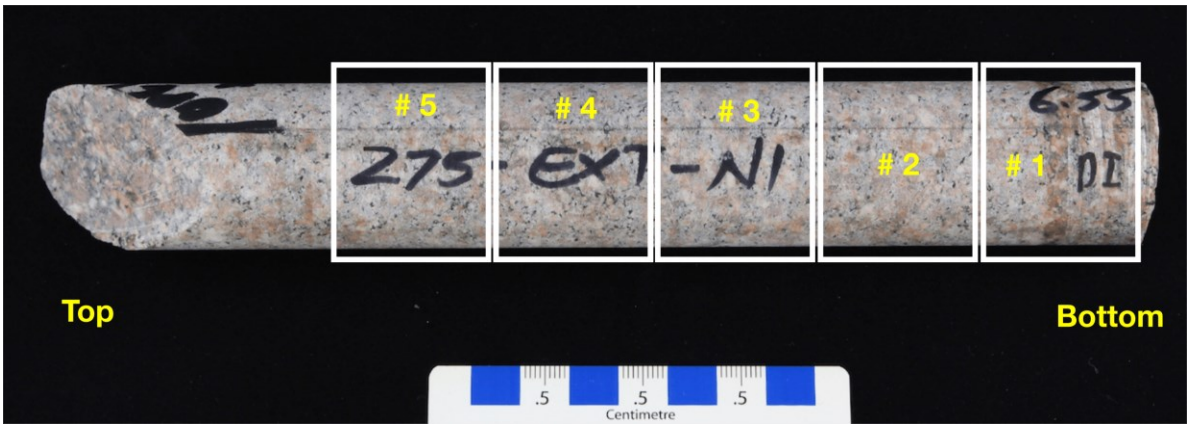

Figure A.2. Photograph of the Lac du Bonnet drill core showing sections were subsamples were obtained.

A.2.2. Experimental procedures

Core #3 was used to measure the water-accessible porosity (φ_w) following the method described by Xiang et al. (2013). A simplified composition of the Standard Canadian Shield brine (Table A.1; McMurry, 2004) was used in the current experiment due to its high salinity, even though the shallow groundwater at the URL is Ca-Na-HCO_3 water of low salinity (TDS < 0.3 g/l; Gascoyne, 2004).

Ions	SPW (mol/kgw)	Tracer (mol/kgw)
Na^+	1.1066	1.1066
K^+	0.0090	0.0090
Ca^{2+}	1.8714	1.8714
Mg^{2+}	0.0597	0.0597
Cl^-	4.9882	3.9882
I^-	-	1.000
Ionic strength	6.9	6.9

Table A.1. Synthetic porewater (SPW) and iodide tracer solution used for the diffusion experiments (simplified from McMurry, 2004).

Cores #1, #2, #4 and # 5 were re-saturated following the method described by Xiang et al., (2014) and were left immersed in SPW for four weeks. After saturation, the sample cells were prepared similarly to the procedure detailed by Loomer et al. (2013), using Delrin® cells and placing aluminum caps (13 mm height, 33 mm diameter) at the top to serve as internal standard. To aid in the image registration, two openings at 180° of each other were drilled in each aluminium (Al) cap and lead balls were inserted and kept in place with silicone (Fig. A.3). SPW was instilled in the sample cell lower reservoir and at the top of the surface through a hole in the Al cap to keep saturation on both ends. The felt disc at the top was kept dampened by injecting SPW daily and closing up the hole with a nylon screw. The diffusion experiments were initiated by replacing the SPW from the lower reservoir with iodide tracer solution.

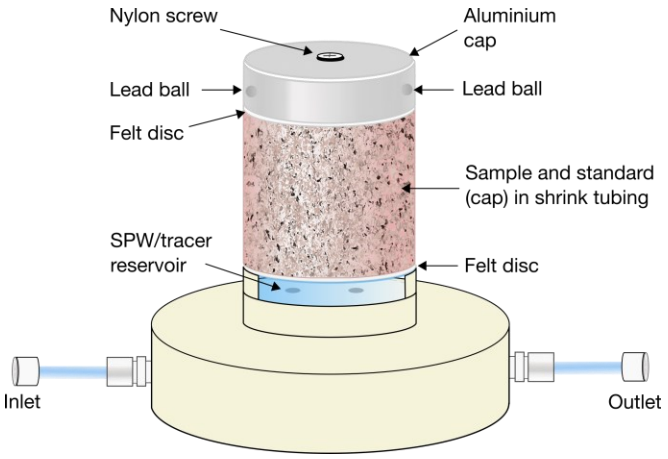

Figure A.3. Diagram of a granite sample mounted in the diffusion Delrin® cell used for X-ray radiography.

X-ray measurements were conducted with an X-ray CT system as described in Chapter 2, collecting reference X-ray images for each sample immediately after injecting the tracer solution. Subsequent images were obtained every 24 hours for four days, and then in times intervals of 40-48 hours; great caution was taken to align them at the same position as to the reference image. The tracer solution in the lower reservoir was replaced every 24 hours and after 88 days the experiments were stopped. The X-ray source voltage and current settings were optimized at 50 kV and 60 mA,

acquisition time was 1 frame per second with 48 frames averaged to produce an image. A 3.3 mm aluminum filter was used to condition the beam and minimize beam hardening. X-ray images were collected as 16-bit DCM files (1024 x 1024 pixels, 65 536 greyscale values -gsv-) and analyzed using ImageJ software (Rueden et al., 2017). Alternatively to the Al cap, a ceramic block (Mykroy/Mycalex; McMaster-Carr) and a region on the middle of the sample were also used as internal standards to correct for variations in the X-ray source.

A.3. Results and Discussion

The petrographic analysis show that some quartz crystals present undulose extinction and fluid inclusions, and biotite has pleochroic halos (Fig. A.4 A). Allomorphic quartz micrograins are commonly observed at the contact between quartz and potassium feldspar, as well as small amphibole and feldspar crystals (Fig. A.4 A and B). Intergranular microcracks are most frequent in quartz and feldespars and although less common, interphase microfractures are also observed between these two minerals (Fig. A.4 B). The cracks are irregular and they seem to appear also at the grain boundaries.

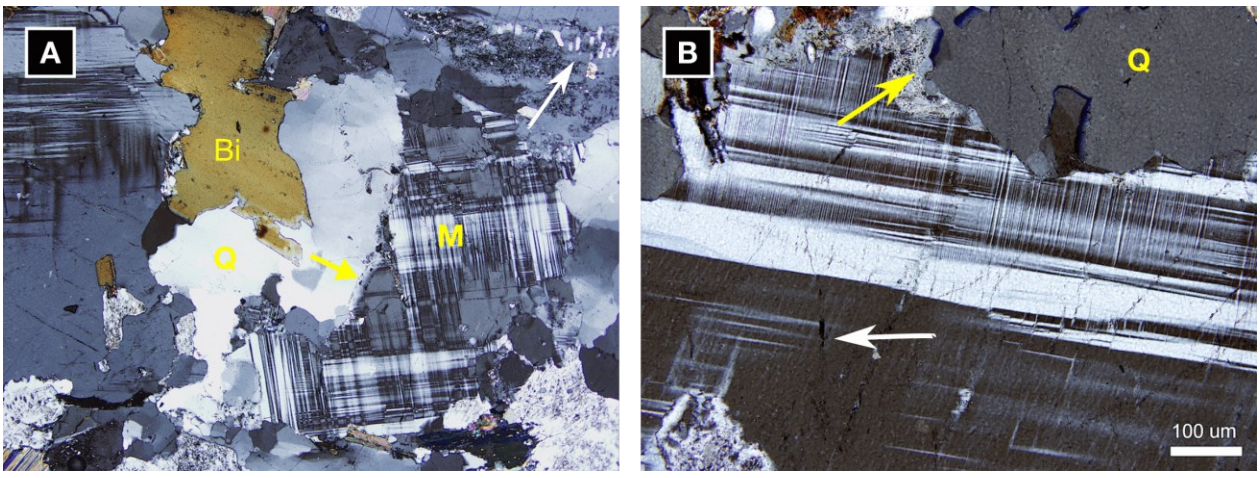

Figure A.4. Microphotographs of core 275-EXT-NI. A: centre occupied by quartz (Q) with undulose extinction and fluid inclusions close to the edge (yellow arrow), biotite (Bi) with pleochroic halos and microcline (M) with cross-hatched twinning. Mirmekite rods (white arrow). B: Microfractures in microcline (white arrow) and common intragranular microquartz (yellow arrow).

The results from water-accessible porosity (φ_w) measurements confirm very low values as expected in crystalline, unfractured rocks. The porosity obtained from triplicate measurements for granite # 3 is 0.4 % ($\pm$ 0.1).

A.3.1. X-ray radiography diffusion profiles

X-ray imaging data of the analyzed samples display fluctuating $\Delta\mu$ values; the time-series profiles do not reveal an attenuation pattern consistent with iodide diffusion over time. For example, time-series plots of granite #2 and #4 show $\Delta\mu$ values higher at 6 days than at 10 days after the diffusion started (Fig. A.5 A and B). In granite #2 the trend is constant throughout the profile, but in #4 the difference between the two time-series becomes smaller along the sample distance and they almost overlap close to the top (from 22 to 27 mm, Fig. A.5 B) as it would be expected with no tracer breakthrough at this time. Generally, granite #4 exhibits a lot of $\Delta\mu$ variations at the bottom of the sample (0 to 14 mm) than at the top, but this variation is not consistent with tracer diffusion and a concentration front cannot unarguably be identified. In contrast, granite #2 $\Delta\mu$ profiles commonly show more attenuating $\Delta\mu$ values at early diffusion times than at later (e.g. more attenuation observed at 4 days than at 33 days, Fig. A.5 A) and the difference in $\Delta\mu$ values remains relatively constant throughout the sample length giving the plot a slightly symmetrical look.

Significant care was put into image processing, and reference images were carefully aligned to their respective time-series images at the pixel level. Similarly, in each image a rigorous registration procedure was done in the aluminum cap fixed on the top of the sample to adjust for variations in the X-ray intensity. However, in an attempt to identify the source of discrepancies among greyscale values and to better understand the anomalous plots, a ceramic block and a region at the centre of the sample were additionally used for image normalization on granite #2 and #4 respectively. The ceramic block is mounted into the screen frame designed to protect the detector from the high

photon flux from the source, it is 30 mm in height with a constant thickness of 25 mm. The block is mainly composed of B_2O_3, SiO_2, Al_2O_3, MgO, SrO, K_2O and other trace elements (McMaster-Carr) that could interact with the x-ray beam similarly to the minerals in the sample. For normalization using the imaged sample, a region was selected in an area away from any potential influence by the diffusing tracer. For granite #2, the results show a $\Delta\mu$ vs distance graph with higher $\Delta\mu$ values relative to those obtained with the aluminum cap, yet the pattern of higher attenuation at early diffusion times still remains (Fig. A.3 C). A distinct feature in both granite #2 plots is the 43 days time-series profile, which shows significant attenuation that does not follow the general symmetrical plot pattern. This error is thought to be due to molecular iodine ($I_{2(g)}$) diffusing through unforeseen openings between the polyolefin plastic sleeve and the sample. Iodide tracer solutions undergo photochemical oxidation, a reaction that produces volatile I_2. Its formation is inferred from yellowish stains observed on the sample cell. In the case of granite #4, using a region on the sample for image normalization minimized considerably $\Delta\mu$ variations (Fig. A.5 D), but the lack of a consistent attenuation trend over time and misalignment of the time-series profiles on the upper-half of the sample (from 12 to 26 mm), clearly reveal a composite of factors are affecting the measurements. From the grayscale vs distance plots of granite #2 and #4 is apparent that errors in $\Delta\mu$ are related, in part to registration, noise and distortion, which are all more significatively notorious when using the aluminum cap standard than with the sample standard (Fig. A.6). The 1-4 days time-series profiles in granite #2 hardly line up with the greyscale values of the reference image after careful registration. Conversely, granite #4 shows better fit of time-series profiles with the reference image for the same diffusion period except at the inflection points (Fig. A.6 B).

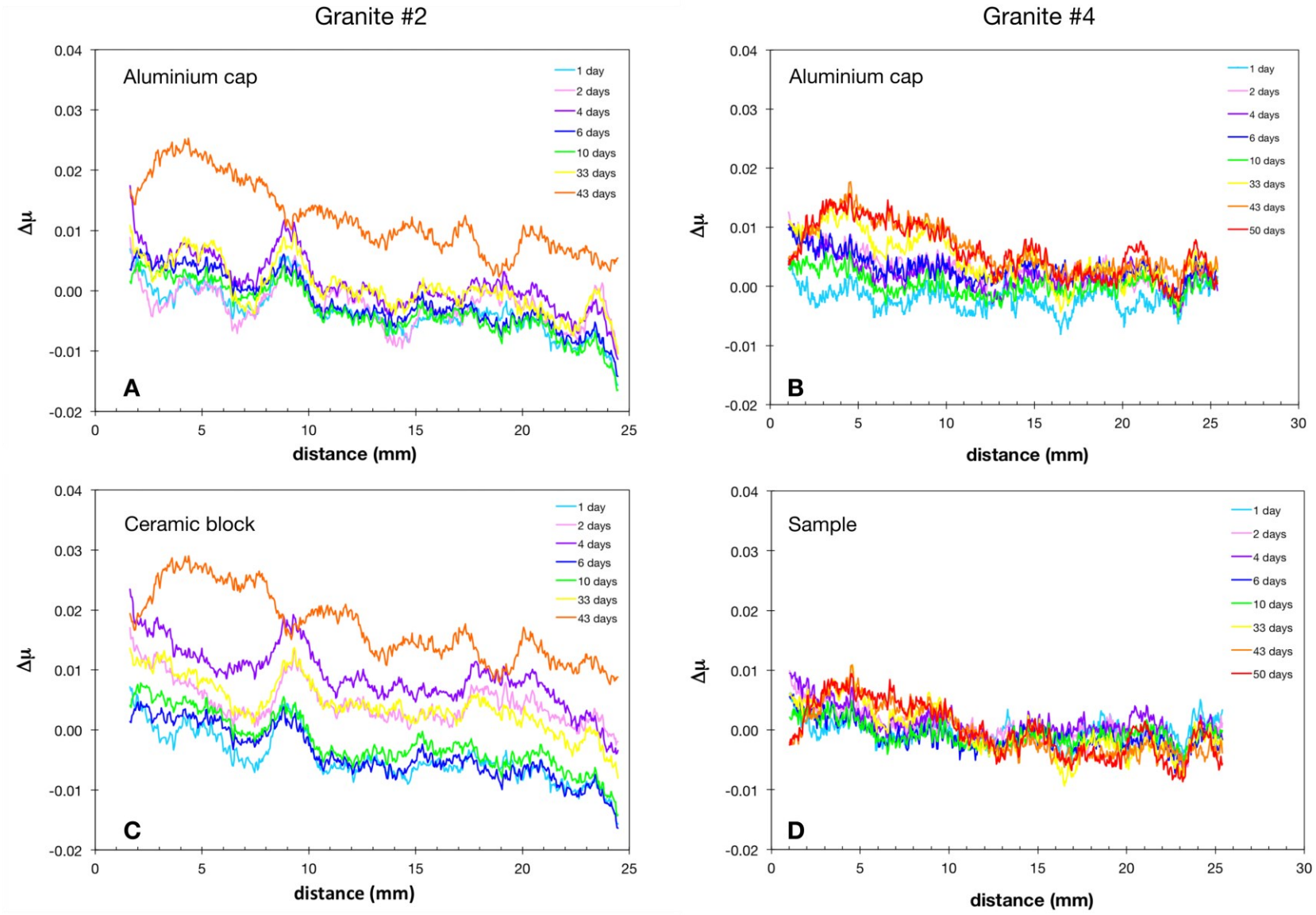

Figure A.5. Δμ versus distance graphs of granite # 2 and #4 obtained using different standards to adjust for variations of X-ray intensities from image to image. A and B: aluminium on top of the sample; C: a ceramic block inserted in the shielding screen, and D: a region on the sample.

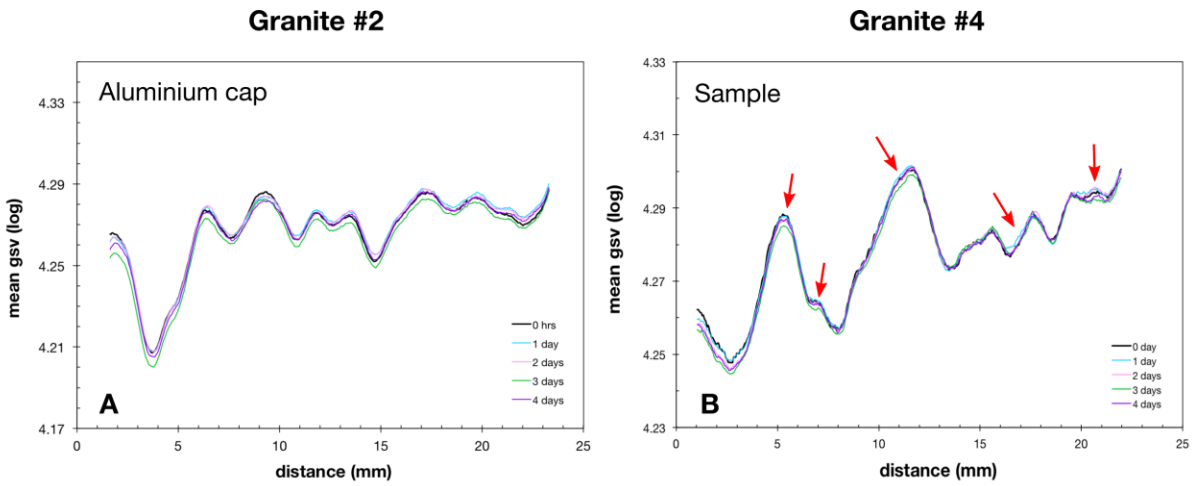

Figure A.6. A: effects of misalignment and inaccurate adjustments of X-rays intensities (Al cap standard) on the granite # 2 greyscale vs distance plot. B: granite #4 profile showing effects of image quality on registration. Greyscale values (gsv) on the plot inflections (red arrows) display uneven signal and noise, more significant close to the top of the sample (from 15-23 mm).

The sample imaged with X-rays is an array of pixels with specific information recorded as greyscale values (in a 16-bit image values range from 0 to 65,536), each one in a unique position similar to the Cartesian system with *x* and *y* coordinates. Because the X-radiography method relies in the blank subtraction approach in order to visualize the change in attenuation caused by the iodide tracer (Cavé et al., 2009), the pixel array of the time-series image must have the same *x* and *y* coordinates as in the reference image, as well as the same vertical to horizontal dimension in pixels for the method to work (Fig. A.7). Furthermore, the sample under study should be accurately placed on the same position between X-ray measurements. Image misalignment contributes significatively to errors in low porosity rocks, in addition to inaccurate adjustment of X-ray intensities from image to image. The change in greyscale values caused by the tracer is very small, thus an imprecise normalization aggravates the registration problem as it was demonstrated with the Al cap and ceramic block used as standards. In this experiment considerable effort was placed to minimize the error introduced by image registration (it is noted that manual registration renders better results than appropriate software); however, results suggest that the quality of the data is also affected by a

number of factors including sample movement and noise. The high-power X-ray CT system (Pinnacle X-ray Systems, Suwanee, Ga., U.S.A) used in this work has the ability to limit noise, but the high X-ray photon flux needed compromises the image resolution, restricting the capacity for discriminating adequately features in the sample. In the case of granite #4 greyscale vs distance plot normalized with a region on the sample, a better alignment among the reference and time-series images was achieved, with the exception of the inflexion points (Fig. A.6 B) where the pixel values either decrease or increase beyond the reference profile values, leading to significant errors on the $\Delta\mu$ plot. The distortion observed on the time-series profiles curvatures could be explained by a combination of image noise and resolution.

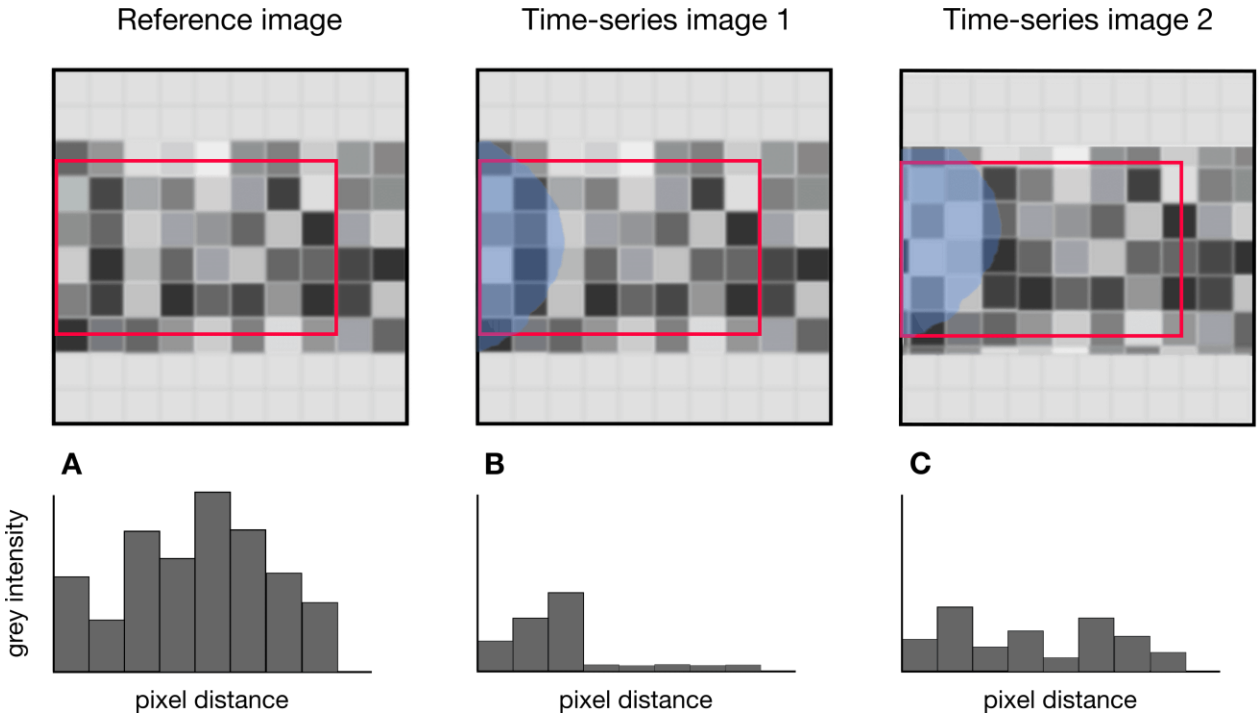

Figure A.7. Representation of the blank subtraction method on a region of interest (red rectangle) for an imaged sample. A: reference image and baseline greyscale values. B: greyscale values reflecting the presence of tracer (blue area) in the sample after the blank subtraction removes efficiently the rock matrix C: anomalous greyscale values due to physical and image misalignment.

Precise alignment was not possible to attain using standards that move independently from the sample. This is more evident with the ceramic standard, which is attached to the shielding screen,

than with the Al cap, which is attached to the sample, but susceptible to minute displacements every time the nylon screw is removed to saturate the felt disc with SPW. Moreover, minor displacements of the sample from the source and detector from image to image could also contribute to the greyscale values fluctuation observed on the time-series profiles.

A.4. Conclusions

The diffusion of iodide in ~30 mm-long granitic samples from Lac du Bonnet batholith was studied using the X-ray radiography method. The results indicate that errors due to millimetric displacement of the sample and detached standard cause miscalculation of the time-series greyscale values. Because the blank subtraction relies in an accurate removal of the background to monitor the tracer diffusion, misalignment of the sample and standard leads to spurious greyscale intensities that cannot produce coherent $\Delta\mu$ values; this is an experimental error that cannot be corrected during image processing. The precision of the measurements is paramount since contrast caused by the tracer is very small and additional artifacts related to the quality of the image represent an additional challenge to the experiment.

The X-ray radiography method can potentially be a useful technique to measure diffusion coefficients in rocks with porosity < 1 %, however critical to the successful application is a perfect alignment between the sample and standard, and precise adjustment of X-ray intensities from image to image. For future work, focusing on solving the registration challenges would yield optimal results in measuring diffusion in crystalline rocks.

A.5. References

Brown, A., Soonawala, N.M., Everitt, R.A., Kamineni, D.C., 1989. Geology and geophysics of the Underground Research Laboratory site, Lac du Bonnet Batholith, Manitoba. Can. J. Earth Sci. 26, 404–425. https://doi.org/10.1139/e89-037

Cavé, L., Al, T., Xiang, Y., Vilks, P., 2009. A technique for estimating one-dimensional diffusion coefficients in low-permeability sedimentary rock using X-ray radiography: Comparison with through-diffusion measurements. J. Contam. Hydrol. 103, 1–12. https://doi.org/10.1016/j.jconhyd.2008.08.001

Davidson, C.C., 1984. Monitoring hydrogeological conditions in fractured rock at the site of Canada's Underground Research Laboratory. Groundw. Monitoting Remediat. 4, 95–102. https://doi.org/10.1111/j.1745-6592.1984.tb00899.x

Gascoyne, M., 2004. Hydrogeochemistry, groundwater ages and sources of salts in a granitic batholith on the Canadian Shield, southeastern Manitoba. Appl. Geochem. 19, 519–560. https://doi.org/10.1016/S0883-2927(03)00155-0

Hartmann, J., Moosdorf, N., 2012. The new global lithological map database GLiM: A representation of rock properties at the Earth surface. Geochem. Geophys. Geosystems 13, 1–37. https://doi.org/10.1029/2012GC004370

McEwen, T., 2007. Site selection and characterisation, in: Radioactivity in the Environment. Elsevier, pp. 77–111. https://doi.org/10.1016/S1569-4860(06)09004-8

McKinley, I.G., Russell Alexander, W., Blaser, P.C., 2007. Development of geological disposal concepts, in: Radioactivity in the Environment. Elsevier, pp. 41–76. https://doi.org/10.1016/S1569-4860(06)09003-6

McMurry, J., 2004. Reference water composition for a Deep Geological Repository in the Canadian Shield (No. 06819-REP-01200-10135-R01), Nuclear Waste Management. Ontario Power Generation.

Roxburgh, I.S., 1987. Geology of High-level Nuclear Waste Disposal - An Introduction. Chapman and Hall, London UK.

Rueden, C.T., Schindelin, J., Hiner, M.C., DeZonia, B.E., Walter, A.E., Arena, E.T., Eliceiri, K.W., 2017. ImageJ2: ImageJ for the next generation of scientific image data. BMC Bioinformatics 18, 529. https://doi.org/10.1186/s12859-017-1934-z

Schild, M., Siegesmund, S., Vollbrecht, A., Mazurek, M., 2001. Characterization of granite matrix porosity and pore-space geometry by *in situ* and laboratory methods. Geophys. J. Int. 146, 111–125. https://doi.org/10.1046/j.0956-540x.2001.01427.x

Stevenson, D.R., Kozak, E.T., Davison, C.C., Gascoyne, M., Broadfoot, R.A., 1996. Hydrogeologic characteristics of domains of sparsely fractured rock in the granitic Lac du Bonnet batholith, southeastern Manitoba, Canada (No. AECL-11558, COG-96-117). Atomic Energy of Canada Limited, Ottawa, ON.

Stober, I., Bucher, K., 2007. Hydraulic properties of the crystalline basement. Hydrogeol. J. 15, 213–224. https://doi.org/10.1007/s10040-006-0094-4

Tullborg, E.-L., Larson, S.Å., 2006. Porosity in crystalline rocks – A matter of scale. Eng. Geol. 84, 75–83. https://doi.org/10.1016/j.enggeo.2005.12.001

Wilson, C.R., Witherspoon, P.A., Long, J.C.S., Galbraith, R.M., DuBois, A.O., McPherson, M.J., 1983. Large-scale Hydraulic Conductivity Measurements in Fractured Granite. Int. J. Rock Mech. Min. Sci. Geomech. Abstr. 26, 279–286.

Xiang, Y., Al, T., Scott, L., Loomer, D., 2013. Diffusive anisotropy in low-permeability Ordovician sedimentary rocks from the Michigan Basin in southwest Ontario. J. Contam. Hydrol. 155, 31–45.

Xiang, Y., Loomer, D., Al, T., 2014. Improvements in methodologies for radiographic measurement of diffusion properties in low-permeability rocks, and development of methods for pH measurement in brines (No. NWMO TR-2014). Nuclear Waste Managment Organization, University of New Brunswick.

Appendix B

X-RAY RADIOGRAPHY, STANDARDS AND REGISTRATION

B.1. Introduction

X-rays are electromagnetic radiation that travels at a constant speed of 3 x 10^5 km/s in vacuum (X-ray tube) and have the ability to penetrate and interact with certain materials in different degree (Selman, 2000). These interactions involve scattering and absorption processes that eliminate some of the X-rays in a process called attenuation (Sprawls, 2019). The attenuation depends on the characteristics of the material (density, thickness, atomic number) and the energy of the X-rays (Sprawls, 2019). Polychromatic X-rays are affected by fluctuations in voltage; thus, it is of interest to understand how these fluctuations sway the attenuation of materials used for normalization of the X-ray intensities in diffusion experiments. The purpose of this section is to describe the tests conducted on different objects and calibrating materials at off-, mid- and on-peak periods of electricity use and at different voltage.

B.2. Background

The X-ray radiography method to measure diffusion in low-porosity rocks is a challenge because the attenuation caused by an attenuating tracer cannot be easily differentiated from the sample background (low signal-to-noise ratio, SNR). However, the technique developed by Cavé et al. (2009) has been refined, and with the high-power of the X-ray-CT instrument from Pinnacle X-ray Systems, the image parameters were optimized following the work of Nunn (2018). Initial X-imaging (greyscale value -gsv- measurements) of the Cobourg formation (1-2 % porosity) rendered a good SNR, nonetheless the $\Delta\mu$ profiles did not show a coherent evolution of the tracer concentration because of the difficulty to align the time-series profiles with the reference (Fig. B.1).

The plots display profiles consistent with apparently an image registration issue, however, after careful analysis of the procedure, it seemed that a combination of random errors associated with calibrating materials and systematic errors were affecting the data.

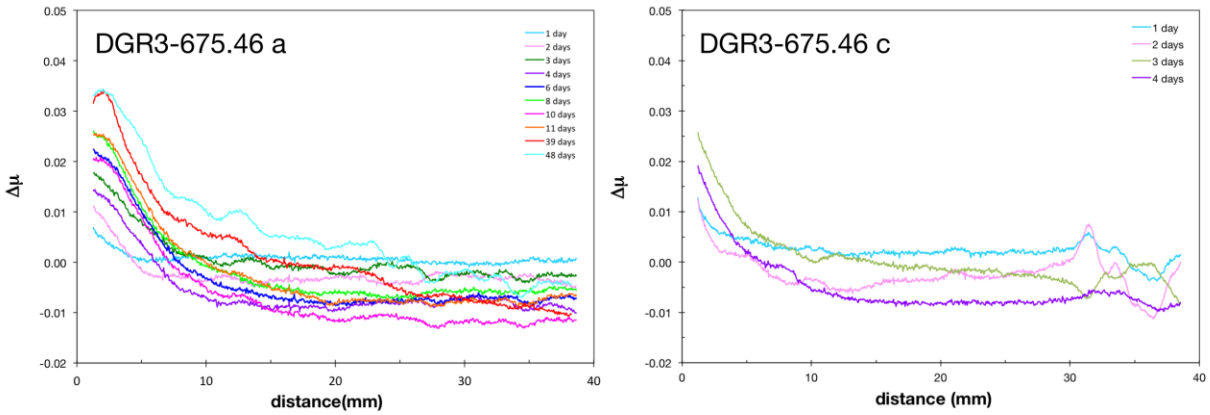

Figure B.1. Examples of Δμ profiles of DGR3-675.46-a and DGR3-675.46-c samples showing alignment artifacts.

B.3. Methodology

In order to estimate the precision of the repeated measurements and to evaluate the efficacy of the standard, a series of tests were performed using: 1) a 40 x 25 x 10 mm aluminum bar, and 2) a 40 mm by 254 mm limestone core. For the first experiment, the aluminum bar was imaged for three times a day (morning, noon and evening) during three days to account for variations in the source due to voltage surges and test the efficacy of the ceramic screen in normalizing the X-ray intensities. The X-ray parameters were set at 50 keV, 60 mA and 15 FPS, and a lead ball was placed on the shielding screen to assist in the registration and to serve as an alternative standard. For the second test, the shielding screen was modified to accommodate two blocks of 30 x 50 x 25 mm, one made of ceramic and one made of aluminum, slanted 10°, to fit with the rest of ceramic bricks (Fig. B.2). To aid in the registration process, a hole was drilled in each block and a led ball was inserted in them.

The sample limestone was aligned in the center and the set was imaged three times in a single day, at 4-hours intervals varying the X-ray tube voltage from 48 to 51 keV.

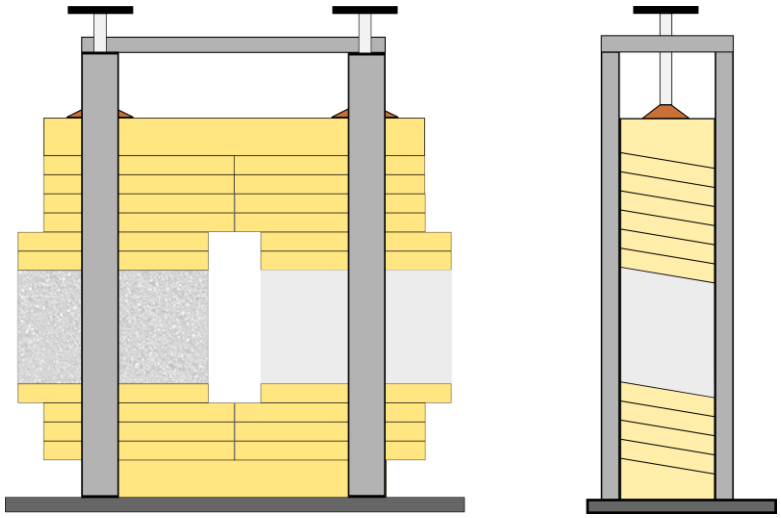

Figure B.2. Shielding screen used in the experiments to protect the detector from oversaturation. Front view (left) shows the ceramic (grey pattern) and aluminum (grey solid) blocks inserted in the frame made of ceramic (Mykroy/Mycalex) bricks (yellow). Lateral view (right) shows the slanted angle of the blocks (modified from Nunn 2018).

Imaging processing was done following the procedure detailed by Cavé et al. (2009) and described briefly in Chapter 1 and 2 using ImageJ (Rueden et al., 2017). For the aluminum bar, an identical region of interest (ROI) was selected for each image and normalized using the aluminum bar and two different regions on the screen: one vertical along two ceramic bricks, and one horizontal along a single brick (Fig. B.3). To determine whether the size of the ROI helps to reduce uncertainty, a 49 % larger ROI was selected on the bar and the greyscale values (gsv) were normalized using the led ball as internal standard. For the second test, an identical region of interest (ROI) in pixel area was cropped on the limestone sample, and on the ceramic and aluminum blocks (Fig. B.3). gsv values were extracted for each radiograph obtained at voltages 48 to 51 keV using ImageJ and raw data of the triplicate measurements were processed on Excel from MicroSoft®.

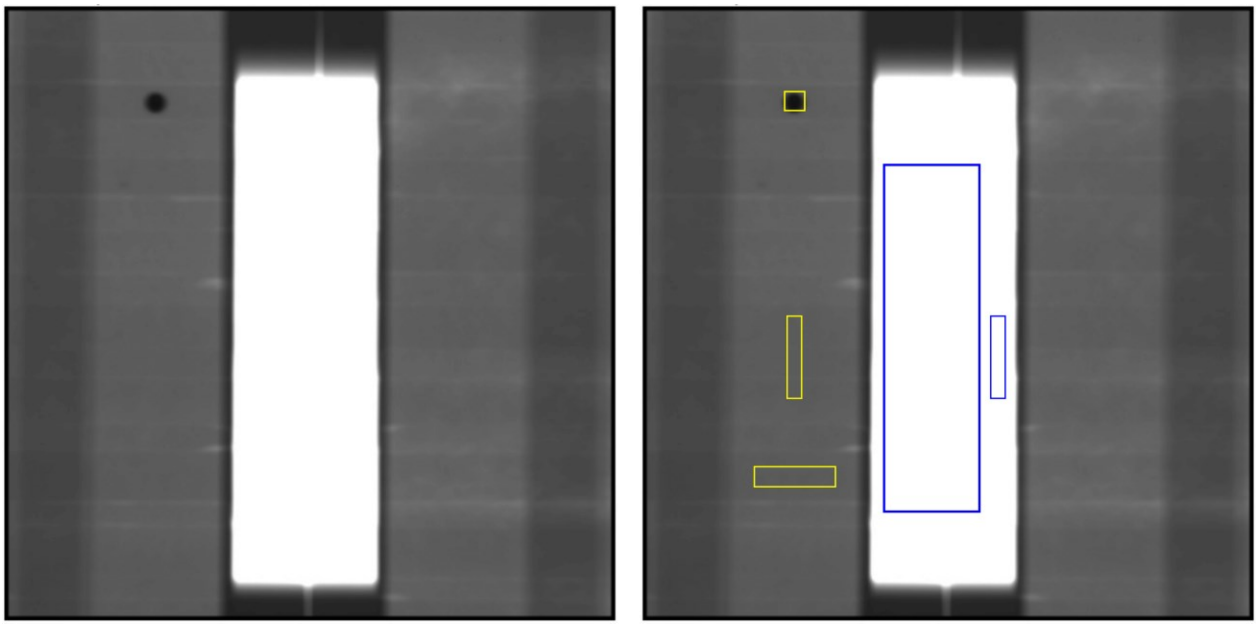

Figure B.3. X-ray radiography image of the aluminum bar showing the position of the lead ball (black circle) used for registration. Three different areas on the screen (yellow rectangles) and one on the aluminum bar (blue rectangle) were used for normalization of the greyscale values measured from the aluminum bar (large blue rectangle).

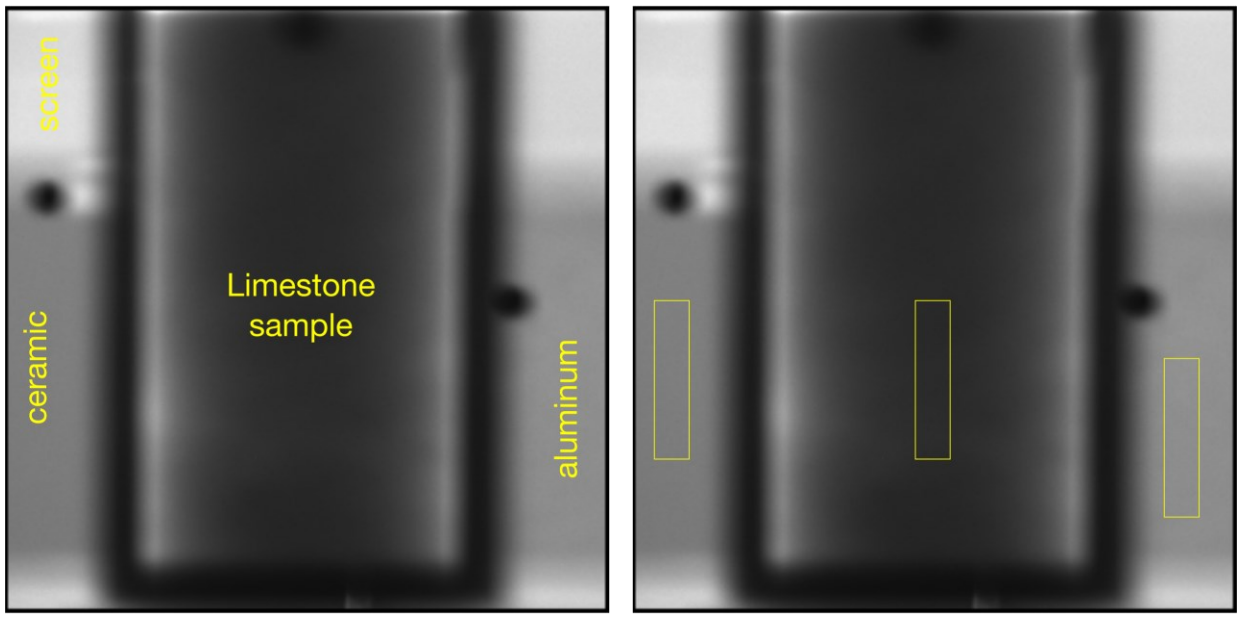

Figure B.4. X-ray radiography image of the limestone sample obtained with the modified screen. Left: location of the region of interests (ROI) on each of the materials tested. Black circles: lead balls inserted inside of the ceramic and aluminium blocks.

Careful steps were taken during the experiments to ensure the possibility of mistakes were minimized (e.g. calibration, sample positioning, registration).

B.4. Results and Discussion

Mean gsv versus distances profiles obtained from the aluminum bar show that the time-series gsv vary consistently over the period of the experiments, and that the values also change with the standard used for normalization (Fig. B.5). The percentage difference between the gsv of the reference image and the time-series increases in average from 0.5% to 1 % when normalization is performed using the vertical area on the shielding screen instead of the horizontal. A possible reason for this change may be explained by a slight attenuation difference between the two ceramic bricks included in the vertical normalization area. The horizontal region runs along a single brick in which attenuation should be more homogeneous. On the other hand, there is an apparent relation between gsv intensities with imaging time, i.e. higher gsv on images collected at on-peak periods (noon) and lower gsv on images obtained at mid-peaks periods (morning and evening), when normalizing with the shielding screen. However, when the normalization is done using the lead ball, this trend is inverted (Fig. B.5 D). Furthermore, the gsv obtained using this standard are in average 0.5-1% lower than when using the shielding screen and show a larger standard deviation (mean 12687.32 $\pm$ 73, 1σ). A larger ROI was selected for this test to determine whether it would help to reduce the uncertainty of repeated measurements but it was not possible to establish a relationship. Because the aluminum bar has a constant thickness, it would be expected that the number of photons reaching the detector would be constant from image to image. It is notable then, that the mean gsv vary significantly from image to image and a correlation with unaccounted voltage fluctuations due to variations in the utility grid cannot be drawn from these tests.

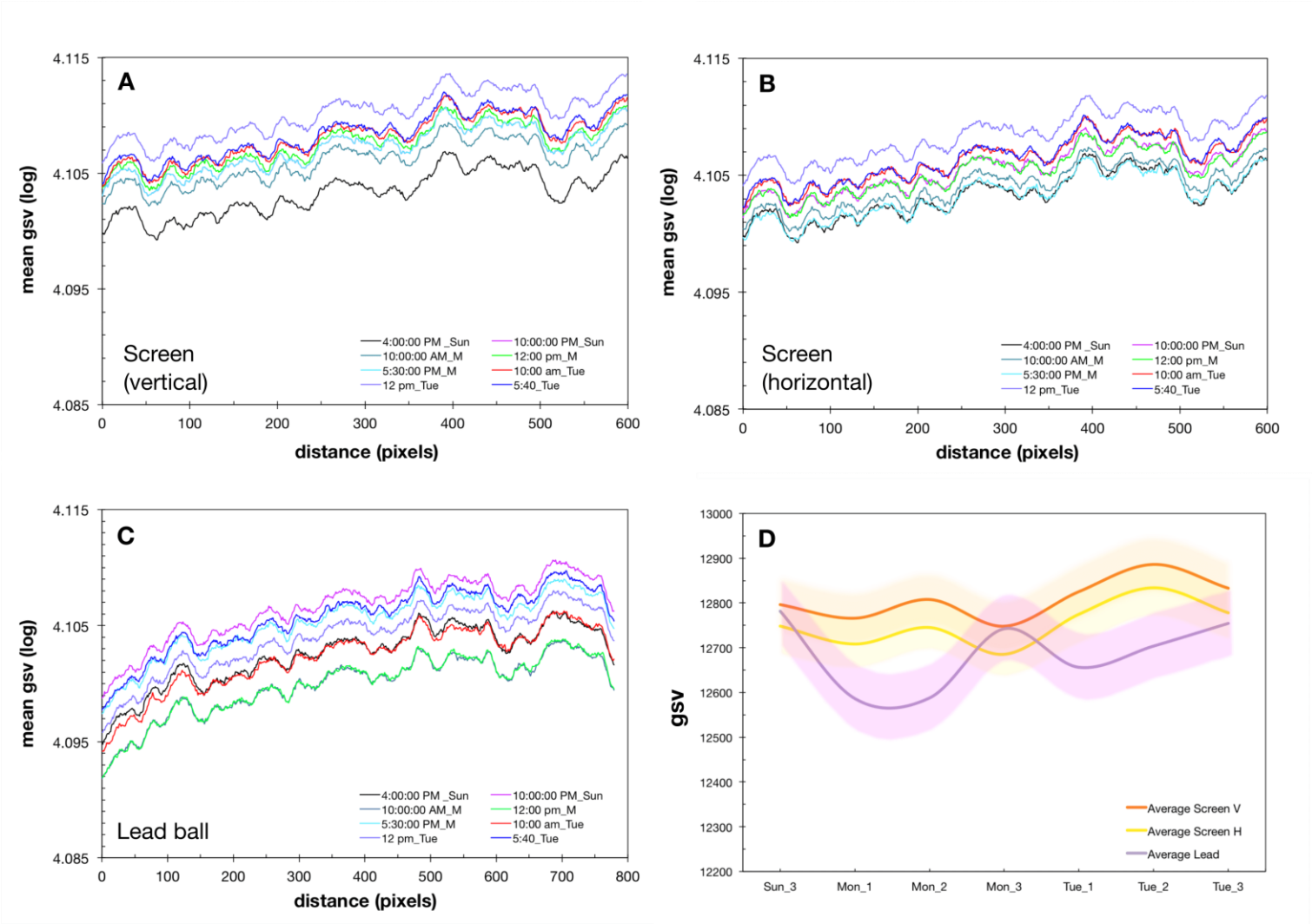

Figure B.5. Greyscale values (gsv) versus distance plots of the aluminum bar imaged at on-, mid- and off-peak periods of electricity consumption. The normalization of the time-series X-ray intensities was done using a vertical (V) and horizontal (H) area on the shielding screen (**A** and **B** respectively), and a lead ball (**C**). **D**: Mean gsv (normalized measurements) of the aluminum bar over time showing one standard deviation (coloured bands). Sun: Sunday; Mon: Monday; Tue: Tuesday. 1: morning; 2: noon; 3: evening.

It is known that repeated measurements of test objects are the best method to determine precision in X-ray quantitative measurements; however, it is recommended to perform the assessment using calibrating materials similar to the tested object (ASTM, 2011). With this approach, a region on the aluminum bar was selected for normalization. The area was of similar size in pixels to the normalization area selected on the shielding screen. The results show a consistent overlap of the time-series gsv with the reference image, and no variation with imaging time (morning, noon or evening) is observed (Fig. B.6). The mean gsv of the aluminum bar is 12681.89 (± 55, 1σ) and the percentage difference between the reference image and time-series is below 0.05%. This result allowed to identify the effect of voltage swinging during image acquisition on the measured gsv (Fig. B.6, B). Additionally, it is apparent that systematic uncertainties also affect the measurements as it is noticed on the crest of the profile. From 0-50 pixels and 400-500 pixels the reference image displays anomalous variations that may be related to noise.

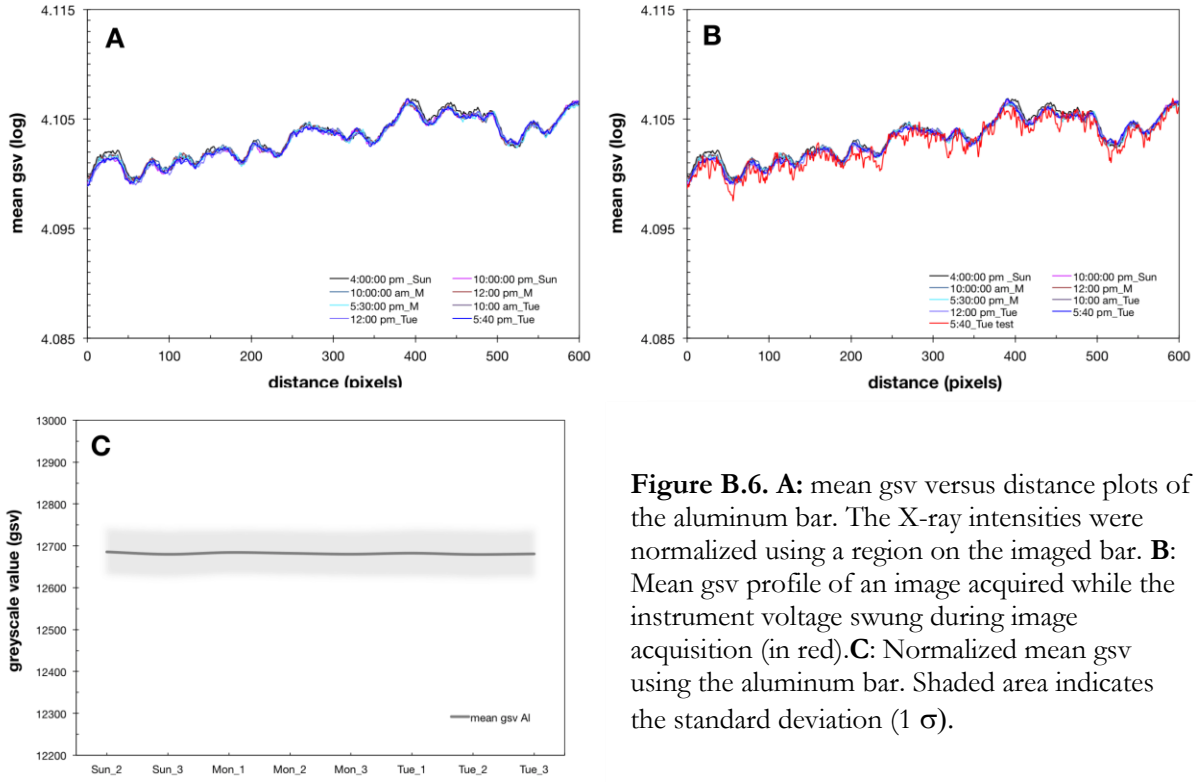

Figure B.6. A: mean gsv versus distance plots of the aluminum bar. The X-ray intensities were normalized using a region on the imaged bar. **B**: Mean gsv profile of an image acquired while the instrument voltage swung during image acquisition (in red).**C**: Normalized mean gsv using the aluminum bar. Shaded area indicates the standard deviation (1 σ).

The results of the second experiment demonstrate that the attenuation of the standard materials tested have a strong positive correlation with voltage variation (Fig. B.7). The aluminum (Al) and ceramic (Cer) blocks show a similar regression line, whereas limestone has an attenuation trend that diverges noticeably from the blocks. The limestone, Al and Cer blocks have similar area mass (Table B.1), but the higher atomic number of the limestone components, through increased photoelectric interactions, attenuates more effectively the incident X-ray photons.

Table B.1. Physical characteristics of the tested materials to be used as standards.

Standard	ρ (g/cm^3)	Thickness (cm)	Area mass (gr/cm^2)
Al block	2.7	2.5	6.75
Cer block	2.6	2.5	6.5
Limestone	2.66	2.54	6.76

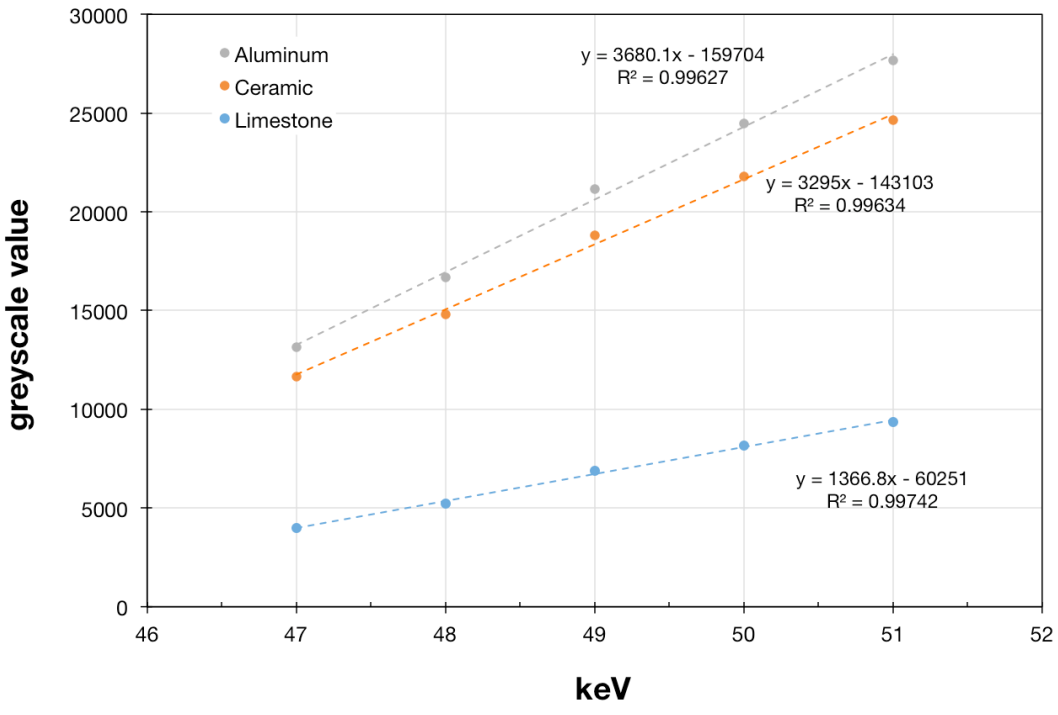

Figure B.7. Variation of gsv with changes in X-ray tube voltage (keV) of the tested materials (limestone core, aluminum and ceramic blocks) considered as potential standards for diffusion experiments with X-ray radiography (dashed lines are the best-fitting line).

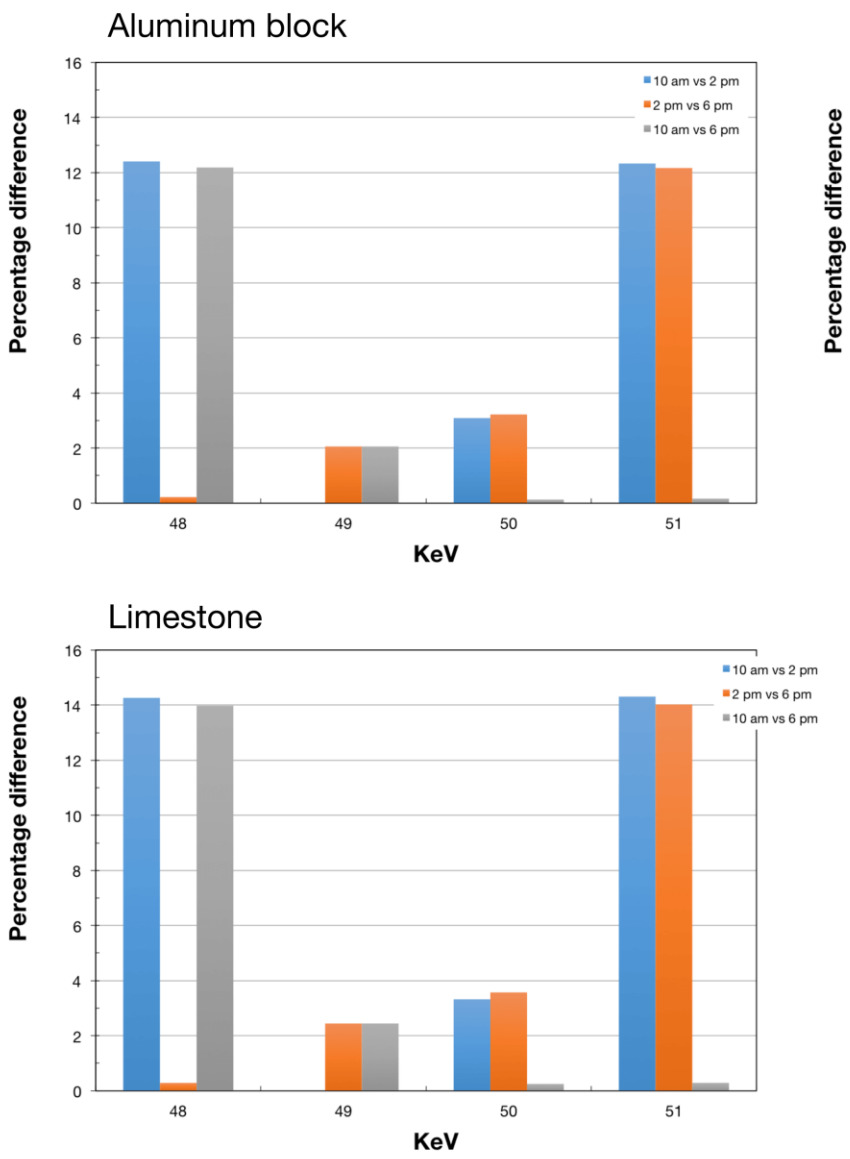

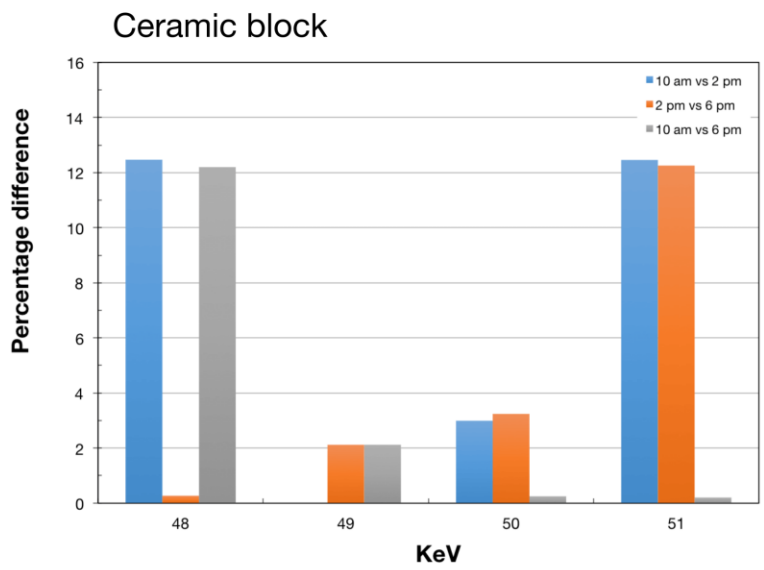

Figure B.8. Percentage variation of the mean gsv with different voltages of the standard materials tested. X-ray images triplicates were obtained at 4-hours intervals.

The intensities of the triplicate ROI, recorded as gsv, of the three tested standard materials were compared with one another. The results show that at 48 and 51 keV, the raw gsv have the largest percent difference (12 % Al and Cer blocks, 14 % limestone), and at 49 keV a better agreement among the triplicate measurements is observed (2% blocks, 2.6% limestone; Fig. B.8). Interestingly, the radiographs taken in the morning (10 am) and afternoon (2 pm) at 49 keV show no variation of the mean gsv (0 % difference). Similarly, when comparing images obtained at 10 am and 6 pm at 50 and 51 keV, the percentage difference of the mean gsv is below 0.2 %. It is unknown the origin of the high agreement among the radiographs at these voltages. As noticed from the experiment with the aluminum bar, voltage fluctuations from the grid are effectively rectified by the instrument, and the image registration procedure was the same for all the images because the experimental set up remained in place during the duration of the test, thus the alignment was not disturbed.

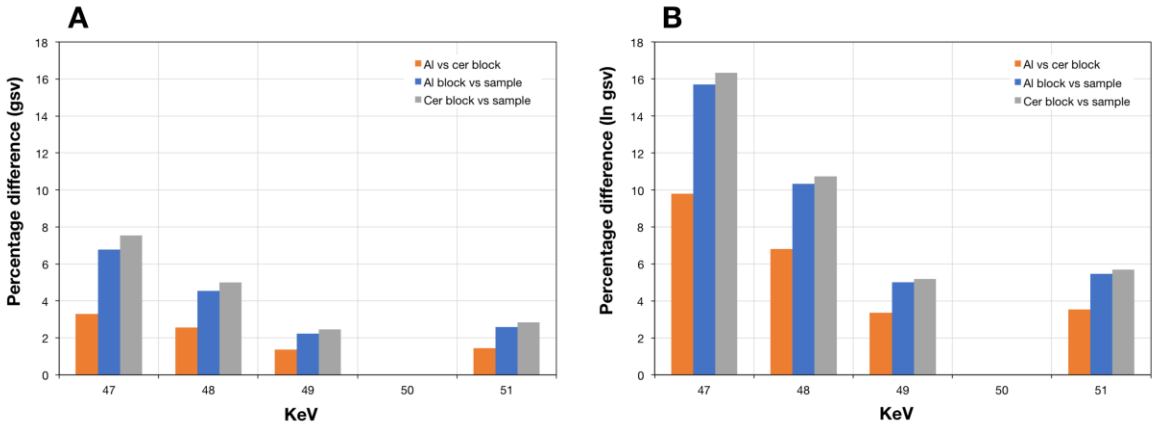

Figure B.9. Percentage difference between the limestone and the Al and Cer blocks as potential standard materials. **A**: mean gsv. **B:** plot showing two-fold increase in the percentage difference when the ln of the mean gsv is calculated.

On the other hand, when comparing how the mean gsv of a given pair of materials (Al vs limestone, limestone vs Cer block, and Al vs Cer blocks) vary relative to 50 keV (parameter selected for the Cobourg Formation experiments), it is noticed that the lowest variation exist between the Al

and Cer block. However, for selecting the best standard for diffusion experiment, limestone coupled with the Al block has that the lower percentage difference. It is significant that the difference in the values increases two fold when the natural logarithm is calculated. This explains the larger discrepancies observed on the $\Delta\mu$ plots.

B.5. Summary and Conclusions

The possible effects of voltage fluctuations on the gsv measurements of an aluminum bar were investigated and three potential standard materials (limestone, aluminum and ceramic) were tested at different voltages. The gsv values of the aluminum bar were normalized using two different regions on the ceramic shielding screen and a led ball. The results show that the data are repeatable when the X-ray intensity variations are normalized with the screen but they are not precise. The use of a lead ball for normalization produces considerable variation in the gsv measurements and when the data are compared with those normalized with the ceramic screen, neither gives a reliable mean gsv of the aluminum bar. The lack of agreement between the two data set may be related to alignment artifacts and the different mass attenuation of the standard materials used. Time-series gsv normalized using a region on the tested aluminum bar shows good agreement with the reference gsv; the plot allows to identify systematic errors that were not visible when normalization was done using the shielding screen and the lead ball.

In the case of the standard materials tested, it is observed that at 49 keV the variation of the mean gsv of triplicates images was lower for three of them, and that the Al block can give better results than the Cer block as normalization standard.

B.6. References

ASTM, 2011. Standard guide for Computed Tomography (CT) Imaging. ASTM International Committee E07, West Conshohocken, PA, USA. https://doi.org/10.1520/E1441-11

Cavé, L., Al, T., Xiang, Y., Vilks, P., 2009. A technique for estimating one-dimensional diffusion coefficients in low-permeability sedimentary rock using X-ray radiography: Comparison with through-diffusion measurements. J. Contam. Hydrol. 103, 1–12. https://doi.org/10.1016/j.jconhyd.2008.08.001

Nunn, J., 2018. Investigations of partial gas saturation on diffusion in low- permeability sedimentary rocks. University of Ottawa, Ottawa, ON.

Rueden, C.T., Schindelin, J., Hiner, M.C., DeZonia, B.E., Walter, A.E., Arena, E.T., Eliceiri, K.W., 2017. ImageJ2: ImageJ for the next generation of scientific image data. BMC Bioinformatics 18, 529. https://doi.org/10.1186/s12859-017-1934-z

Selman, J., 2000. Fundamentals of Imaging Physics and Radiobiology. Charles C. Thomas Publisher, Limited.

Sprawls, P., 2019. Interaction of radiation with matter [WWW Document]. Phys. Princ. Med. Imaging. URL http://www.sprawls.org/ppmi2/INTERACT/#INTRODUCTION (accessed 1.13.20).

Appendix C

PETROGRAPHIC ANALYSIS OF THE COBOURG FORMATION

C.1. Introduction

Petrographic studies were carried out on thin sections obtained from the centre of the DGR3-675.46 and DGR4-671.24 cores (Fig. C.1). The purpose was to gain an understanding of their mineralogy and internal structure, as well as to investigate the geological processes that may have affected the samples initial porosity.

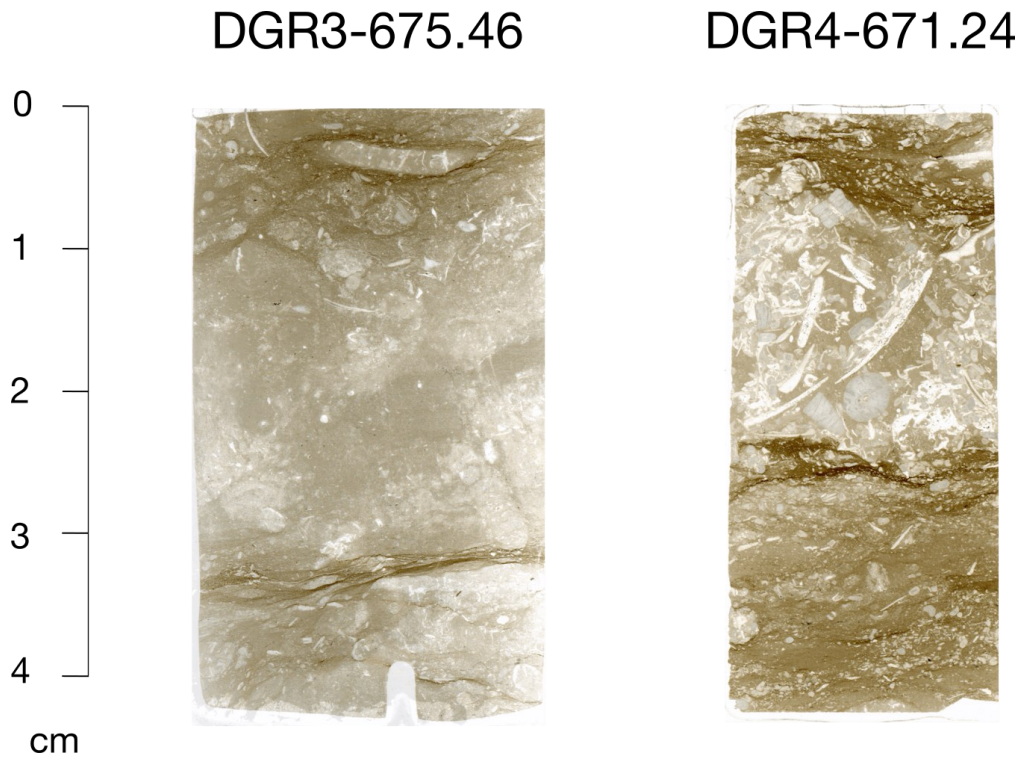

Figure C.1. Thin sections obtained from the centre of the 76-mm DGR3-675.46 and DGR4-671.24 cores. Argillaceous fine laminations are observed on the two of them.

C.2. Background

The argillaceous rocks currently under investigation as potential repository host rocks include a broad group of sedimentary formations deposited in lacustrine and marine environments. It is well known that the unique physicochemical properties of clayey formations are determined by their texture, fabric, mineralogy and diagenetic history (Aplin and Macquaker, 2011). The interplay of these variables, which are influenced by sediment provenance (allochthonous and autochthonous components), deposition environment, geochemistry of the water column and post-depositional changes, have an important effect on the porosity of the rock (Loucks et al., 2012; Potter et al., 2005). The depositional environment of the Cobourg Formation is interpreted to be a well-oxidized shallow marine environment with intervals of anoxic conditions (Obermajer et al., 1999). Gravimetric measurements of these cores show that the bulk porosity is 1-2 %, and like in other argillaceous formations, most of the porosity and pore connectivity occur in the embedding clay groundmass (Houben et al., 2013). The non-clay mineral components, such as carbonates, fossils, pyrite, etc., also affect the pore-size distribution, but it is the clay fraction that controls the transport properties (Desbois et al., 2009; Timur et al., 1971)

C.3. Qualitative petrographic analyses

C.3.1. DGR3-675.46

The DGR3-675.46 thin section shows distinct bioturbation with quasi-vertical burrows (thalassinoides) in the carbonate mud, and argillaceous seams produced by pressure dissolution. Soft-sediment mud clasts containing allochems are located in the horizontal argillaceous laminae (Fig. C.2 A). Bioclasts are abundant, and well-preserved crinoids, broken braquiopods and ostracods are commonly observed; the braquiopod fragments sometimes show an inner prismatic calcite layer (Fig. C.2 C) or foliation. Planktonic allochemes such as globigerina are sparse. Carbonates are the main

minerals in the rock, they are mostly calcite and less common dolomite. Euhedral dolomite is usually found adjacent to two secondary calcite veins and within the argillaceous seams. The two mm-wide, recrystallized-calcite veins run perpendicular to bedding. The fine-grained matrix contains abundant clays, which also occur in bands sometimes iron stained.

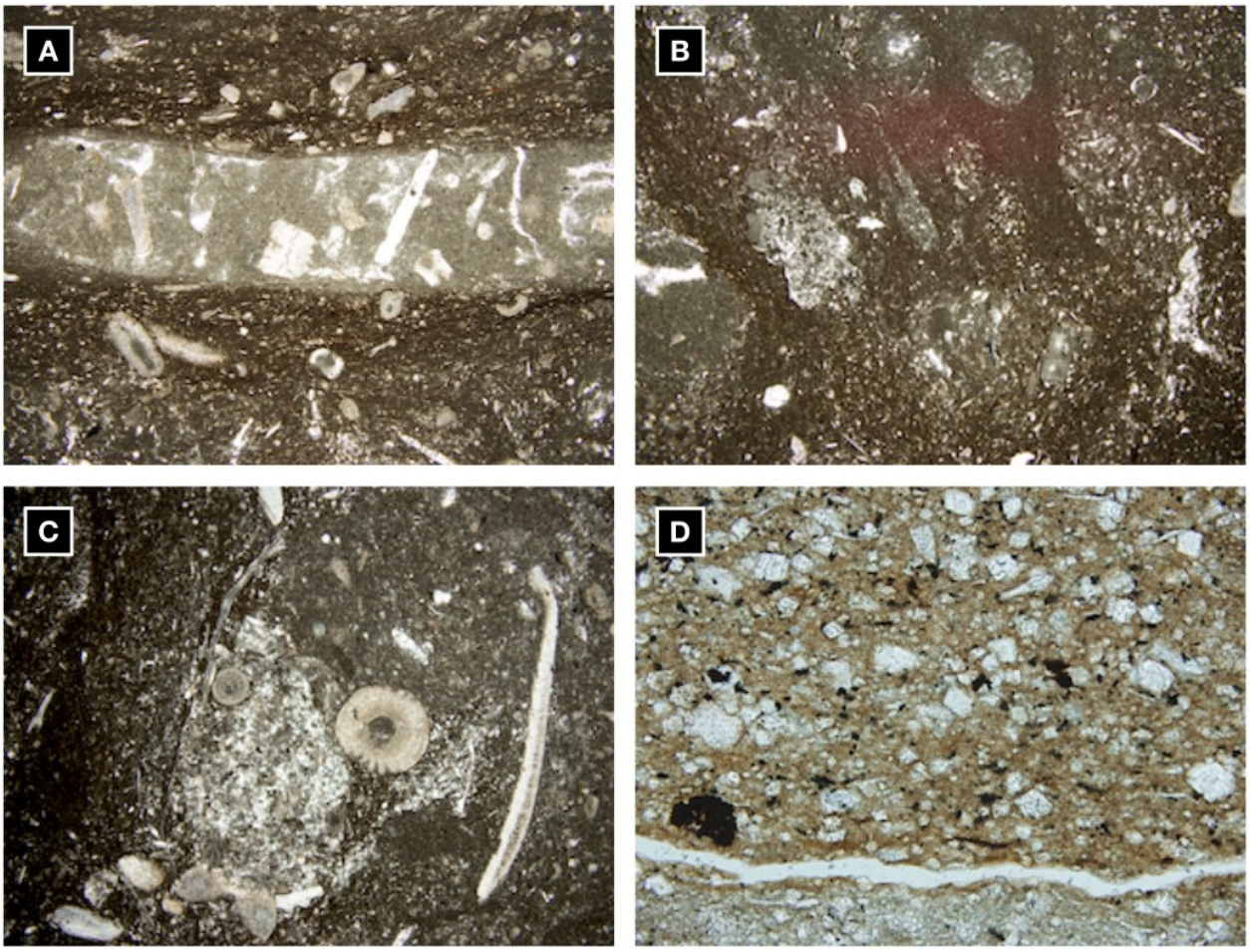

Figure C.2. A) Soft sediment mud clast. **B)** Pellets in carbonate mud and iron-stained clay-rich matrix. **C**) Large brachiopod fragment, crinoids and skeletal clasts in a micritic matrix. **D)** Recrystallized dolomite crystals in a micritic groundmass.

C.3.2. DGR4-671.24

The DGR4-671.24 is composed of a packstone interbeded with a wackstone. In the bioclast packstone, crinoids, bivalves and trilobites are the major allochems, some of them are well preserved (e.g crinoids) and others, like braquiopods, are broken. Also, some bioclast display a well-preserved

thin envelope, probably of micrite, but others have fractured walls particularly when they come in contact with other grains. The stress is observed at most of the bioclasts boundaries, many of which exhibit a saw-tooth appearance (Fig. C.3, A-C). In the wackstone, carbonate mud with dark, wavy argillaceous laminations is visible. Pyrite crystals are usually abundant in these areas.

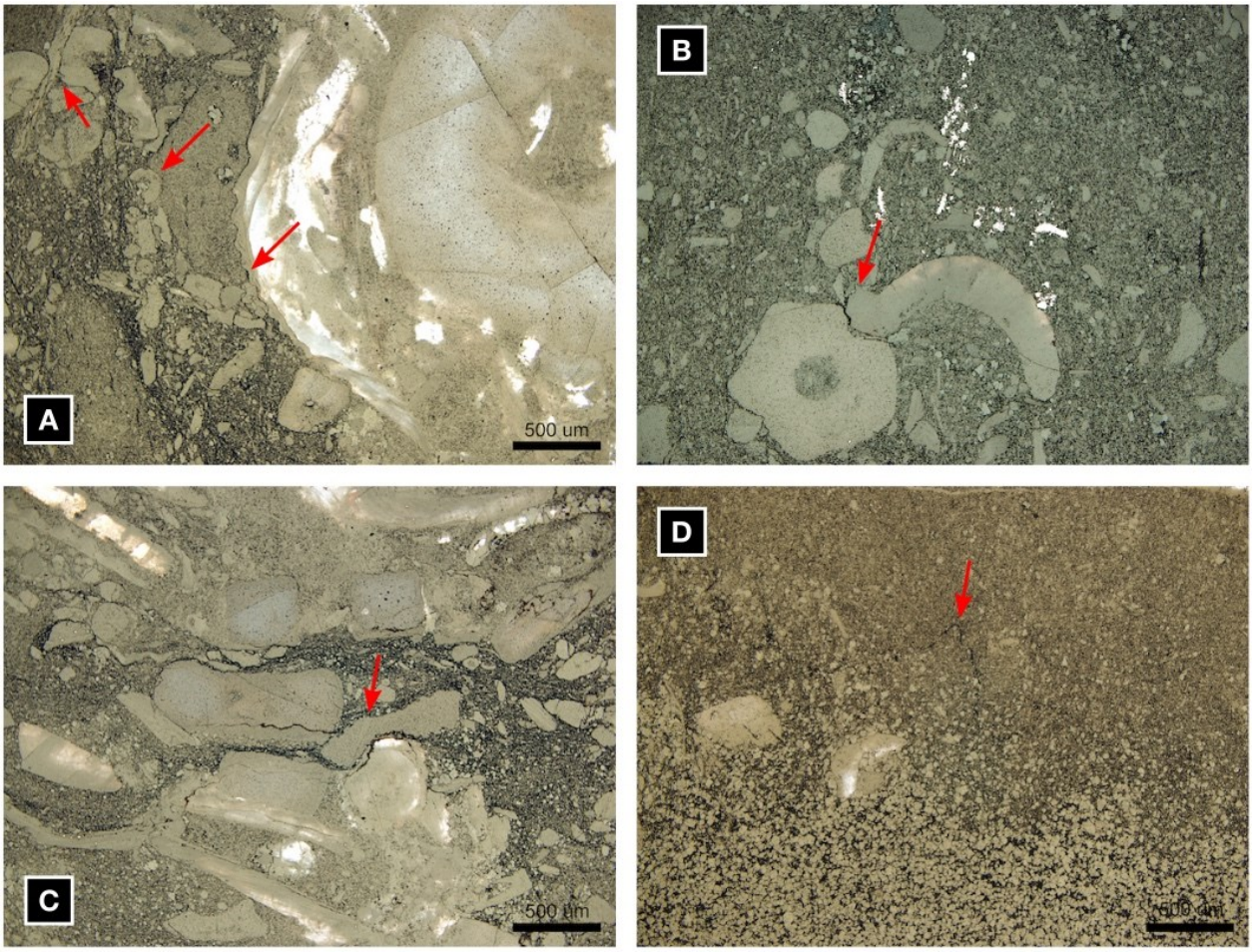

Figure C.3. A) Compacted grains along argillaceous seams. The allochems have crushed edges (arrows). **B)** Star-shaped crinoid showing crushing with another shell fragment (arrow). **C**) Broken edges and crushed grains in direct contact (red arrow) in clay-rich areas. **D)** fine-grained, euhedral recrystallized dolomite within a clay-rich matrix. Red arrows showing a stylolite.

C.4. Summary and Conclusions

Porosity in deep buried argillaceous limestones (> 500 m depth) is significantly reduced due to chemical compaction, a process catalyzed by the clay content in the rock (Brown, 1997; Ehrenberg, 2006; Ehrenberg et al., 2006; Saller et al., 1999). During burial diagenesis, pressure dissolution occurs at intergranular contacts between carbonate and clastic grains; the resulting dissolved solids (mainly calcium carbonate) diffuse more favourably in the clay-rich zones and precipitate as cement in the neighbouring porous regions, obliterating the primary porosity (Choquette and James, 1986; Oldershaw and Scoffin, 2007; Weyl, 1959). Additionally, the clay minerals concentrate along seems forming wavy, dark laminae, commonly fissile (Brown, 1997).

The early porosity loss in the Cobourg Formation is corroborated by Petts et al. (2017) findings on fluid inclusions isotopic analyses carried out on the Cambrian to Devonian carbonate sequence. They report a hydrothermal brine influx forming a second generation of fluid inclusions during Late Devonian-Mississippian that is observed in all the carbonate sequences at the Bruce nuclear site, except in the Cobourg Formation, evidencing the unit was tightly cemented by this time.

C.5. References

Aplin, A.C., Macquaker, J.H.S., 2011. Mudstone diversity: Origin and implications for source, seal, and reservoir properties in petroleum systems. AAPG Bull. 95, 2031–2059. https://doi.org/10.1306/03281110162

Brown, J.A., 1997. Porosity variation in carbonates as a function of depth: Mississippian Madison Group, Williston Basin, in: Kupecz, J., Gluyas, J., Bloch, S. (Eds.), Reservoir Quality Prediction in Sandstones and Carbonates, AAPG Memoir. pp. 29–46.

Choquette, P.W., James, N.P., 1986. Diagenesis in Limestones - 3. The deep burial development. Geosci. Can. 14, 3–35.

Desbois, G., Urai, J.L., Kukla, P.A., 2009. Morphology of the pore space in claystones – evidence from BIB/FIB ion beam sectioning and cryo-SEM observations. EEarth Discuss. 4, 1–19. https://doi.org/10.5194/eed-4-1-2009

Ehrenberg, S.N., 2006. Posority destruction in carbonate platforms. J. Pet. Geol. 29, 41–52. https://doi.org/10.1111/j.1747-5457.2006.00041.x

Ehrenberg, S.N., Eberli, G.P., Keramati, M., Moallemi, S.A., 2006. Porosity-permeability relationships in interlayered limestone-dolostone reservoirs. AAPG Bull. 90, 91–114. https://doi.org/10.1306/08100505087

Houben, M.E., Desbois, G., Urai, J.L., 2013. Pore morphology and distribution in the shaly facies of Opalinus Clay (Mont Terri, Switzerland): Insights from representative 2D BIB–SEM investigations on mm to nm scale. Appl. Clay Sci. 71, 82–97. https://doi.org/10.1016/j.clay.2012.11.006

Loucks, R.G., Reed, R.M., Ruppel, S.C., Hammes, U., 2012. Spectrum of pore types and networks in mudrocks and a descriptive classification for matrix-related mudrock pores. AAPG Bull. 96, 1071–1098. https://doi.org/10.1306/08171111061

Obermajer, M., Fowler, M.G., Snowdon, L.R., 1999. Depositional Environment and Oil Generation in Ordovician Source Rocks from Southwestern Ontario, Canada: Organic Geochemical and Petrological Approach. AAPG Bull. 83. https://doi.org/10.1306/E4FD41D9-1732-11D7-8645000102C1865D

Oldershaw, A.E., Scoffin, T.P., 2007. The source of ferroan and non-ferroan calcite cements in the Halkin and Wenlock Limestones. Geol. J. 5, 309–320. https://doi.org/10.1002/gj.3350050206

Petts, D.C., Saso, J.K., Diamond, L.W., Aschwanden, L., Al, T.A., Jensen, M., 2017. The source and evolution of paleofluids responsible for secondary minerals in low-permeability Ordovician limestones of the Michigan Basin. Appl. Geochem. 86, 121–137.

Potter, P.E., Maynard, J.B., Depetris, P.J. (Eds.), 2005. Provenance of Mudstones, in: Mud and Mudstones: Introduction and Overview. Springer Berlin Heidelberg, Berlin, Heidelberg, pp. 157–174. https://doi.org/10.1007/3-540-27082-5_7

Saller, A.H., Dickson, J.A.D., Matsuda, F., 1999. Evolution and distribution of porosity associated with subaerial exposure in Upper Paleozoic platform limestones, West Texas, Arthur. AAPG Bull. 83, 1835–1854.

Timur, A., Hempkins, W.B., Weinbrandt, R.M., 1971. Scanning electron microscope study of pore systems in rocks. J. Geophys. Res. 76, 4932–4948. https://doi.org/10.1029/JB076i020p04932

Weyl, P.K., 1959. Pressure solution and the force of crystallization: a phenomenological theory. J. Geophys. Res. 64, 2001–2025. https://doi.org/10.1029/JZ064i011p02001

Appendix D

GREYSCALE (GSV) AND Δμ PROFILES OF THE COBOURG FORMATION

D.1. Introduction

DGR3-675.46 and DGR4-671.24 preserved drill cores were used for the present study. Four sub-cylinders were drilled from each core segment (two of 20 mm diameter by 40 mm length and two of 25.4 mm diameter by 40 mm length) with the main axes normal to bedding (shown in Fig. 2.1). The gsv vesus distance profiles and Δμ plots for the 20 mm by 40 mm sub-cores are presented in this section. The radiography measurements for the 25.4 mm by 40 mm sub-cylinders are not included due to their very low SNR.

D.2. Gsv and Δμ profiles

The mean gsv versus distance profiles for samples DGR3-675.46-a and -c, and DGR4-671.24-a and -c prior to tracer diffusion display significant variability along the sample length and among the samples (Fig. D.1, A to D). X-ray attenuation caused by tracer diffusion decreased gsv 3 ± 0.1 % in average for DGR3-675.46-a and -c, with some regions decreasing up to 6% after 152 days of diffusion. In the case of sample DGR4-671.24-a, gsv decreased 3.5 ± 0.9 % in average after 163 days, and for DGR3-675.46-c gsv were reduced in 4 ± 0.5 % in average after 155 days.

The profiles of Δμ versus distance for DGR3-675.46-a and DGR4-671.24-c (Fig. D.2, A and B) become uneven after 48 days for the former and 11 days for the later. The irregular Δμ profiles indicate tracer accumulation in the sample where the distinct humps appear. Visual comparison with the DGR3-675.46-a polished thin section (Fig. D.2, C) shows correlation between tracer accumulation and the dark, clay- and organic rich zones (see Chapter 2 for discussion).

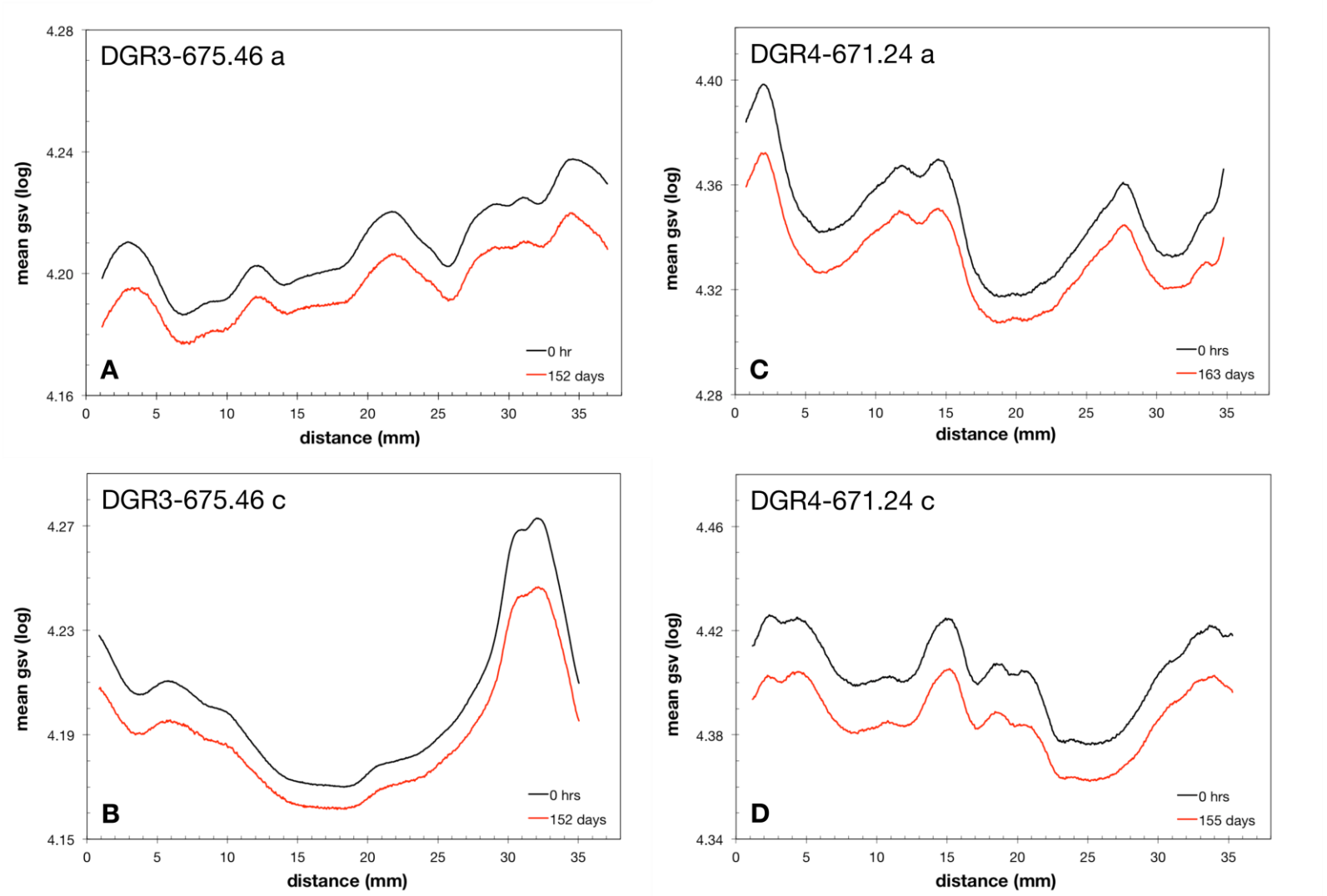

Figure D.1. Mean gsv vesus distance profiles for DGR3-675.46-a (**A**) and -c (**B**), and DGR4-671.24-a (**C**) and -c (**D**) subcores showing X-ray attenuation variability along the sample length. The black line (0 hrs) displays the gsv prior to tracer diffusion and the red line indicates the X-ray attenuation caused by tracer diffusing in the pore space over time (*n* days).

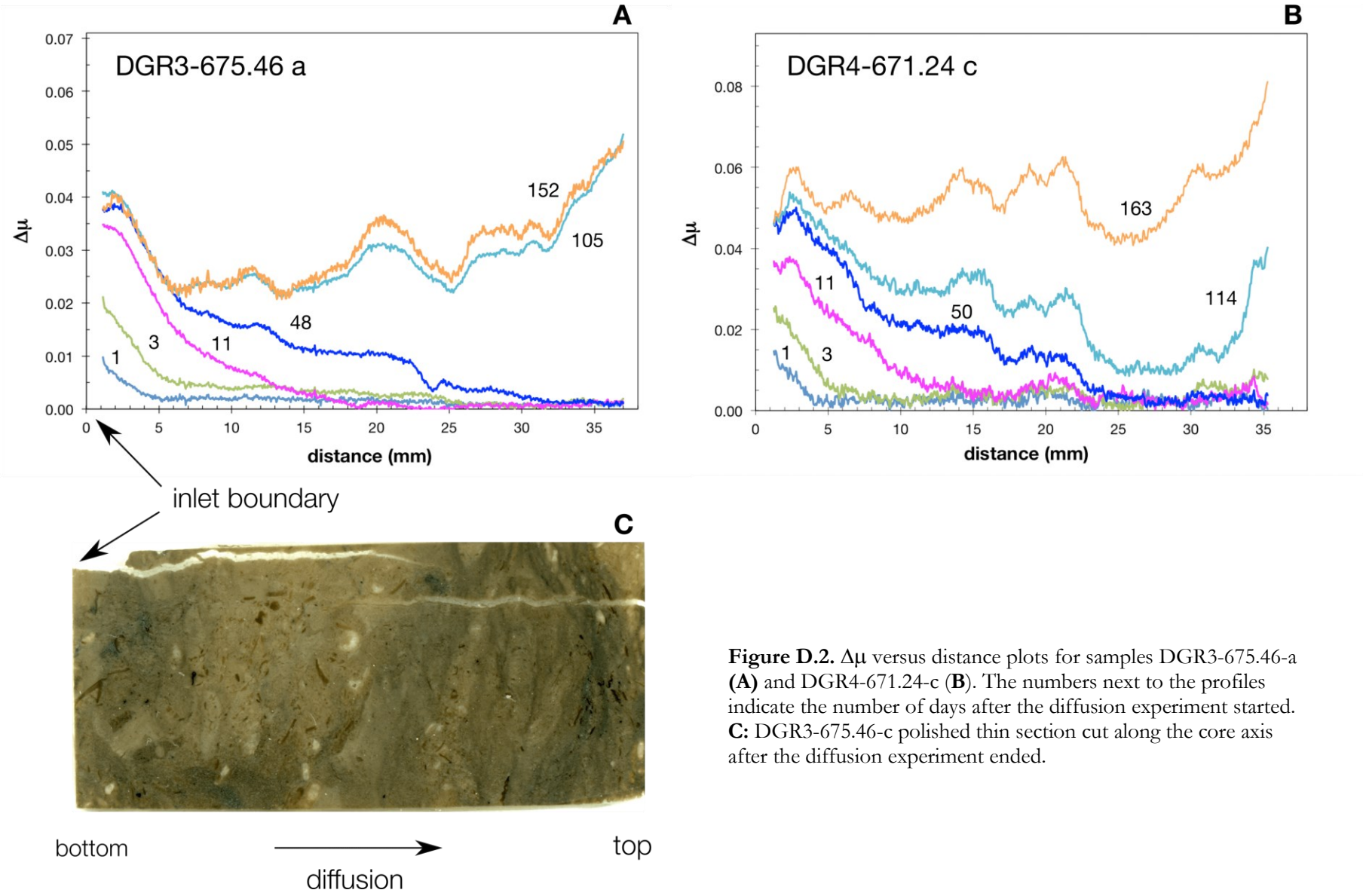

Figure D.2. Δμ versus distance plots for samples DGR3-675.46-a **(A)** and DGR4-671.24-c (**B**). The numbers next to the profiles indicate the number of days after the diffusion experiment started. **C:** DGR3-675.46-c polished thin section cut along the core axis after the diffusion experiment ended.